Theoretical Investigations of Gold Nanostructures

by

Nicola Totò

A thesis submitted to
The University of Birmingham
for the examination of
DOCTOR OF PHILOSOPHY

School of Physics and Astronomy
University of Birmingham
June 2007

UNIVERSITY OF BIRMINGHAM

University of Birmingham Research Archive

e-theses repository

Abstract

The research described in this thesis has focused on the properties of some nanometre scale systems mainly composed of gold. These systems have attracted a considerable amount of attention within the scientific community due to their vast range of applicability and their profound physical interest. Throughout this work, a semiempirical many-body potential has been used to model the atomic interaction in gold.

The first part of the thesis reports a study carried out on gold nanoclusters of between 53 and 80 atoms. The structures of the clusters have been globally optimised by using a genetic algorithm. The potential energy surface generated by the semiempirical potential has thus been sampled by the algorithm in a search for the global minimum. Decahedral structures have been found to predominate in the size range investigated.

The second part of the thesis is concerned with the study of the nanoscale finger pattern induced on a stepped Au(111) surface when scanning with a scanning tunneling microscope. An atomistic model of the system implemented by a Kinetic Monte Carlo algorithm has been set up which proved that the phenomenon is a diffusion kinetic instability triggered by the effect of the scanning tunneling microscope tip.

A thorough study of the kinetics of diffusion on Au(111) has made it possible to improve the model, thus reaching a satisfactory agreement between the experimental and simulated data. It has been found that the diffusion barriers for certain processes, such as step, corner, and kink diffusion, are important in determining the shape of the fingers. In particular it has been observed that the finger width can be finely tuned simply by varying the height of the barrier for diffusion on the bare surface. Finally, the model has been further refined by introducing the effect of the microscope tip on the surface. This is the most realistic atomistic simulation of such a system performed so far.

To Mario Guidone and Antonio Ciarrocchi, for their human touch and love for science

Acknowledgements

I would like to thank my supervisors Prof. Roy L. Johnston, Dr. Quanmin Guo and Prof. Richard E. Palmer, whose guidance and ideas helped me throughout my PhD. Prof. Riccardo Ferrando brought a contribution to this thesis which could hardly be overrated. His expertise and long term experience were crucial for the successful outcome of this work.

I also benefited from illuminating discussions with Dr. Feng Yin in Birmingham, and Dr. Giulia Rossi and Dr. Florin Nita in Genoa. I feel indebted to past and present members of Johnston's group (Gareth, Graham, Ben, Nick, Oliver, Andy), for introducing me into the previously obscure world of computer programming and for making our office such a pleasant work environment.

I express my gratitude to all those people who made my time in Birmingham one of the most important experiences in my life. First of all, I have to thank Xiaodan, for standing right beside me in every moment. Then, I would like to say thanks to my friends, from whom I received and learnt so much. Powei, Miklos, Garry, Tina, Molefe, Ana, Margarita, Yiannis, are some of the people with whom I shared a part of my life in Birmingham and whose presence I will definitely miss.

Finally, I cannot omit to acknowledge my family, for all the support I received from them. In particular, I would like to thank my parents for encouraging and always believing in me. To them I owe much more than this thesis.

Contents

List of Figures

List of Tables

Chapter 1

Introduction

The research described in this thesis has focused on the properties of some nanometre scale systems mainly composed of gold. These systems have attracted a considerable amount of attention within the scientific community due to their vast range of applicability and their profound physical interest. For instance, it has been found that supported gold nanoparticles can be successfully employed in heterogeneous catalysis [24], or used in biomolecule detection [25, 26]. Furthermore, nanometre scale [27, 28] and low-dimensional gold systems such as nanowires [29, 30] have been studied for their interesting properties of quantised electronic transport which make them likely candidates for the construction of low current, low energy electronic devices.

Throughout this work, a semiempirical many-body potential has been used. Semiempirical or classical potentials are simple mathematical expressions which aim at modelling interatomic forces arising from quantum mechanical interactions of electrons and nuclei [31]. These analytic potential energy functions result from approximations of higher levels of theory and their development was prompted by the need for a model which is less computer intensive than full *ab-initio* quantum mechanical treatments. Although more precise than semiempirical methods, quantum mechanical calculations can as yet be performed only on systems of limited size, due to the high amount of computer resources required.

The first part of the thesis reports a study carried out on gold nanoclusters of be-

tween 53 and 80 atoms. The structures of the clusters have been globally optimised by using a genetic algorithm. The potential energy surface generated by the semiempirical potential has thus been sampled by the algorithm in a search for the global minimum. Chapter 2 is a general introduction to cluster physics, with particular regard to structural optimisation. The main tools of cluster global optimisation, such as the potential and the search algorithm, are discussed here. In chapter 3 the results of the global optimisation of gold nanoclusters are presented and discussed, after a review of some previous relevant results.

The second part of the thesis is concerned with the study of a different gold nanostructure: the nanoscale finger pattern induced on a stepped Au(111) surface. This phenomenon was observed experimentally during a scanning tunneling microscopy experiment described in chapter 4. The chapter also contains a review of finger patterns in nature and a description of the Au(111).

The phenomenon of nanofinger growth on gold is studied theoretically in chapters 6 and 7. The system is at first modelled as a simple lattice gas in order to show how the phenomenon can be explained in terms of a diffusion instability of the step edge. This first approximate model is presented in chapter 6, along with the results obtained from the calculations performed on Au(111) and Ag(111) by means of a Kinetic Monte Carlo algorithm implementing the model.

The imperfect correspondence of the calculated with the experimental data has prompted the need for an accurate study of diffusion kinetics on Au(111) in the presence of surface defects such as steps, kinks and corners. A thorough calculation of activation energies for all possible diffusion events has therefore been undertaken. Chapter 5 is concerned with adatom thermally activated diffusion on metal surfaces. In the first part of the chapter some general concepts are reviewed and some relevant results on diffusion of a single particle and on the formation of surface nanostructures due to diffusion are presented. The second part of the chapter contains the results of the

activation energy calculations carried out in this work.

The activation energies obtained from the calculations have been used as input parameters for an improved version of Kinetic Monte Carlo algorithm. In the first part of chapter 7 this algorithm is presented and the results obtained from the simulations are illustrated and discussed. The second part of chapter 7 deals with the calculations introducing the effect of the scanning tunneling microscope tip on the surface. A new model has been set up and the results of preliminary tests are reported.

Finally, in Chap. 8 some general conclusions are drawn and some directions for future work are indicated.

Chapter 2

General Methods of Cluster Investigation

2.1 Introduction

The present trend towards decreasing the characteristic length of electronic devices has resulted in a strong interest in the study of microscopic scale systems. A major role in current science and technology is played by so called *nanoscale* systems, i.e. systems typically having dimensions ranging from the order of a few up to a few hundred nanometres.

The term *cluster* usually means an aggregate of a countable number of particles (atoms, molecules or ions) in the range from two to several millions. Clusters of atoms are included in the class of nanoscale systems. In fact, the typical dimensions of a cluster composed of a number of atoms in the range between ~ 10 and ~ 100 turn out to be equal to $\sim 1 - 2$ nm. Indeed, the interest in investigating cluster properties has increased enormously in the past two decades. Clusters form a bridge between atomic and molecular physics on one side and condensed matter physics on the other. From this point of view, the most fascinating aspect in the study of clusters is the investigation of how their properties evolve as the number of building blocks increases. The natural question to ask is what is the size beyond which the cluster behaviour is indistinguishable from the corresponding bulk element. This is of interest also from the technological point of view, since being able to control and manipulate clusters on

the atomic scale would lead to the creation of a whole family of new structures and materials whose features could be tailored at will. Furthermore, due to their small dimensions, clusters display a high ratio of surface to bulk atoms, which makes them natural candidates for heterogeneous catalysis as well as an interesting object of study for surface science.

Technological development, though, needs a deep understanding of the system under study. In the case of clusters this is a particular sensitive issue since many properties (e.g. cluster geometries, binding energies, etc.) cannot be easily accessed by experimental techniques. Hence the importance of theoretical models and computational methods in the field of cluster physics and chemistry.

In this chapter, the main points of cluster theory will be reviewed. The chapter opens with Sect. 2.2, which presents the most popular approaches for describing the interactions between atoms in solids. In particular the family of atomistic potentials called semiempirical potentials will be introduced: an essential element for modelling static and dynamical properties of metals and semiconducting elements. Sect. 2.3 deals with one of the crucial problems in cluster theory, i.e. the search of the global minimum in the energy landscape generated by an atomistic potential. The main optimisation techniques will be presented and explained, with a particular focus on genetic algorithm search, the technique used for this work. The last part of the chapter will provide an overview of nanocluster physics. In Sect. 2.4 the most common structural motifs found to be the global minima of small clusters will be introduced and the connection between the geometric structure and the binding energy of a cluster clarified. In Sect. 2.5 the regularities observed in experimental studies on clusters will be discussed through the introduction of the important concepts of geometric and electronic shells and magic numbers.

2.2   Semiempirical potentials and Gupta potential

The family of potentials known as semiempirical or phenomenological potentials have been used for a long time in Molecular Dynamics and Monte Carlo simulations. Basically, the physics of the model system is at least partially contained in the form of the potential chosen in order to reproduce the system inter-atomic interactions. Thus, the more realistic the choice of the potential, the higher the accuracy which can be achieved in the results of the simulation.

Historically, the first types of potentials to be applied were simple pairwise potentials, where only interactions between pairs of particles are considered. A pairwise potential assumes the following common form:

$$V = \sum_{i=1}^{N-1} \sum_{j>i}^{N} V_{ij}(r_{ij}); \tag{2.1}$$

where N is the number of particles constituting the system and V_{ij} is the form of the potential depending only on the interparticle separation r_{ij}. Typical examples of pairwise potentials are the Lennard-Jones [32] and Morse potentials [33]. Though successfully employed to model ionic or Van der Waals crystals, pairwise potentials turn out to be inadequate in the case of metals, for which the strong delocalisation of bonding electrons over a large number of lattice sites requires the use of a long-range type of many-body potential to faithfully describe their properties. Pairwise potentials were shown to fail also in other aspects such as for example the prediction of the inward relaxation of the topmost surface layer of atoms of a metal surface. Gupta showed that according to predictions based on the use of a pairwise potential a surface can only be expected to expand with respect to the bulk inter-layer spacing [34]. Further drawbacks with pairwise potentials are the missing prediction of the Cauchy violation for cubic solids where the elastic constants C_{12} and C_{44} are different, and the overestimation of the vacancy energy (the energy needed to remove an atom from the bulk and place it on the surface) which is calculated to be equal to the cohesive energy (the energy of

an atom in the bulk) for a pair potential.

These deficiencies prompted the development of a new class of many-body potentials which are expected to better mimic the typical features of metals. Though being obtained from different approximations, all of these potentials can be expressed in the following common form:

$$E_{tot} = \sum_{i=1}^{N} E_i \tag{2.2}$$

$$E_i = \frac{1}{2} \sum_{j \neq i} \varphi(r_{ij}) + F(\bar{\rho}_i) \tag{2.3}$$

$$\bar{\rho}_i = \sum_{j \neq i} \rho(r_{ij}). \tag{2.4}$$

The function $\varphi(r_{ij})$ appearing in (2.3) is a repulsive pairwise potential between atoms i and j at distance r_{ij} from each other. On the other hand, the term denoted as $F(\bar{\rho}_1)$ in (2.3) represents the many-body cohesive contribution to the total energy. It is shown to depend on $\bar{\rho}_i$, which can be envisaged as the electronic density created by the neighbouring atoms at the position of atom i. Within this picture, the energy of the atom i turns out to be identical to the energy of an atom embedded in a uniform electron gas of the same density as the site where i is located. The embedding function F is the key to understanding the nature of the metallic bond and thus to explain the characteristic properties of metals. All many-body potentials of this form were derived after approximations of electronic structure theories in solids such as Density Functional Theory (DFT) or Tight Binding model (TB), and they all display a set of parameters which have to be fitted to experimental or calculated values, hence their name of semiempirical potentials.

The Embedded Atom Method (EAM) [35,36] potential is of the form (2.2)-(2.4) and was the first alternative to traditional pairwise potentials. It is still a popular choice for modelling physical properties of metals. Another potential of the same form which was developed specifically for modelling fcc metals is the Sutton-Chen (SC) potential [37], which is a variant of the Finnis-Sinclair (FS) potential [38]. The Effective Medium

Theory (EMT) [39] potential also belongs to the same family of potentials and has been extensively used in computer simulations in an attempt to retain the essential physics of atom interactions in metals while reducing the computational effort.

The semiempirical many-body potential chosen for this work is known as the Gupta or RGL potential. Based on the second moment approximation to the tight binding scheme [40], the Gupta potential is particularly suitable to describe transition metals, where the d electrons play a decisive role in the bonding. The total energy E of the crystal is expressed by the sum of a pairwise repulsive potential E_r, and an attractive many-body term E_b. Each of the two terms can be seen to be a sum of contributions due to every atom in the system. So the total energy turns out to be:

$$E = \sum_{i=1}^{N} \left(E_r^i + E_b^i \right) ; \tag{2.5}$$

where E_r^i and E_b^i are the contribution due to atom i to the repulsive and attractive part of the potential, respectively. The repulsive and the attractive energy per atom in (2.5) has the following forms:

$$E_r^i = \sum_{j=1, j \neq i}^{N} A \exp \left(-p \left[\frac{r_{ij}}{r_0} - 1 \right] \right) \tag{2.6}$$

$$E_b^i = - \left\{ \sum_{j=1, j \neq i}^{N} \zeta^2 \exp \left[-2q \left(\frac{r_{ij}}{r_0} - 1 \right) \right] \right\}^{\frac{1}{2}} . \tag{2.7}$$

Here r_{ij} is the distance between atoms i and j, whereas r_0 is the interatomic distance when the crystal is at the equilibrium. The quantities A, ζ, p, and q, on the other hand, are parameters that have to be fitted to bulk properties of the metal such as compressibility, lattice constant etc. A determines the magnitude of the repulsive part of the potential, p is the parameter determining the spatial range of the repulsive interaction, ζ is the hopping integral, and q describes the distance dependence of the hopping integral. It can be shown [41] that when only interactions between first neighbours are

considered, the following relations apply:

$$\zeta = \frac{pE}{(p-q)\sqrt{N_{nn}}} \tag{2.8}$$

$$A = \frac{qE}{(p-q)N_{nn}} , \tag{2.9}$$

where N_{nn} is the coordination number. This makes the second moment approximation to the tight-binding a two-parameter model.

Cleri and Rosato [42] have calculated Gupta potential parameters for a wide variety of face centred cubic (fcc) and hexagonal close packed (hcp) transition metals (see Table 3.1 for Gupta parameters for Au). The most important quantities to determine are the two empirical constants p and q, which determine the range of the atomic interactions.

2.3   Global optimisation of clusters

Among the most discussed problems in cluster theory is the search for the lowest energy configuration of a cluster of a given size and composition. The structure of its lowest energy isomers in fact strongly affects the chemical and physical properties of a cluster. This necessitates the investigation of the potential energy surface [43]. Since a cluster possesses no translational symmetry, the number of degrees of freedom scales linearly with its size and the numbers of minima on the potential energy surface scales exponentially. To give an idea of the characteristic orders of magnitude involved in the problem, it has been estimated that for a 55 atom cluster bound by Lennard-Jones type forces, the number of minima in the potential energy surface is of the order of 10^{21} [3]. So, the search for the global minimum of the potential energy of clusters is definitely not a trivial task.

2.3.1   Global optimisation techniques

A brief review of the most commonly employed methods to achieve the global optimisation of the potential energy surface must include techniques such as: simulated

annealing, the Monte Carlo basin hopping algorithm and genetic algorithms.

The simulated annealing technique consists of the slow quenching of the system from a high temperature, corresponding to the liquid phase, to a low energy configuration. In the course of the process, the accessible region of the phase space is probed [44]. When the temperature is high the region of phase space occupied by the system is larger and energy barriers can easily be crossed. When the temperature drops, the lower energy states get more and more favoured according to the Boltzmann distribution and eventually, at absolute zero, only the lowest energy state can be occupied. The evolution of the system between successive steps in the quenching is governed either by Monte Carlo or Molecular Dynamics simulation. Molecular Dynamics simulated annealing has been used, for example, by N. T. Wilson and R. L. Johnston for the study of gold clusters consisting of between 2 and 40 atoms [45].

The basin hopping algorithm was first developed by Doye and Wales [46]. It basically consists of the transformation of the potential energy surface into a steplike surface. In order to accomplish the mapping, a local minimisation is performed in the region surrounding each point in configuration space, the point is then associated with the minimum energy obtained from the local minimisation. This allows one to eliminate the energy barriers separating two successive local minima though preserving the global minimum of the actual potential energy surface.

Genetic algorithms are one of the techniques borrowed by chemistry from artificial intelligence [47] and they have found applications in the study of chemical systems since the early 90's. Because of the importance of this algorithm for the present work, the following section will be concerned with its detailed explanation.

2.3.2 Genetic algorithms

A Genetic Algorithm (GA) is an optimisation strategy inspired by the Darwinian evolution process. It can be applied to any problem where the variables (*genes*) to be optimised can be arranged in a string (*chromosome*). A particular string represents a
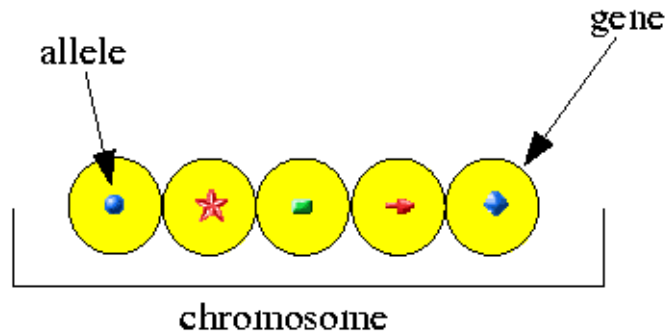
Figure 2.1:   Schematic representation of an individual in a generic genetic algorithm run. (Adapted from Ref. [1]).

trial solution of the problem and, by analogy with biology, the value assumed by each variable is called an *allele* (cfr. fig. 2.1). By means of operators similar to evolutionary processes such as mating (or *crossover*), mutation and natural selection, the algorithm tries to optimise an initial set of solutions that are usually randomly generated. Every step of the algorithm can be seen as giving rise to a new *generation* of *individuals* where the *population* has evolved from the parent population. The algorithms ends either after a fixed number of iterations have been carried out, or when some convergence criterion is satisfied.

Let us now go through the different stages of the cluster GA while introducing at the same time some necessary terminology. As has already been said, the GA is given at the beginning an *initial population* which is usually generated at random. The *fitness* of the population is then assessed: this is an evaluation of the function to be optimised for each member of the population. High values of fitness indicate good solutions for the problem in question. The fitness is an important parameter in that it determines the likelihood for an individual to survive into the next generation and to be selected in the crossover process as one of the parents. The following stage is just the *selection* of the individuals which are due to take part in the mating. One of the possibilities is
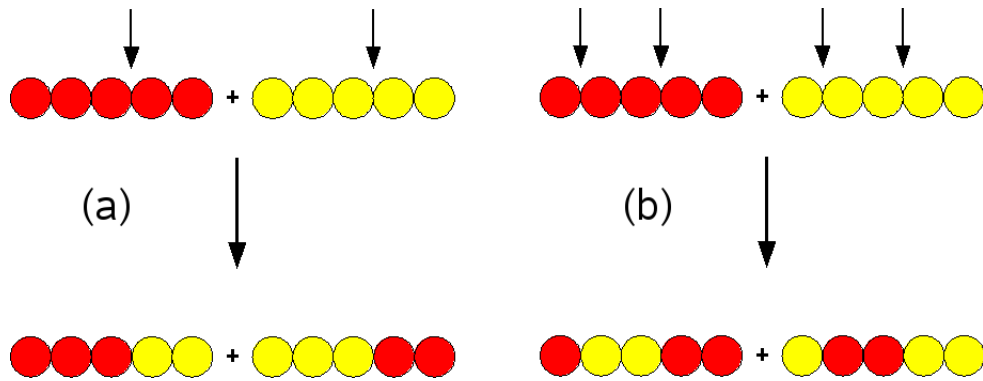
Figure 2.2: Schematic representation of the two crossover mechanisms: (a) one-point crossover, (b) two-point crossover. (Adapted from Ref. [1]).

the *roulette wheel selection* method, according to which an individual is accepted as a parent in the crossover only if its fitness is higher than a randomly generated number, otherwise another element of the population is selected and tested.

Crossover is the actual process by which two parent individuals are combined together and information is transmitted from the parents to their *offspring*. The two most common crossover operations, schematically depicted in fig. 2.2, are *one-point* and *two-point crossover*. In one-point crossover, parents are cut into two parts at the same point and offspring are generated combining complementary genes resulting from the cut. In two-point crossover, on the other hand, parents are cut in the same two points and each parent thus gives rise to three fragments which can be recombined to generate new individuals.

After the offspring have been created, the population is allowed to undergo a certain number of *mutation* processes by which some individuals chosen at random may be either changed in some part or be completely replaced by randomly generated new ones. This guarantees that new genetic material is continously fed into the population and prevents it from the possibility of lack of diversity and stagnation.

The GA continues with a process which is the analogue of *natural selection*. During this stage, the individuals which are to survive into the next generation are selected on

the basis of their fitness. This can be accomplished in several ways. For example the selection process can accept all the offspring without discrimination. Furthermore it can either reject all the parents or select only the fittest ones to let them survive. The latter method is known as an *elitist* strategy and it generally makes the population fitter and fitter, preserving the best elements and getting rid of the worst ones. At the end of the selection process one ends up with a new population and a new GA cycle can be carried out.

2.3.3   Birmingham cluster genetic algorithm

The Birmingham cluster genetic algorithm (BCGA) program [1] is a code developed by Roy Johnston's group specifically to locate global minima of metal clusters up to a few hundreds of atoms. The algorithm used for the structural optimisation of small clusters carried out in this thesis will be described in the following.

    The initial population of clusters of a given size is generated at random, the number of individuals being typically chosen in the range from 10 to 30. Following the approach of Ref. [48], the cartesian coordinates of the cluster atoms are seen as the genes, whereas each cluster plays the role of a chromosome. To ensure that the total volume of the cluster correctly scales linearly with the total number of atoms N, the initial coordinates of the particles constituting the clusters are randomly chosen in the range $[0, N^{1/3}]$. After the initial population has been generated, each component is allowed to relax into its nearest local minimum. This is accomplished using the quasi-Newton L-BFGS minimisation routine [49], which uses analytical first derivatives of the potential.

    Then the fitness of each member of the population is worked out on the basis of the cluster energy V_{clus}. Let V_{min} be the energy of the most stable structure and V_{max} the energy of the least stable structure within the population. Given the energy V_i of a general cluster then, we can define the quantity:

$$\rho_i = \frac{V_i - V_{min}}{V_{max} - V_{min}}, \tag{2.10}$$

which can be used as an argument for the function chosen to evaluate the population fitness. Once specified that we want the lowest energy clusters to have fitness equal to 1 and the highest energy clusters to have fitness close to 0, almost any monotonically decreasing function of ρ can be used provided that its value for $\rho = 0$ is 1 and that for $\rho = 1$ the function vanishes (or it is close to vanish). In our simulations for example a hyperbolic tangent function has been chosen. The fitness f_i of the i cluster is thus calculated as:

$$f_i = \frac{1}{2}[1 - \tanh(2\rho_i - 1)]. \tag{2.11}$$

After the parents have been selected by means of the roulette wheel selection method, the crossover process begins. The choice of mating procedure is central in planning an efficient genetic algorithm, since mating determines the way how the properties of parent clusters are imparted to the offspring. The cluster GA uses a variant of the operator first introduced by Deaven and Ho [50]. Basically, both parent clusters are cut horizontally about one position in one-point crossover and about two positions in two-point crossover. Complementary fragments are then spliced together. The crossover continues until the predetermined number of offspring has been generated. This number is typically chosen as 80% of the population size. Each newly generated cluster is then relaxed into the nearest local minimum of the potential energy with the same routine as that used for the initial population.

Each member of the population thus created has a certain probability of undergoing a mutation process. Mutation operators change the structure of the cluster in several ways. Below are listed some of the most popular mutation schemes:

Atom displacement The coordinates of a certain number of atoms in the cluster are replaced by new randomly generated values.

Twisting The upper half of the cluster is rotated about the z axis by a random angle.

Cluster replacement The cluster is completely removed and replaced by a new one

generated at random. The generation mechanism of the replacing cluster is exactly the same as that followed for the generation of the initial population.

Subsequently, the individuals allowed to survive to the next generation must be selected from the set consisting of the parent clusters, the offspring and the mutated clusters. The fittest individuals among all of the above ones are selected to form the new generation. The cluster GA thus uses an elitist strategy, since it allows members of the old generation to take part in the next one and at the same time it prevents the best members of the population from getting worse in passing from one GA cycle to the next.

At this point one ends up with a new population whose fitness can be assessed and which can undergo the typical operations of a genetic algorithm cycle (crossover, mutation and selection). The whole process can terminate either after a specified number of generations or when a convergence criterion has been achieved. The population is deemed to have converged if the range of cluster energies in the population has not changed after a predetermined number of generations.

2.4   Structural motifs of small clusters

All our simulations have been carried out at absolute zero temperature, this implies that the most stable configuration for a cluster is that which minimises the total energy. In other words, thermodynamical and entropic effects arising at higher temperatures are completely neglected in our scheme. For a comprehensive review of how the temperature can affect the properties of clusters please see Ref. [2].

In this section, rather than giving a thorough overview of the physics of clusters, the structural motifs associated with particularly stable configurations for small clusters will be introduced and discussed. We define a *small cluster* as an aggregate of particles composed of less than one hundred building blocks [51].

To a reasonable degree of approximation, the potential energy V of a cluster com-

posed of N atoms can be written in the following form:

$$V = aN + bN^{2/3} + cN^{1/3} + d; \qquad (2.12)$$

where the first term in the summation on the right hand side of the equation arises from the volume contribution, the second from the contribution from the cluster facets, the third is due to the edges and the last one to the vertices. Starting from the energy V, we define the average binding energy per atom (or, simply, binding energy) E_b as:

$$E_b = -\frac{V}{N}. \qquad (2.13)$$

Since the total energy V is by definition a negative quantity, the binding energy is always positive. In order to have an indication of the stability of a cluster of size N with respect to clusters of size $N-1$ and $N+1$, we define the second difference in binding energy as:

$$\Delta_2 E_b(N) = 2E_b(N) - E_b(N-1) - E_b(N+1), \qquad (2.14)$$

where $E_b(N)$ is the binding energy of a cluster of N atoms.

The lowest energy morphology for a cluster corresponds to the structure able to minimise the different terms of the summation in (2.12). It is not difficult to guess that in (2.12) the volume term and the latter three terms, which can be collectively classified as surface effects, are in competition. Clusters with low surface energies, in fact, must have quasi-spherical shapes in order to minimise the surface to volume ratio and they are expected to display close-packed facets. On the other hand, as we shall see, spherical-shaped close-packed geometries based on the icosahedral geometry determine an inevitable internal strain in the structure, which causes the volume contribution to the cluster energy to increase [2].

Unless the potential is very long ranged, the lowest energy structures are often based on some regular or semi-regular polyhedra such as the Platonic or Keplerian polyhedra [4], or on close-packed fragments of the bulk lattice [52].
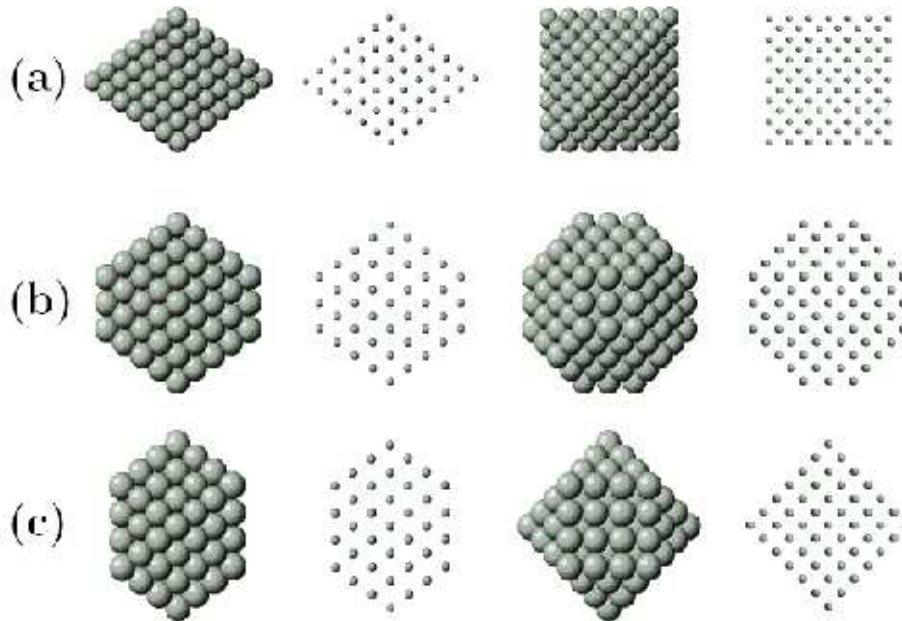
Figure 2.3: Spatial arrangements for clusters obtained from the fcc crystal lattice: (a) octahedron, (b) truncated octahedron, (c) cuboctahedron. (From Ref. [2]).

An explanation for the reason why nanoparticles prefer a regular shape in their growth will now be provided. Let us consider a closed-packed lattice: specifically we will assume the case of an fcc crystal. Let us imagine that we want to create a cluster out of that crystal. The most straightforward way to minimise the volume contribution is to cut out a piece of the bulk in order to leave inter-atomic distances unchanged. If we now want the surface contribution to the total energy to be as low as possible, we can think of a geometry where only close-packed facets are exposed. In the case of an fcc crystal crystal, the close-packed surfaces correspond to the family of (111) surfaces. A way to obtain from an fcc lattice a chunk of bulk exposing just (111) surfaces is the octahedral geometry (Fig. 2.3 (a)). Though having all the facets arranged in a close-packed fashion, the octahedron does not optimise the surface contribution to total energy of the cluster because of the high surface/volume ratio. A more spherical geometry based on an fcc crystal is thus the truncated octahedron, having eight (111)
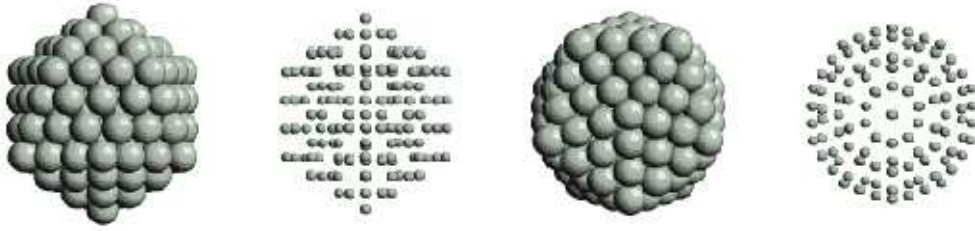
Figure 2.4: Icosahedral cluster. (From Ref. [2]).

hexagonal faces and six square (100) faces (Fig. 2.3 (b)). A truncated octahedron can be obtained by performing a cut of each of the six vertices of the octahedron in such a way that every cut plane intersects the edges of the octahedron at one third of their length. On the other hand, if the cut is performed in such a way that the cut planes intersect the edges of the octahedron at half of their length, then you end up with a polyhedron known as a cuboctahedron (Fig. 2.3 (c)). A cuboctahedron can alternatively be thought of as a regular octahedron truncated by a cube.

Since they do not possess translational symmetry, clusters are free to assume spatial arrangements which crystal lattices are not allowed to have. A good geometry which is able to accomplish the requirements of a compact quasi-spherical arrangement for the building elements of a cluster is the Mackay icosahedron (Fig. 2.4). Being a five-fold symmetric structure, the Mackay icosahedron is not a crystalline structure but it is an advantageous organisation for clusters in that it displays (111)-like facets only and enjoys a lower surface to volume ratio compared to fcc based structures.

One might think to construct a Mackay icosahedron from tetrahedra, namely by arranging twenty regular tetrahedra (one for each face of the icosahedron) in such a way that they can share a common vertex. This turns out to be impossible, since twenty regular tetrahedra packed in this fashion leave a gap between them which must be filled by a slight distortion of the tetrahedra (see Fig. 2.5). The reason for this is that the tetrahedron is not a space-filling geometric figure. Thus, in order to accommodate
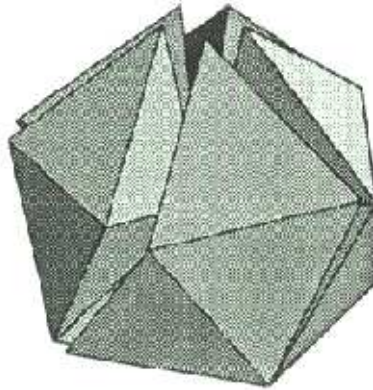
Figure 2.5:   Twenty tetrahedra sharing a common vertex leave a gap in the middle which must be filled by a slight distortion of the tetrahedra. This causes frustration of the packing. (From Ref. [3]).

a certain number of atoms in an icosahedral pattern one loses the ideal inter-atomic distance in the bulk of an fcc crystal. In other words, an icosahedral structure is one where an internal strain is present. When the size of the cluster is small, the lowering of the energy surface outweighs the increase in the volume energy due to the internal stress and the icosahedron turns out to be an advantageous arrangement. But as the size of the cluster increases, the internal strain also increases and there must be a crytical size beyond which the icosahedral structure is no longer stable.

Another non-crystalline structure which is possible to construct by the frustrated packing of tetrahedra is the decahedron, basically a pentagonal bipyramid (Fig. 2.6 (a)).

As for the octahedral geometry, the decahedron does not display an optimal surface to volume ratio, so several truncated versions of it have been constructed. The Ino decahedron is one of these (Fig. 2.6 (b)). It is obtained by cutting the five edges limiting the common basis of the two pyramids in such a way as to expose (100)-like faces. A more efficient truncation scheme has been proposed by Marks (Fig. 2.6 (c)). The Marks decahedron displays an alternating sequence of (100)-like and (111)-like reentrant facets in correspondence with the cut plane. Marks decahedra can optimise
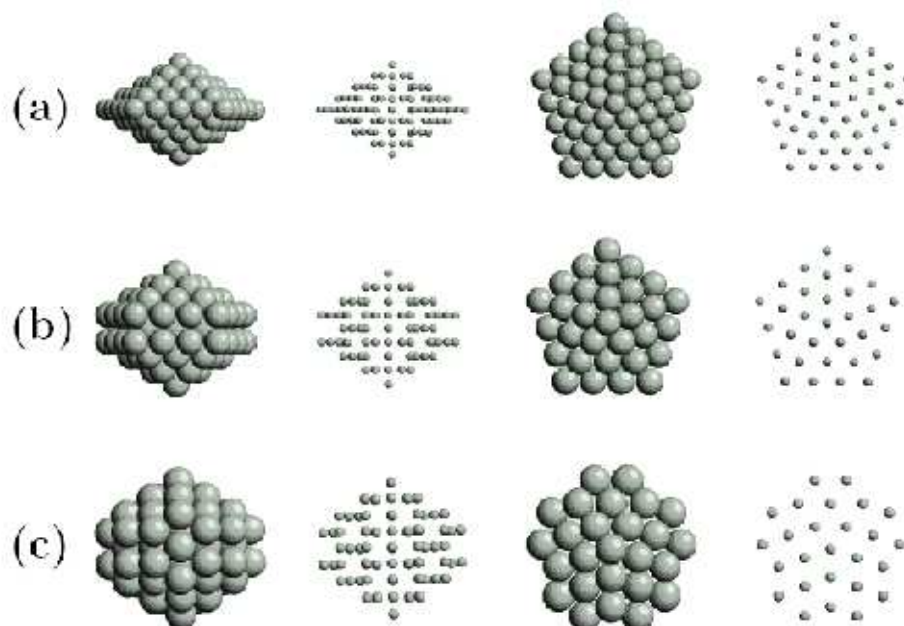
Figure 2.6: Different types of decahedral clusters: (a) regular decahedron, (b) Ino decahedron, (c) Marks decahedron. (From Ref. [2]).

the surface energy contribution better than truncated octahedron structures are able to do. On the other hand, decahedra, like icosahedra, are strained structures (Fig. 2.7), although they are less strained than icosahedra.

A comparison of the three described morphologies shows that the icosahedral structure maximises the coordination number but displays the largest strain. The truncated octahedron geometry, on the other hand, minimises the internal strain but has the smallest coordination number. The Marks decahedron is intermediate between these two structures.

Doye et al. performed molecular dynamics calculations using a Morse potential on clusters ranging from a few up to 80 atoms [53]. They have found that, given a fixed morphology, the strain energy increases as the range of the inter-atomic interactions decreases. Thus, long ranged interactions tend to favour strained non crystalline structures (i.e. icosahedra and decahedra), whereas short ranged potentials make crystalline close-packed structures more energetically favourable. Increasing the size of the cluster
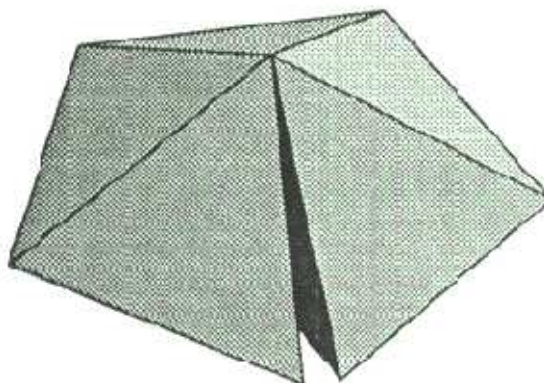
Figure 2.7:   Image illustrating the frustration of five tetrahedra sharing a common edge. The resulting geometric figure is almost, but not quite, a regular decahedron. (From Ref. [3]).

has a similar effect to decreasing the range of the potential.

2.5   Shells and magic numbers

It has already been pointed out that, being finite structures in space, clusters do not possess any translational symmetry. Yet experimental studies have revealed a sort of regularity in the distribution of cluster sizes. In particular, it has been noticed that cluster mass spectra of almost any material display intensity anomalies [4]. Mass spectra of rare gas clusters, for example, display peaks of intensity corresponding to well determined sizes (nuclearities). This behaviour can be explained if we imagine the cluster structure consisting of concentric layers of atoms arranged in a polyhedral pattern around a central atom. Borrowing the terminology from nuclear physics, the layers of atoms composing a cluster with the same geometrical spatial arrangement are given the name of shells. On the other hand, the nuclearities corresponding to clusters composed of a certain number of closed shells are known as magic numbers.

The Mackay icosahedral geometry described in the previous paragraph can easily be thought of as the composition of concentric shells. Considering a single atom as the first shell, let us arrange 12 neighbouring atoms at the vertices of a Mackay icosahedron
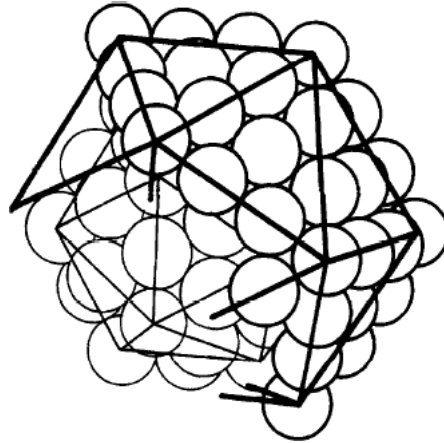
Figure 2.8:   Three-shell 55-atom icosahedron and a portion of the next shell. (From Ref. [4]).

around a central atom. These 12 atoms will then form the second shell. One can carry on building up a new shell of 42 atoms covering the 13-atom core thus forming a bigger icosahedron of 55 atoms. The construction of the following shells can be obtained in a completely analogous way (see Fig. 2.8).

If K is the number of closed icosahedral shells in a cluster, then the total number of atoms N turns out to be [4]:

$$N = \frac{10}{3}K^3 - 5K^2 + \frac{11}{3}K - 1; \qquad (2.15)$$

which sets the series of magic numbers for icosahedral clusters. These numbers turn out to correspond to the sizes for which mass spectra of rare gas clusters display significant peaks.

The construction of shells for the other two geometries described in Sect. 2.4 proceeds the same way as for icosahedral clusters. The magic numbers for the truncated decahedral and for the fcc octahedral geometries are provided, respectively, by the following expressions [4]:

$$N = \frac{10}{3}K^3 - 5K^2 + \frac{11}{3}K - 1 \qquad (2.16)$$

$$N = \frac{2}{3}K^3 + \frac{1}{3}K, \qquad (2.17)$$

where, as usual, K is the index of the shell and N indicates the total number of atoms in a closed-shell cluster. It should be noted that expression (2.16) is the same as (2.15), giving the series of magic numbers for icosahedral structures. In fact, this equation holds for every geometry based on 12-vertex polyhedra, i.e. icosahedral, truncated decahedral and cuboctahedral structures. These geometries have the same principal magic numbers, yet different patterns can be distinguished in experiments because of the presence of different series of secondary magic numbers due to sub-shell filling. Geometric sub-shells result from covering of individual faces or groups of faces of a polyhedron without giving rise to a complete polyhedral shell [51].

So far, only the spatial arrangement of the atoms constituting a cluster has been taken into account, but regular variations in cluster properties can also be due to the electronic structure. As well as having an atomic shell structure, clusters can possess electronic shells obeying their own periodicity rules. In the same way, experiments can reveal, besides geometric magic numbers, electronic magic numbers, corresponding to electronic shell closure. The main candidates to observe electronic shell effects are metals with weakly bound valence electrons, primarily alkali metals. In order to find a reason for the existence of electronic shells, the cluster is modelled as a sort of super-atom where valence electrons are delocalised in the cluster volume and fill discrete energy levels [2]. The electronic shell structure will not be discussed in any more detail, since it is likely that effects related to it are important only at temperatures at which the cluster is in the liquid state [51]. As our simulations are performed at absolute zero temperature, electronic shell structure may not be observed. The interested reader can find further details, for example, in the review by Baletto et al. [2] and references cited therein as well as in the book by Johnston [51].

Chapter 3

Structural optimisation of gold nanoclusters

3.1 Introduction

The present chapter is concerned with the structure of gold clusters. The first section introduces the reader to the field by displaying a survey of the previous work on gold nanoparticles. Particular attention has been reserved to theoretical investigations carried out within a semiempirical potential scheme. In Sect. 3.3 the results obtained in my simulations are presented and the procedures of calculation explained. Sect. 3.4 contains a discussion of the results found in this work and compares them with other analogous studies. Finally, in Sect. 3.6 the conclusions on the work carried out on nanocluster optimisation are drawn and some suggestions for future work are given.

3.2 Previous results for gold clusters

New molecular nanocrystalline materials using gold nanoclusters as building blocks have recently been synthesised, paving the way to the realization of a new generation of electronic nanodevices and biosensors [54–56]. This has motivated a number of experimental and theoretical studies. Experimentally, the most common techniques to investigate the properties of small gold clusters are X-ray powder diffraction [57], scanning tunneling microscopy and high resolution scanning electron microscopy [58].

On the theoretical side, calculations based on both first principles density functional theory and semiempirical many-body potentials have been carried out.

This section provides a comprehensive view of the current debate about the most common structural motifs of gold clusters ranging from the size of a few up to a few hundreds of atoms. As we will see, in spite of all the experimental and theoretical effort spent in the last ten years, the lowest-energy structures of gold nanoclusters is far from being clear.

Garzón's group performed several unconstrained searches for the global minimum of small gold clusters using a Gupta-like many-body potential to simulate interatomic interactions. In one of the first of these works, an analysis of the structures and of the vibrational frequencies of the lowest-energy isomers of Au_{55} nanocluster is presented [59]. Using simulated annealing combined with a simulated quenching technique within the framework of molecular dynamics, the potential energy surface of Au_{55} was explored in a search for the global and other low-lying local minima. This kind of investigation shows that the global minimum corresponds to an amorphous structure and that the Mackay icosahedron, the lowest energy highly symmetric isomer, is only the fourth most stable structure. All these isomers, though, are very close to each other in energy, with the difference in binding energy between two structures being of the order of 1 meV/atom or less.

In a later work by the same group, the most stable structures of Au_{38}, Au_{55} and Au_{75} were investigated starting from potential energy surfaces again generated by the Gupta potential [60]. The sizes were not chosen at random. In fact 38 is the magic number associated with the truncated octahedron with hexagonal and square facets obtained from the four-shell octahedron (cfr. (2.17)). On the other hand, 55 and 75 are still magic numbers associated, respectively, with the two-shell icosahedral geometry and the Marks decahedral geometry (cfr. (2.15) and (2.16), respectively). In this paper, the results obtained by the molecular dynamics simulated annealing were com-

pared to those produced using a genetic algorithm and density functional theory based on first-principle calculations. It was found that while for Au_{38} and Au_{55} the most stable structures were amorphous, the global minimum of Au_{75} is arranged in a Marks decahedral pattern. In all three cases, a set of isomers nearly degenerate in energy with the global minimum was found. The 100 lowest-energy configurations, for example, turned out to differ by less than 10 meV/atom from the global minimum. All of the employed techniques have agreed about the same conclusions.

The comparison of the lowest-energy structures of Ni, Ag and Au clusters in the size range from 6 to 75 atoms was the object of another paper [61]. A genetic algorithm was used to locate the global minima of the clusters, where the interaction are modelled by means of the Gupta potential. Regarding the range of nuclearities we are interested in ($N \geq 38$), the structures of the magic sizes 38, 55 and 75 were studied for all three metals. Ni and Ag were found to prefer highly symmetric lowest-energy structures for the 38 and 55 nuclearities, assuming, respectively, the truncated octahedral geometry and the Mackay icosahedral geometry. Au clusters of the same size, on the other hand, displayed amorphous global minima, as had been seen in the previous study. The results for clusters of the three metals composed of 75 atoms revealed that the most stable common structure for all of them is the Marks decahedron. In the case of Au_{75} though, many disordered isomers of almost identical stability to the global minimum were found. From this study it is concluded that the structure of the lowest-lying energy minimum is a sensitive function of the form of the potential. In the case of the Gupta potential, the dominant role is played by the two parameters p and q (see Sect 2.2), which differ for the three metals here studied. In particular, since p is pretty much the same for the different metals, the main responsible for the different structures of the most stable isomers appear to be the parameter q, determining the spatial range of the many-body inter-atomic interactions. The preference for disordered asymmetric structures of gold was thus attributed to the short range of its inter-atomic forces as

compared to nickel and silver.

This latter point was developed in later works both by the same and different groups. In fact the effects of the range of the potential on the structure of clusters had been a field of intense study well before the publication of the papers by Garzón and colleagues. A remarkable contribution was given by the works by Doye and colleagues [53, 62], who simulated the structure of clusters of up to ≈ 80 atoms using the pairwise Morse potential. By varying the only parameter upon which the range of the Morse potential depends, the authors concluded that decreasing the range of the potential results in destabilising strained structures. For very long-ranged potentials the most stable structures are highly strained, highly coordinated with low symmetry. At intermediate ranges of the potential icosahedral structures are dominant. If the range of the potential is decreased further, first decahedral and then fcc structures are favoured.

The Sutton-Chen many-body potential was later employed by the same authors to model the structure of noble metal clusters within the same size range as in the previous work [63]. As compared to the other metals investigated, Sutton-Chen gold clusters seem to display a clear prefence for fcc structures rather than quasi-crystalline structures. A tendency to form structures which are not identifiable with any of the ordered morphologies was also noticed.

Garzón's group recently attempted to give a reason based on quantitative arguments for the preference for low-symmetric structures of small gold clusters, as observed in their simulations [64]. One might think that the most important factor determining the cluster morphology is the surface reconstruction, trying to increase the coordination of the outermost atoms. This was proven not to be the case, as demonstrated by the most stable amorphous structure of Au_{55}, whose surface coordination is certainly lower than in the two-shell icosahedron, which is the lowest-lying ordered isomer for this nuclearity. The main force giving rise to the low-symmetry configurations in gold

clusters was thus identified as an elastic energy contribution. In fact metals were shown to display a tendency to contract their surface inter-atomic bonds in reply to a decrease in coordination. This behaviour is a direct consequence of the character of the metallic bond, which many-body potentials are able to reproduce and pairwise potentials are not. In this picture, the higher abundance of amorphous structures is to be expected for those metals for which the tendency to the contraction of inter-atomic lengths as a result of a decrease in coordination is higher. Within the Gupta potential scheme, this tendency was shown to be higher in gold than in the other noble and quasi-noble metals investigated. Furthermore, gold was observed to display the lowest energetic cost of amorphisation among all the studied metals.

A recent paper by Baletto et al. [65] addressed similar issues as it focused on the crossover among structural motifs taking place in cluster structures as cluster sizes increase. Several metals, including Cu, Ag, Au, Pd and Pt, were investigated synoptically in a search for the most stable structure in the size range up to $\simeq 40000$ atoms. By using the Gupta potential and the Embedded-Atom Method (EAM) [36], the three most common structures for cluster morphologies were compared, i.e. the icosahedral, decahedral and close-packed fcc-based octahedral geometries. The expected trend is that small clusters generally assume the icosahedral geometry and, as long as the size increases, a gradual shift to decahedral-based and, eventually, to fcc structures is displayed. Although this overall trend seems to be generally followed, the conclusion of the study is that the size interval in which a kind of structure is favoured strongly depends on the metal. Cu and Au represent the two extreme behaviours, since the former prefers strained icosahedral arrangements up to sizes of the order of 10^3 atoms, whereas the latter seems to favour fcc structures already at sizes larger than 600 atoms. A simple model was then developed to give an account for the observed differences in crossover sizes. The idea behind the model is that crystals strongly increasing their internal energy for a change in interatomic distances (crystals bound by *sticky* inter-

actions) are expected to have smaller crossover sizes than crystals bound by less sticky interatomic potentials. The quantity responsible for the crossover size was thus taken as proportional to the difference between the energy of the bulk crystal where all the interatomic distances have been changed by the same infinitesimal amount, and the energy of the bulk crystal at the equilibrium. This quantity turns out to be proportional to the product pq of the two free parameters of the Gupta potential. In fact this product was a maximum in the case of gold and minimum in the case of copper, among all the metals considered in the investigation.

Darby et al. [66], in their study of Cu-Au alloy nanoclusters, also carried out simulations of small gold clusters using a genetic algorithm and the Gupta potential. The paper spans the size range from 10 to 56 atoms. Comparison with the analogous series of simulations performed for copper clusters revealed that, in contrast to copper, gold clusters do not adopt a single structural motif but rather prefer low-symmetry structures. This general conclusion is in agreement with the results found by Garzón's group. On the other hand, a disagreement with the simulations carried out by this same group arised for the structure of Au_{38} cluster. While Garzón's group concluded that the most stable structure for this nuclearity is amorphous, Darby and colleagues found the truncated octahedron to be the global minimum for Au_{38}. This discrepancy was attributed to a small difference in the form of the Gupta potential used for the two studies and, above all, to the slightly different values for the parameters of the potential. This is a strong indication of the fact that high and low-symmetry structures are in close competition, and that the global minimum is sensitive to fine details of the potential parametrisation.

To conclude the present review, we consider a recent paper where the global minima of Al_N, Au_N and Pt_N, with N between 2 and 80, were compared [5]. An algorithm based on the Monte Carlo simulation technique, in conjunction with a particular parametrisation of the EAM, were chosen for the search of the most stable structures. Most

of the lowest-energy configuration for gold clusters were found to have low symmetry, in agreement with previous work. Furthermore, the most stable structures in the range investigated do not display a clear correlation with magic sizes or high symmetry geometries.

3.3   Results of genetic algorithm optimisations

Simulations were carried out to locate the global minima of Au_n in the size range 54 up to 80 atoms. The investigation was performed by means of the Birmingham genetic algorithm program described in Sect.2.3.2.

For every genetic algorithm run, an initial randomly generated population composed of 20 individuals was allowed to evolve through 100 generations. After the fitness of each member of the population was assessed using a hyperbolic tangent (tanh) function, the selection of the clusters due to undergo the mating operation was accomplished by roulette wheel selection. The mating, using the one-point crossover operator, gave rise to an amount of offspring equal to 80% of the total population. Newly created clusters, before undergoing the minimisation process, had a probability of 10% of being mutated by being replaced by completely new, randomly generated clusters. Different mating and crossover operators were tried for the nuclearity 79. The results did not prove to display any substantial variation with the combination of mutation and crossover operators employed. For every nuclearity, 200 cluster GA runs were performed, each time starting from a different initial population.

The inter-atomic interactions were modelled by the Gupta potential. In Table 3.1 the parameters used in the present work are quoted and compared with the parameterisation employed by other groups which carried out simulations of metal nanocluster within the Gupta potential scheme.

In what follows, the results obtained in our simulations are presented and discussed. Table 3.2 summaries the outcomes of our simulations by listing the lowest energy and

	A (eV)	ζ (eV)	p	q	Ref.
This work	0.2096	1.815	10.139	4.033	[67]
Cleri and Rosato	0.2061	1.790	10.229	4.036	[42]
Garzón et al.			10.15	4.13	[60]
Baletto et al.	0.2197	1.855	10.53	4.30	[65]

Table 3.1: Parameters for the Gupta Au potential used in the present work (first row) and in previous works.

the structure of the lowest lying isomer for each of the investigated nuclearities. In all cases, the point groups of the most stable isomers are quoted, along with the type of geometry on which the structure is based. Figs. 3.1, 3.2 and 3.3 display the geometries of the global minima found by the GA in the investigated range.

3.4   Discussion of the results

The results obtained for the structural optimisation of gold nanoclusters will now be discussed by describing the morphologies of the lowest-lying isomers associated with the different cluster sizes and pointing out regular trends. The 53-atom cluster is clearly a fragment of the 55-atom centred icosahedron, even if fairly distorted. In the whole studied size range, this is the only case when an icosahedral-like morphology has been found. Nuclearities 54, 55 and 56 display cubic close-packed global minima with different degrees of symmetry. The most regular of them is the 56-atom cluster whose structure is based on a truncated rectangular bipyramid.

With the exception of nuclearity 58, the most stable structures in the range from $57 - 61$ are low-symmetry structures constructed about a 5-fold axes. The larger the size, the more the structure resembles the Marks decahedral geometry. In fact, starting

N	V(eV)	Point Group Symmetry	Structural Assignment
53	-183.939460	C_s	ico
54	-187.520286	C_{2v}	fcc
55	-191.003676	C_1	fcc
56	-194.690945	D_{2h}	fcc
57	-198.239046	C_{2v}	dec
58	-201.759934	C_s	fcc
59	-205.334306	C_{2v}	dec
60	-208.927959	C_{2v}	dec
61	-212.442831	C_s	dec
62	-216.159808	C_s	fcc
63	-219.691567	C_s	dec
64	-223.473514	C_{2v}	dec
65	-226.997990	C_{2v}	dec
66	-230.610708	C_s	dec
67	-234.175279	C_{2v}	dec
68	-237.744399	C_s	dec
69	-241.318903	C_1	dec
70	-244.956521	C_s	dec
71	-248.730652	C_{2v}	dec
72	-252.253160	C_s	dec
73	-255.861431	C_s	dec
74	-259.490527	C_{5v}	dec
75	-263.271836	D_{5h}	dec
76	-266.792504	C_{2v}	dec
77	-270.313449	C_{2v}	dec
78	-273.838181	C_s	dec
79	-277.627474	O_h	fcc
80	-281.100570	C_{4v}	fcc

Table 3.2: Table summarising the results for small gold cluster structures. The first column lists the nuclearity, the second the minimum total binding energy found in the several different runs of the GA, the third column describe the point group symmetry of the structure associated with the lowest energy found. Symmetries are assigned by inspection. In the fourth column the structural assignment of the most stable isomers has been given. The structural categories are: icosahedral based structures (*ico*), Marks decahedral structures (*dec*) and cubic close-packed structures (*fcc*).
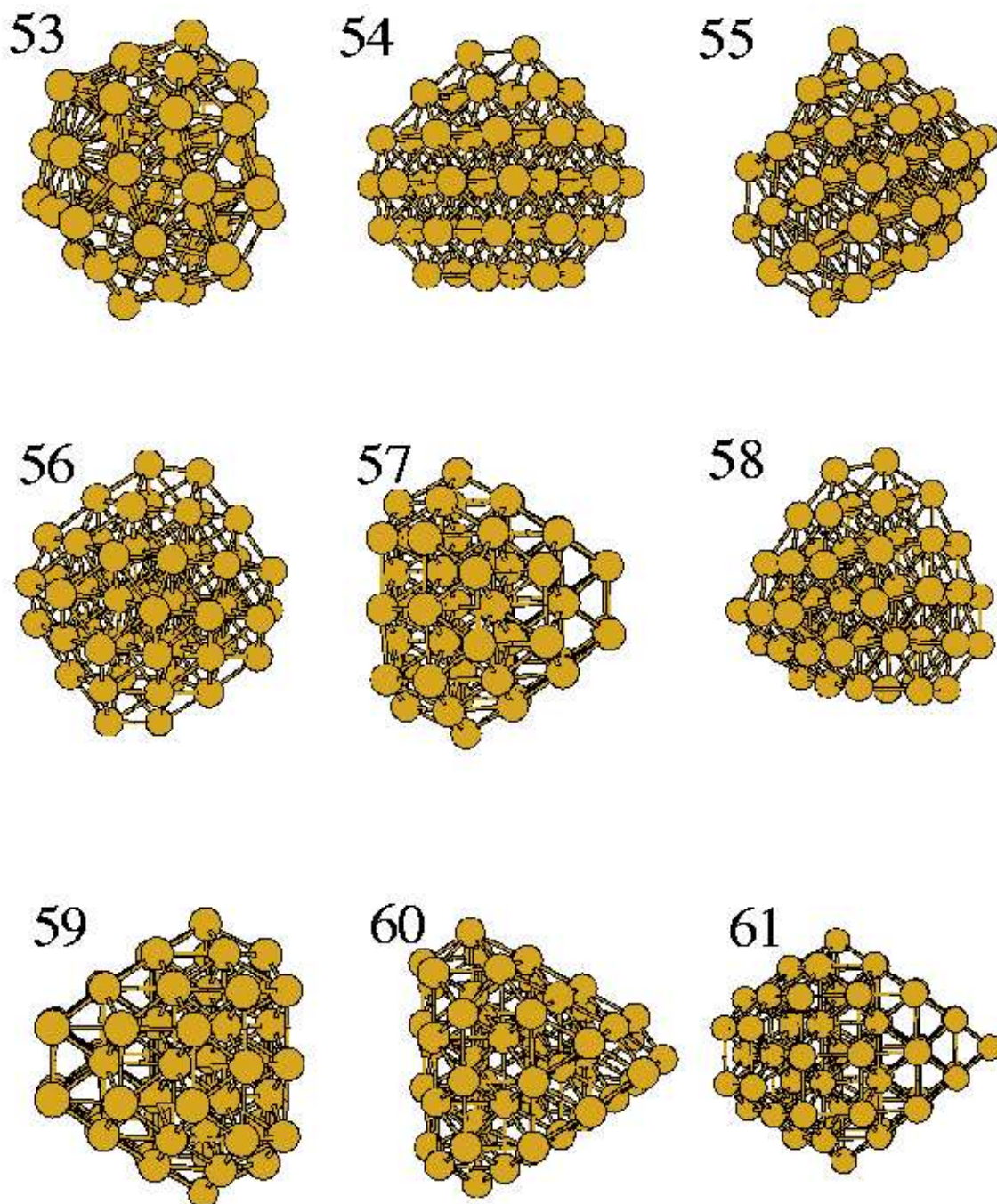
Figure 3.1: Most stable structures obtained from the simulations for the nuclearities from 53 to 61.
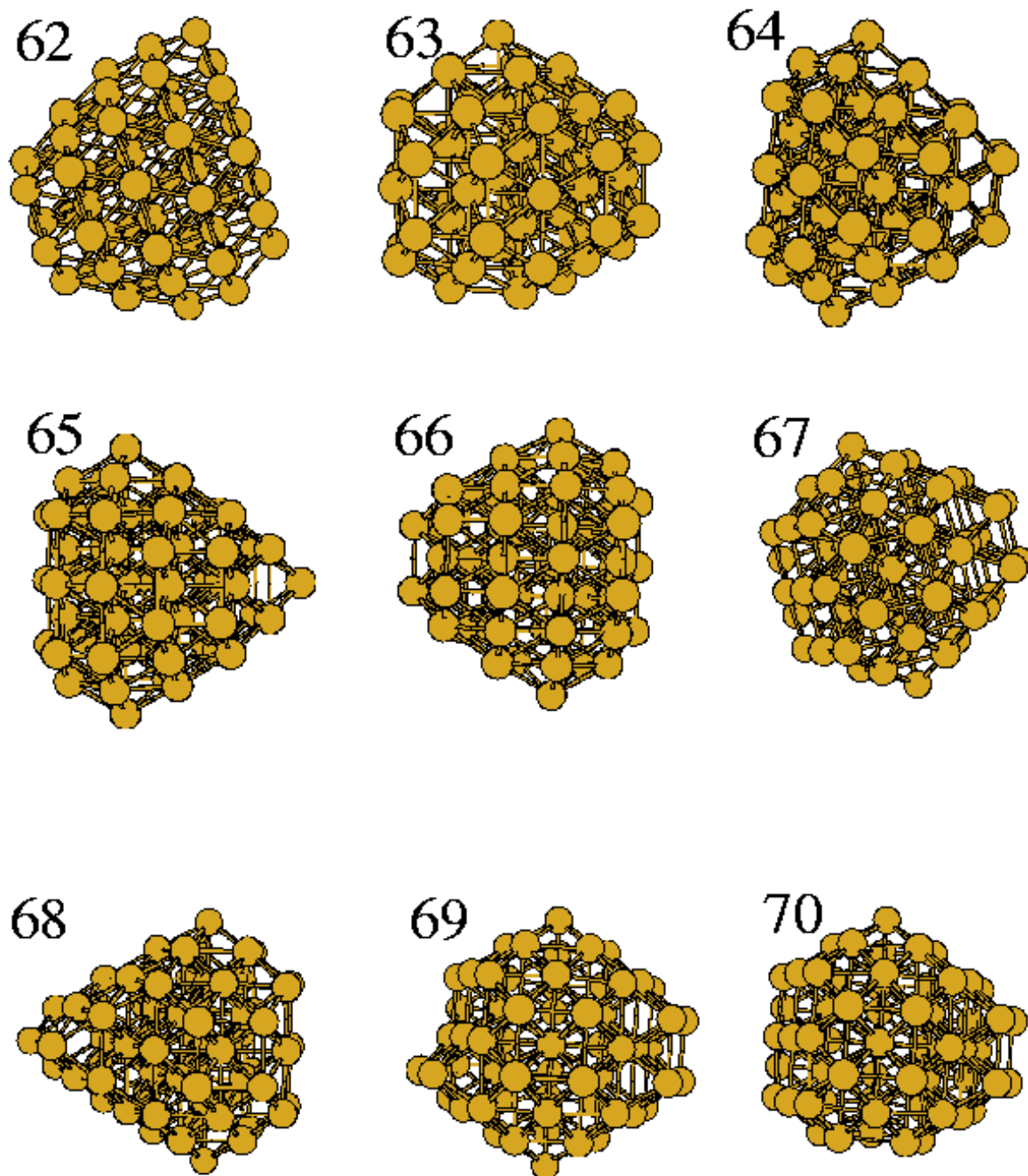
Figure 3.2: Most stable structures obtained from the simulations for the nuclearities from 62 to 70.
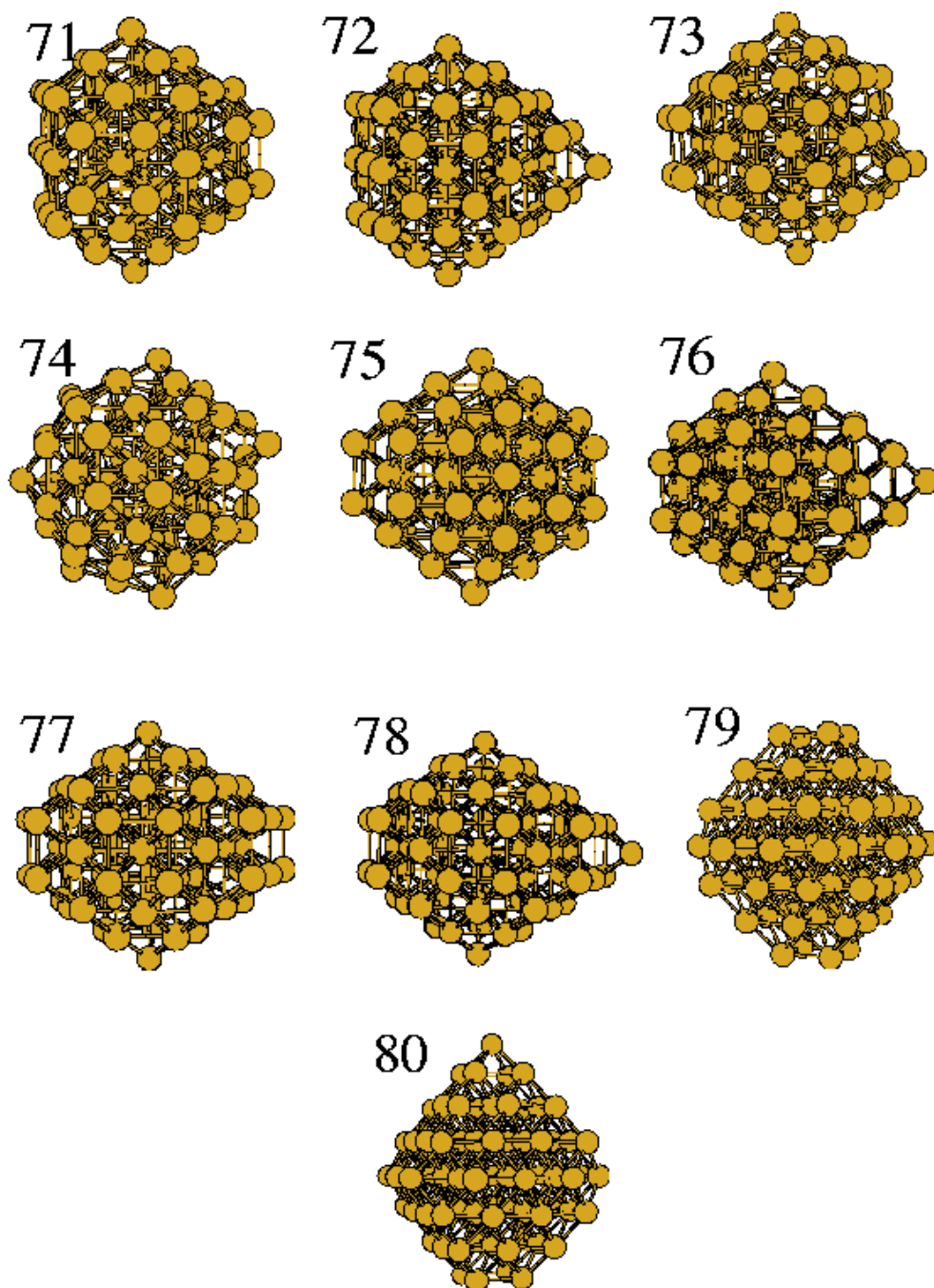
Figure 3.3: Most stable structures obtained from the simulations for the nuclearities from 71 to 80.

from cluster size 57 and excluding the 58- and the 62-atom clusters, the morphologies of the global minima seem to follow a trend culminating with the 75-atom Marks decahedron with 5 atoms lying on the principal axis. All these structures turn out to be based on the Marks decahedral geometry, although having much lower symmetry than the D_{5h}-Marks decahedron, due to distortion or truncation of vertices or faces. The three nuclearities following the 75-atom cluster are also easily obtained from the Marks decahedron by the addition of extra atoms on top of the square or the reentrant faces.

The 58-atom cluster, as has already been said, constitutes an exception to the general trend, as it is a low-symmetry structure based on fcc packing. The lowest energy isomers for Au_{79} and Au_{80} are also fcc based structures. The global minimum of the 79-atom cluster is obtained by truncating the 5-shell regular octahedron in such a way as to deprive it of the 6 vertex atoms. This and the Marks decahedron are the only highly symmetric structures found in the studied size range. Finally, the global minimum of Au_{80} is obtained by adding an extra atom on top of one of the square faces of the Au_{79} truncated octahedron.

Our results are in fair agreement with the existing literature on gold cluster structures, above all regarding the basically amorphous structures of gold clusters which is to be expected in the size range below a few hundred atoms. As already pointed out, most global minima found by the GA display low, if any, symmetry. This seems to be a well known and widely observed characteristic feature of gold, whose strong interatomic interactions as compared to other transition and noble metals, tend to destabilise highly symmetric, strained geometries in favour of amorphous or low symmetry structures [2, 5, 60, 61, 64, 66].

In the parameterisation which has been adopted for this study, the Gupta potential has predicted, for gold clusters in the size range from 53 to 80, a clear preference for configurations based on the decahedral motif. This might seem surprising at first,

considering that many other transition metals such as, for example, nickel, copper and silver appear to prefer icosahedral-like geometries for nuclearities around 55. But this apparent contradiction can again be explained by the sticky character of the gold interatomic forces. So, while icosahedral geometries are rejected, slightly strained decahedral and strainless fcc structures are accepted.

We also agree with previous work on the most stable structures associated with the magic sizes 55 and 75, which we have predicted to have, respectively, amorphous and Marks decahedral morphologies, in line with the papers by Garzón and coworkers [60] and Sebetci and coworkers [5]. The latter work, in particular, displays a particular interest for us, since in it the authors performed an extensive unconstrained search for the global minima of gold clusters with nuclearities up to 80. The model used is a particular version of the EAM, therefore it is of interest to compare the results quoted in that paper with ours.

In agreement with our results, Sebetci and colleagues identified the dominant structural motif in the range between 64 and 79 as the decahedral morphology. Furthermore, the low-lying isomers in this size range display low symmetry, as almost all of them belong to the C_s point group. Compared to these results, the structures found in this study for the same size range appear to preferentially arrange themselves around higher symmetry elements.

Ours and Sebetci's results also agree in predicting the most stable structure of Au_{79} as a truncated octahedron. Yet, at odds with our calculations, only two fcc structures above the size 38 were found by the EAM: namely the 61- and the already mentioned 79-atom clusters. This might be due to a difficulty in locating fcc-type global minima in the study using the EAM potential. In fact, the fcc-based morphology for Au_{80} found by us has been confirmed by Sebetci himself to be more stable for the EAM potential than the global minimum located in the original study [68].

One more notable difference concerns the structures around size 55. Our simulation

runs have provided morphologies arranged in a cubic close-packed fashion for the nucle-
arities between 53 and 56, whereas the EAM study predicted icosahedral morphologies
for the 53- and 54-atom clusters. In particular, the global minimum for nuclearity 54
turned to be an uncentred icosahedron, i.e. a 55-atom three-shell icosahedron deprived
of the atom in the middle. As for the sizes 55 and 56, Sebetci found low-symmetry mor-
phologies without a clear reference to any known structural motif. It is worth pointing
out, however, that 55 turns out not to be a magic size for gold clusters both in our
predictions and in those by Sebetci et al., in agreement with previous studies [60,66].

In Fig. 3.4 the second difference in binding energy (see (2.14)) is plotted for the
data obtained in this work (black line) and for the data quoted in Ref. [5] (red line).
As expected, the 54-atom cluster is particularly stable in the EAM scheme, since it is a
perfect icosahedron, but not according to the Gupta potential investigation. Peaks in
the second difference in binding energy have been found in this study associated with
nuclearities: 56, 62, 64, 71, 75 and 79. Apart from the 62-atom cluster, which is a
fcc structure lying between two decahedral morphologies, the most stable nuclearities
correspond to structures with higher symmetry than their neighbouring lowest-lying
isomers. The global minimum for size 56, for example, is an fcc-based structure with
D_{2h} symmetry and the 75- and 79-atom clusters are associated, respectively, with the
Marks decahedron and the truncated octahedron described above. On the other hand,
while agreeing with us in identifying the 75-atom Marks decahedron as a particularly
stable structure with respect to disproportion, the investigation carried out by Sebetci
and coworkers found peaks in the second difference which are not clearly associated with
any particular structural motif nor have a higher symmetry than their neighbouring
nuclearities. This is the case for the 66-, 73- and 77-atom clusters.
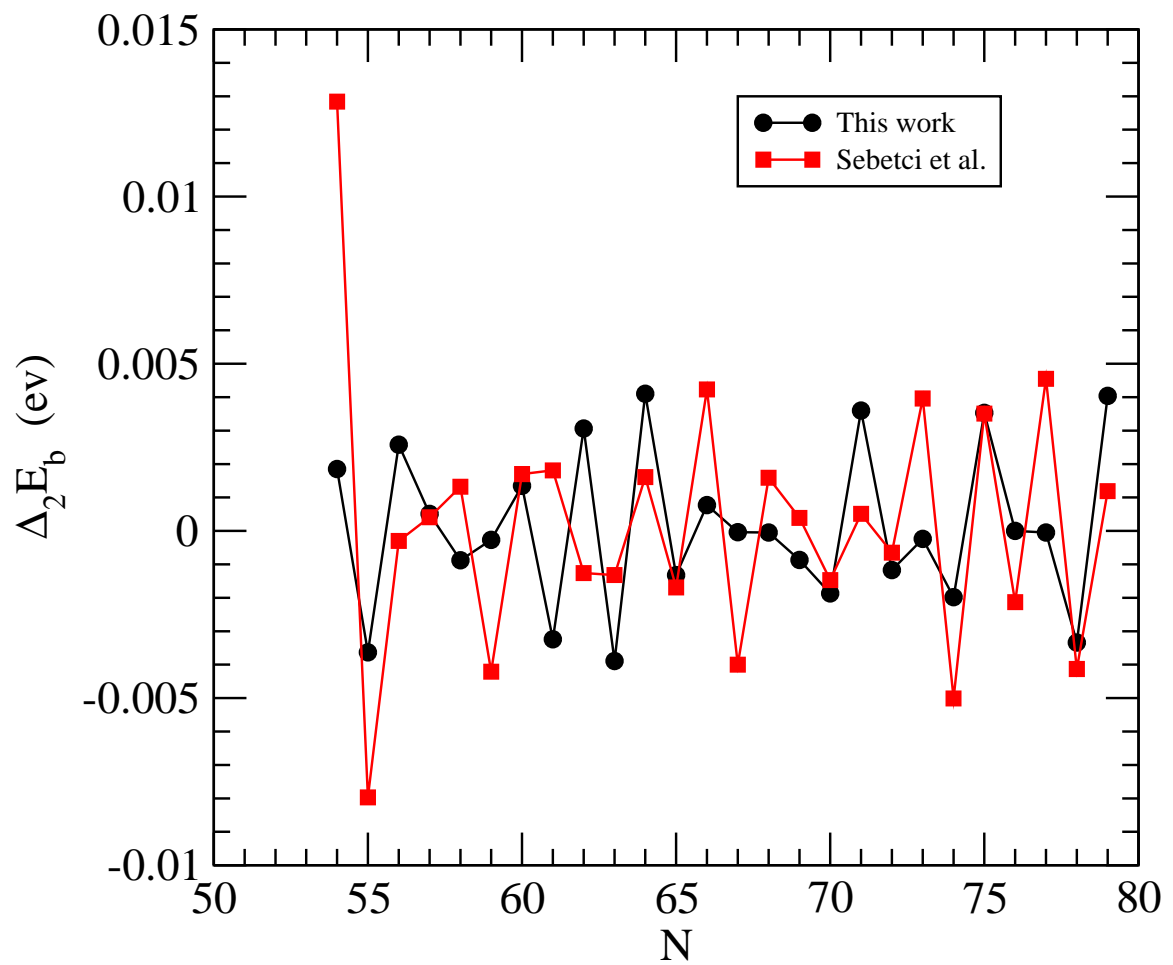
Figure 3.4: Second difference in energy for the size range between 53 and 80. Black line: this work. Red line: data plotted from Ref. [5].

3.5   Estimate of cohesive and surface energy

By combining the two equations (2.12) and (2.13), the following expression for the binding energy as a function of the nuclearity is obtained:

$$E_b = -a - bN^{-(1/3)} - cN^{-(2/3)} - dN^{-1}, \tag{3.1}$$

where the parameters a, b, c and d have the same meaning as in (2.12).

Provided that in the size range studied the last two terms can be expected to give little contribution, the dependency of the binding energy on the nuclearity can be approximated by a linear one in $N^{-(1/3)}$. Thus, provided that $N \gg 1$, the binding energy can be further approximated as:

$$E_b \approx E_c - bN^{-(1/3)}, \tag{3.2}$$

where E_c is the cohesive energy per atom in the crystal bulk.

In Fig. 3.5 the binding energy as a function of $N^{-(1/3)}$ have been plotted, both for our data (black circles) and for the results reported in Ref. [5] (red squares). The two sets of data have then been fitted to a linear spline; the two best fit lines are also shown.

A linear fit of the data found in this work to (3.2) provides for E_c the value of 3.84 eV, which is fairly close to the value of 3.81 eV given by Kittel [69] as the bulk cohesive energy per atom in gold. Fitting the set of data obtained by Sebetci et al., on the other hand, gives the value 4.04 eV as the best estimate for the parameter E_c, which is significantly different from the experimental value.

The coefficient b in (3.2) provides an indication of the surface energy, being the contribution in $N^{-(1/3)}$ to the binding energy due to surface effects. In fact, a simple phenomenological model predicts the surface energy to be proportional to b. This model is the extension to clusters of a scheme which can be applied for the calculation of the surface energy E_s of an infinite 2-dimensional slab, based on an N-atom slab with
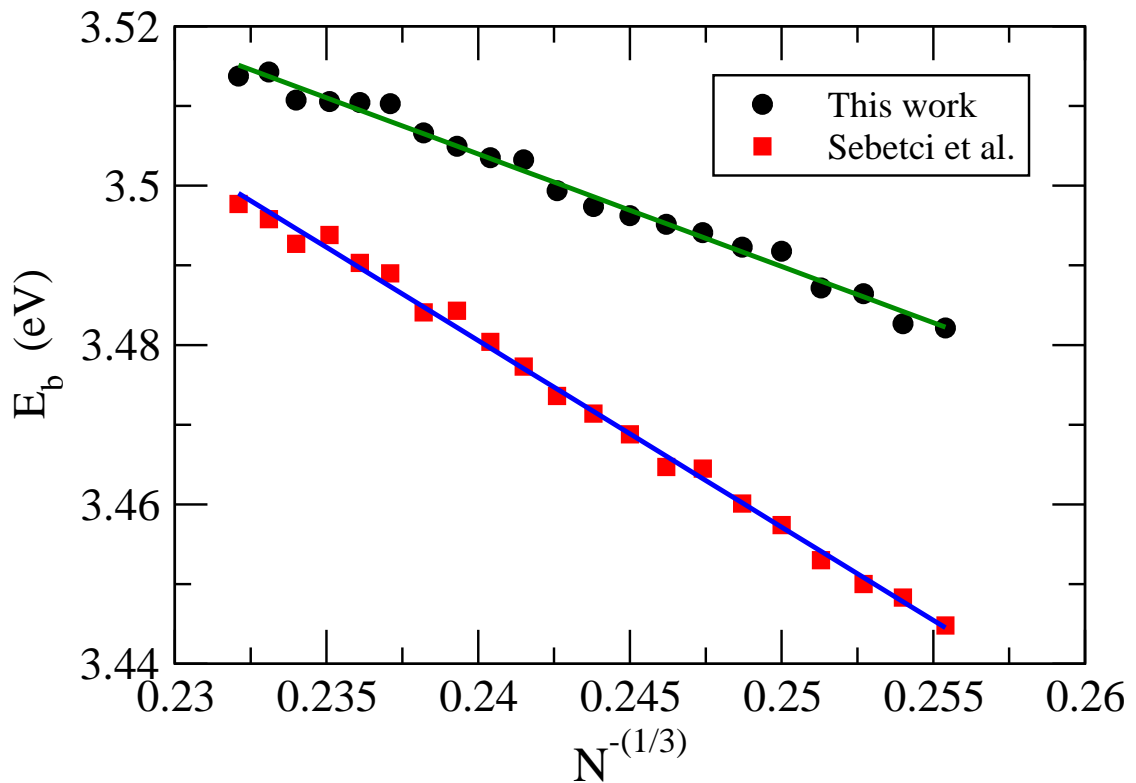
Figure 3.5:   Binding energy plotted as a function of $N^{-(1/3)}$. The minimum energies found in this study are shown as black circles, whereas the values quoted in Ref. [5] have been plotted as red squares. The best linear fits to the two sets are also reported: green line for the fit to my data and blue curve for the fit to data in Ref. [5]
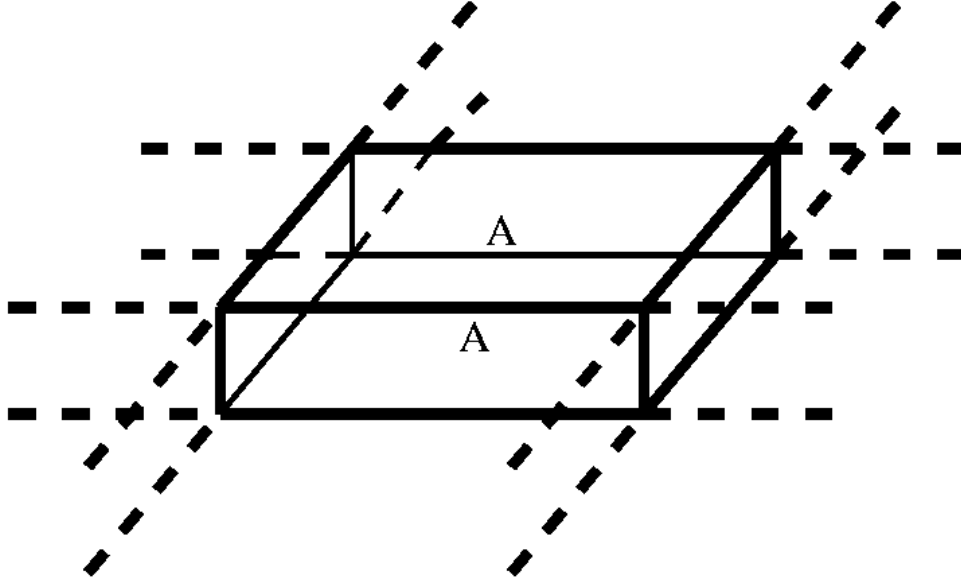
Figure 3.6:   Schematical depiction of the infinite slab considered in the model. The quantity A indicates the area of both the top and the bottom surfaces.

2-D periodic boundary conditions. In this picture, if E_c is the bulk cohesive energy of the crystal, the surface energy can be expressed as the difference between the energy of the slab considering all atoms as bulk atoms, NE_c, and the actual potential energy of the slab, V_{slab} (by definition a negative quantity), in the following way:

$$E_s = \frac{NE_c + V_{slab}}{2A}, \tag{3.3}$$

where A is the area of a slab surface.

This approximate expression for the surface energy can be extended to clusters of atoms with surface area A_c. If in (3.3) we substitute the corresponding quantities for the cluster, we obtain the following equation for the surface energy:

$$E_s = \frac{NE_c + V_{clust}}{A_c}. \tag{3.4}$$

Now, taking into account that the surface area of a pseudo-spherical cluster can by approximated in the following way:

$$A_c \approx N^{2/3} 4\pi r^2, \tag{3.5}$$

where r is the atomic radius of an atom in the cluster, and that, by definition (see (2.13)), the expression

$$V_{clust} = -NE_b \tag{3.6}$$

holds, we can rewrite (3.4) as:

$$E_s = \frac{N^{1/3}\left(E_c - E_b\right)}{4\pi r^2}. \tag{3.7}$$

Let us then consider the expression (3.2) for the approximate binding energy of a cluster. By inserting this equation in (3.7) one obtains:

$$E_s = \frac{b}{4\pi r^2}, \tag{3.8}$$

which is the sought expression.

Using for the atomic radius the value of 1.44 Å found in Ref. [69], and for the value of b the estimate of the linear fit, we obtained for the surface energy the value $55.1\,\mathrm{meV/\mathring{A}}^2$, clearly below $96.8\,\mathrm{meV/\mathring{A}}^2$, which is the value quoted in the literature [70] for the surface energy of gold. The prediction obtained by the set of data in Ref. [5] is closer to the expected value. Following the same procedure as for my data, the surface energy calculated from the data by Sebetci et al. turns out to be $89.8\,\mathrm{meV/\mathring{A}}^2$.

3.6   Conclusions and future work

I have investigated the most stable structures for gold clusters, with between 53 and 80 atoms, using a genetic algorithm within the Gupta potential model. This work can be considered the natural extension of that carried out by Darby et al. [66], where the same search mechanism and the same potential were used for the optimisation of clusters in the size range $10 - 56$ atoms. Notably, the results quoted in Ref. [66] have been improved by finding lower lying minima for the nuclearities 54, 55 and 56. The structures reported by Darby and coauthors have been found to be higher lying local minima.

The most frequently encountered structural motif in the investigated range is the decahedral morphology. Fewer clusters have turned out to prefer the cubic close-packed arrangement, whereas only in the case of the 54-atom cluster has a structure based on the icosahedral geometry been found.

The comparison with previous studies of gold clusters highlights the fact that the structure of gold clusters is extremely sensitive to the choice of the potential and even to slight changes in the parameters within the same potential. This is the case for the Gupta potential, for example, for which fine details in the parameterisation can dramatically affect the morphology of the global minimum [2,61,65].

A Monte Carlo optimisation of clusters in the same size range as ours carried out using an EAM potential [5], allowed us to test the reliability of the GA, since the global minimum found in our investigation turned out to be lower in energy for the EAM potential than that originally obtained. Though in overall agreement with ours, the results obtained in the EAM study indicates a higher tendency for this potential to find amorphous global minima as compared to the Gupta potential. Moreover, the occurrence of morphologies based on the cubic close-packed spatial arrangement turned out to be higher in our investigation as compared to that carried out by Sebetci and colleagues.

To extend this study, it would be of interest to investigate the low-energy minima (both global and local) predicted by the Gupta potential and EAM potential using Density Functional Theory (DFT). DFT alone is too expensive to perform a full search of the energy surface, but coupling semiempirical potentials and DFT is expected to be a more efficient way of finding the global minimum on the ab initio energy surface. The procedure to combine semiempirical and first principles approach is to initially generate a family of lowest energy isomers of a cluster by means of a global optimisation performed using a semiempirical potential. The structures thus obtained can then be locally optimised at a higher level of theory such as DFT. This second ab-initio

optimisation establishes a new energetic ordering in the set of isomers located within the semiempirical potential scheme. Investigations aimed at combining semiempirical and ab-initio methods have been recently attempted on bimetallic clusters [71–73].

Chapter 4

Nanofinger growth on Au(111)

4.1 Introduction

This chapter is an introduction to the basic themes and aims of the surface physics related research carried out during this thesis. The motivation for this work came from an experimental study in which, after scanning a Au(111) surface by a scanning tunneling microscope (STM) [74,75] under particular conditions of voltage and current, nanoscale ordered structures were seen to form in a reproducible way. The main goal of this research project was thus to provide a theoretical explanation for the growth of these nanostructures.

In Sect. 4.2 some examples of finger patterns found in nature will be presented and will be explained in terms of kinetic instabilities of an interface. Particular regard will be given to the meandering instability of a step edge during crystal growth.

Sect. 4.3 will describe the Au(111) surface and its elusive reconstruction. Finally, in Sect. 4.4 the experiment of nanofinger growth will be reviewed.

4.2 Finger formation and kinetic instabilities

4.2.1 Finger pattern in nature

Fingers are one of the patterns that nature seems to form spontaneously [76] and can be found in a wide range of physical systems. Fingering, for instance, is observed when a thin viscous liquid film is allowed to flow down an inclined plane under the effect of

gravity [6, 77] (Fig. 4.1 (a)). Another known case where a fingering instability shows up is in a Hele-Shaw cell, which is formed by two parallel plates with a gap between them of a thickness smaller than all other length scales in the system. The cell can be given either a rectangular or a circular geometry. When two immiscible fluids are introduced into the cell, the instability arises due to a pressure gradient advancing the less viscous flow towards the more viscous [78, 79]. Alternatively, one can fill a Hele-Shaw cell, previously tilted with respect to the horizontal plane, with a denser fluid on the upper part and an immiscible less dense fluid on the lower part. The denser fluid naturally flows towards the less dense one as an effect of gravity, thus again giving rise to a fingering of the interface, which in this case is controlled by the density, rather than viscosity, difference between the two fluids [7, 80, 81] (Fig. 4.1 (b)). One further option is to put the Hele-Shaw cell in rotation, after filling it with the two immiscible fluids making up the interface. A fingering instability of the interface is thus observed which is driven by centrifugal force [8] (Fig. 4.1 (c)).

Finger patterns can be induced in a quasi-two-dimensional electrolytic cell made of two thin electrodes sandwiched between transparent plates, with the space between them filled with an electrolytic solution. Upon biasing the electrodes, the deposited metallic ions at the cathode may develop a fingering instability when the cell is tilted by a small angle with respect to the horizontal [82]. Lopez-Salvans and coworkers [9] observed the formation of a finger pattern in a quasi-two-dimensional electrolytic cell ($110 \times 40 \times 0.1 \, \text{mm}^3$) containing a solution of $CuSO_4$ ($5 \times 10^{-2} \, M$) and Na_2SO_4 (from 10^{-3} to $10^{-2} \, M$). When the two electrodes are biased with a voltage between 10 and 30 V, well formed fingers are formed at the cathode (Fig 4.2).

A finger pattern arises in the situation where a thin elastic layer is bonded to a rigid support and its upper surface is put in contact with either a hemispherical glass lens [83], or a glass plate in the configuration of a cantilever beam [10] (Fig 4.3 (i)). Fingering instabilities develop in the crack between the film and the upper glass
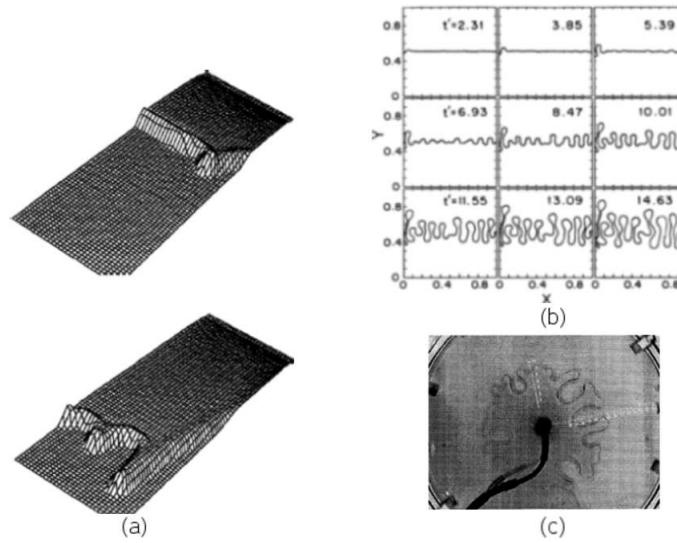
Figure 4.1:   Examples of fingering instabilities developed by a fluid interface. (a) Numerical solutions of the equation describing the flow of a viscous fluid down a vertical plane at two different times: the bottom image refers to the system configuration at a time step which is 7.5 times greater than that for the top image.   The initial configuration was chosen to be a mound of fluid with a parabolic cross section and occupying the top quarter of the computational plane. (From Ref. [6]). (b) Instability of an interface between isobutyric acid (top of each frame) and water (bottom) in a rectangular Hele-Shaw cell of dimensions $45 \times 45 \times 1$ mm^3. Dimensionless time t' is indicated for each frame. Positions x and y are expressed in units of cell width. (From [7]). (c) Typical pattern obtained in a rotating circular Hele-Shaw cell where the two fluids are silicon oil and air. The cell is made of two circular glass plates with a radius of 20 cm and a thickness of 6 mm. The separation between the two plates is between 0.25 and 1.0 mm. The angular velocity of cell rotation used to obtain the present pattern is 80 rpm. (From Ref. [8]).

cover due to the adhesion of the film to the glass. In the case of the cantilever beam configuration, the pattern aspect changes according to the glass cover rigidity and the film thickness (Fig 4.3 (ii)).

Finally, front fingering has been observed in combustion experiments [11]. A rectangular combustion cell with a narrow separation between the two plates has been used. A burning fuel such as filter or normal paper is introduced into one side of the cell. The opposite side of the cell is provided with a laminar flow of oxygen and the experiment is initiated by igniting the fuel along a line near a cell edge. As the flow velocity is reduced below a critical level, a fingering instability of the combustion front
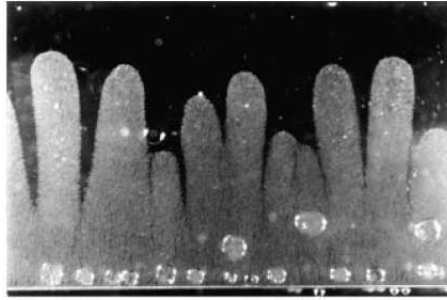
Figure 4.2: Fingering instability obtained by electro-chemical deposition using a quasi-two-dimensional electrolytic cell containing a non-binary solution. The exposed area corresponds to an electrode length of 16 mm. (From Ref. [9]).

sets in. This is caused by originally existing outward bumps in the interface which, due to their being closer to the oxygen source, tend to consume all available oxygen in their vicinity, thus screening and preventing the surrounding areas of the interface from growing. These bumps extend in size and length and, eventually, separate into fingers. The process just outlined becomes effective only in conditions of strong competition for oxygen, i.e. when the oxygen flow is reduced. This is when the front becomes unstable (Fig. 4.4).

The examples presented above are borrowed from various branches of physics and chemistry, and arise from profoundly different reasons. But despite the evident differences, all the systems mentioned above have something in common, in that they all display an initially straight boundary which advances due a driving force, e.g. a pressure gradient, gravity, a voltage gap, adhesion force, a temperature gradient, etc. When the driving force is uniformly distributed along the front, then the boundary advances also uniformly. But, if a bulge is formed along the front, e.g. as a result of statistical fluctuations, a positive feedback mechanism sets in whereby those areas with higher curvature pointing outward grow faster than the surrounding areas. In this way the instability feeds itself and propagates.
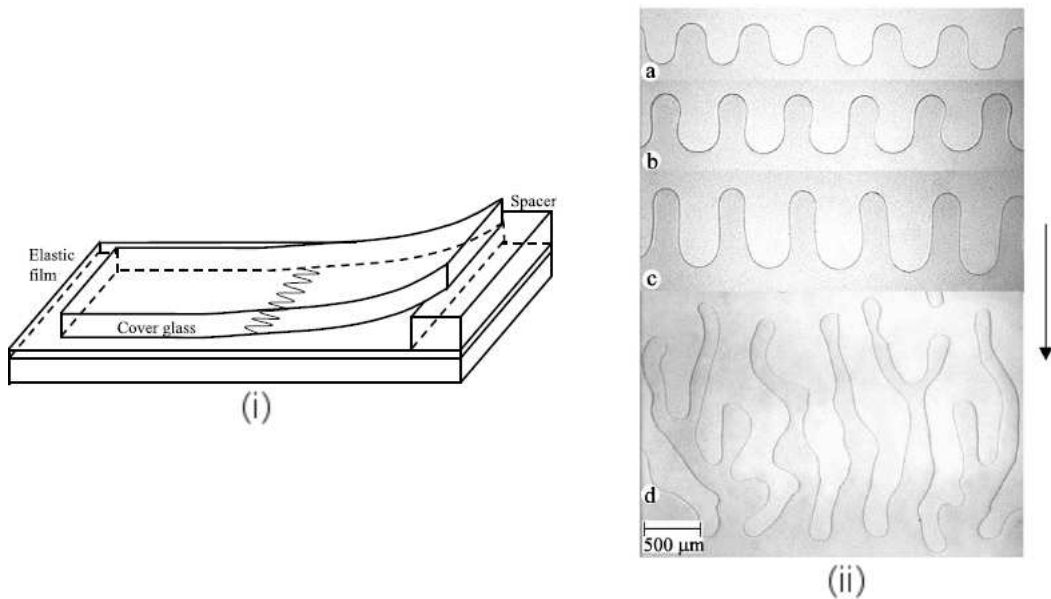
Figure 4.3: (i) Experimental set-up where a thin elastic film is bonded to a rigid support and contacted with a cover glass in the configuration of a cantilever beam. Fingering instability is developed in the crack between the glass and the film. (ii) Snapshots of the instability caused by the contact of an elastic film of thickness $150\,\mu$m against a glass beam of rigidity 0.02 (a), 0.09 (b), 0.2 (c), and 1.0 Nm (d). The arrow points in the direction in which the crack closes. (From Ref. [10]).

4.2.2 Fingering instability of a step edge

In the field of solid state physics, instabilities have been observed during MBE growth of semiconductors and metals. In the step-flow growth mode, a vicinal surface is used as a substrate where deposited atoms can diffuse across terraces and finally attach to preexisting steps. Nucleation on terraces is not allowed. This method is expected to advance the steps in a perpendicular direction, all at the same velocity, thus producing a layer-by-layer type of growth.

In fact, the meandering instability of a step during step flow growth has been predicted theoretically [84,85] and observed experimentally during epitaxial growth of semiconductors [86,87] and metals [88]. In their seminal paper Bales and Zangwill [84] (BZ) extended the analysis of crystal growth carried out by Burton, Cabrera and Frank [89] to take into account the so called Ehrlich-Schwoebel (ES) effect whereby an
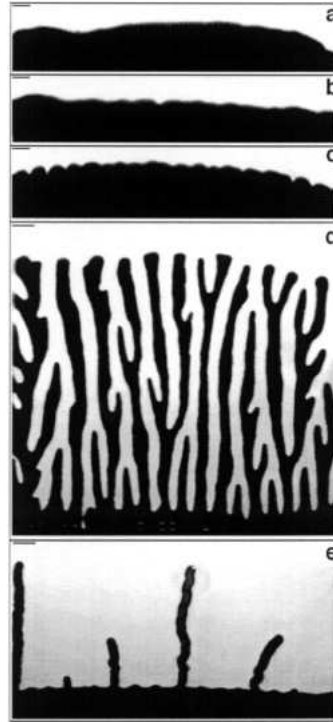
Figure 4.4: Fingering instability of a combustion front in a quasi-two-dimensional cell as a function of oxidising gas flow. The scale bars are 1 cm and the gap between plates is 0.5 cm. The oxygen flow is directed downwards and its values are 11.4 (a), 10.2 (b), 9.2 (c), 1.3 (d), and 0.1 cm/s (e). (From Ref. [11]).

adatom descending from a step edge to a lower lying terrace experiences an increased barrier with respect to the activation energy for diffusion on a terrace [90, 91]. This increase of activation energy is due to a decrease of coordination which the adatom undergoes in descending the step.

In the study carried out by BZ a system is considered where a gas atmosphere is in contact with a stepped surface. An adatom from the gas phase impinges on the substrate with a frequency F, migrates on the terrace according to a diffusion coefficient D, and desorbs with a lifetime τ. In the steady state regime, the concentration c of adatoms on the surface is expected to follow the following equation:

$$D \nabla^2 c - \frac{c}{\tau} + F = 0. \tag{4.1}$$

The problem is thus completely determined by imposing boundary conditions on the

considered domain - i.e. at infinity and along the step edge - and by specifying the requirements of mass conservation at the step. The boundary condition along the step edge is particularly interesting for the system studied in this thesis. An equilibrium adatom concentration c_{eq} is introduced, which is the uniform concentration of adatoms on the terrace in case of a straight step. By linearly expanding the chemical potential of the adatoms embedded in the upper terrace (*solid phase*) and of those facing the step and migrating on the lower terrace (*gas phase*), one finds that the concentration c of adatoms in gas phase in the area facing the step edge is given by:

$$c = c_{eq} + \frac{c_{eq}\Omega}{k_B T}\left(p_s - p_g\right); \tag{4.2}$$

where Ω is the volume occupied by an atom in the solid phase, k_B is the Boltzmann constant, T is the temperature, and p_s and p_g are the pressures of the adatoms in the solid and gas phase, respectively. At this point, Laplace's law can be used which states that when a surface (line) is curved, the pressure inside the curvature must be higher than outside, the difference being due to surface (line) tension effects [92, 93]. After defining a line tension γ along the step edge, Eq. (4.2) can be reformulated as:

$$c = c_{eq} + \frac{c_{eq}\Omega}{k_B T}\gamma\kappa; \tag{4.3}$$

where κ is the curvature of the step profile counted as positive for a convex profile.

An intuitive way to understand the effect of the curvature is by using a simple bond breaking model such as that presented in Fig. 4.5 for the case of a crystallographic plane with square symmetry. If the step profile is convex, the number of unsaturated bonds increases with respect to the case of a straight step, while for a concave profile the number of broken bonds is less than for a straight step. When atoms are deposited and adsorbed onto the lower terrace, there will therefore be an accumulation of gas phase adatoms in proximity to convex regions and depletion in areas surrounding concave regions, resulting in increased step roughness.
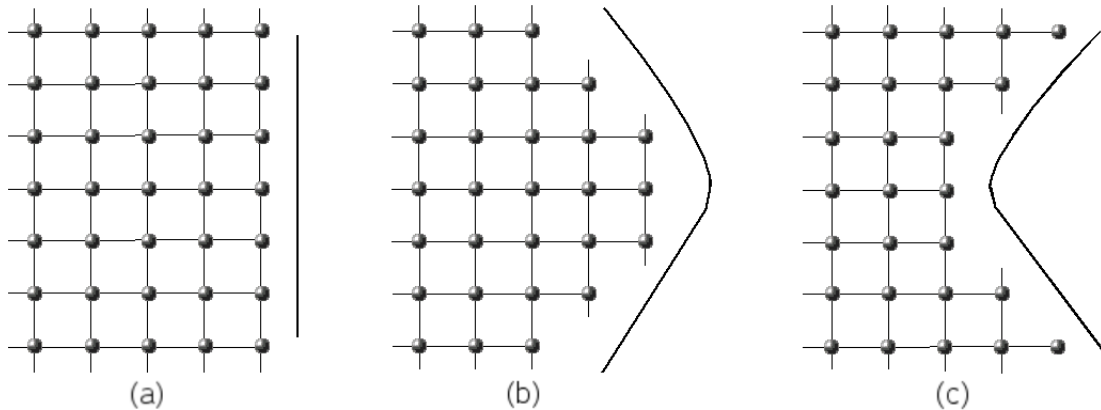
Figure 4.5:   Schematic view of the number of unsaturated bonds for a straight (a), a convex (b), and a concave step (c) on a surface with square symmetry. The grey spheres represent topmost atoms in the upper terrace; the thick black line indicates the step profile. The topmost atoms in the lower terrace are not indicated.

4.3   Au(111) surface

Au is an fcc type crystal and possesses three low-index crystallographic planes: the (100) plane with square unit cell, the (110) plane with a rectangular unit cell and, finally, the close packed (111) surface. The Au(111) surface is threefold degenerate, being invariant with respect to rotations of 120° around the [111] axis. Let us identify two orthogonal directions on the surface. We choose $\langle 1\bar{1}0 \rangle$ as the family of close-packing directions and $\langle 11\bar{2} \rangle$ as the set of directions orthogonal to $\langle 1\bar{1}0 \rangle$ (see Fig. 4.6).

On an fcc(111) surface, not all close packed step edges are equivalent. Steps which expose a {100} microfacet are called A type steps, whereas B steps are those ones which expose a {111} microfacet. A hexagonal island on a fcc(111) surface displays alternatively A and B type steps (see Fig. 4.7).

The Au(111) surface has been extensively studied over the last decade, from both an experimental and a theoretical point of view. The experimental techniques used encompass surface characterisation probes such as: low-energy electron diffraction (LEED), reflection high-energy electron diffraction (RHEED), transmission electron diffraction (TED), and STM. The theoretical investigations carried out so far are mostly based on
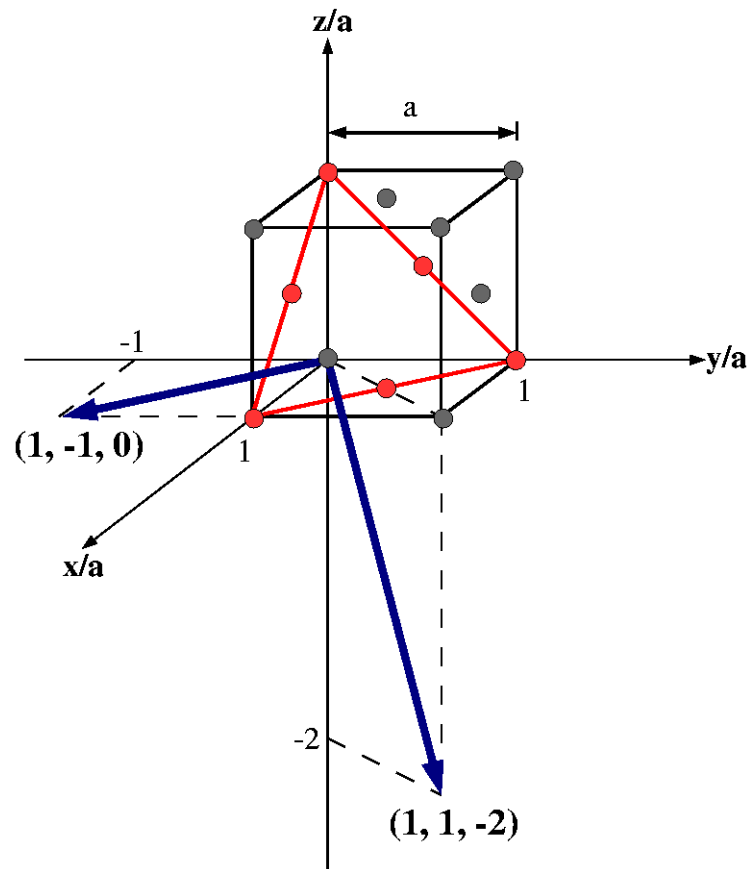
Figure 4.6: The conventional cubic unit cell of an fcc crystal is highlighted. The filled circles represent lattice sites. Red circles indicate atoms lying in the (111) plane, grey circles represents atoms outside the plane. The two vectors shown in blue are parallel to the reference directions chosen in the (111) plane: $[1\bar{1}0]$ for the close-packing direction and $[11\bar{2}]$ for the direction orthogonal to it.

semiempirical simulations, because the periodicity of the reconstructed surface is too large to allow a full first-principles calculation.

A helium diffraction experimental study [12] led to a model which is schematically depicted in Fig. 4.8 and was validated by subsequent atomically resolved STM images [13, 94]. According to this model, the structure of the reconstructed surface can be derived from the bulk terminated surface by the insertion of an extra row of atoms in the top monolayer along the $[11\bar{2}]$ direction for every 22 rows along the perpendicular $[1\bar{1}0]$ direction. A compression along the $[1\bar{1}0]$ direction is produced, whose effect is
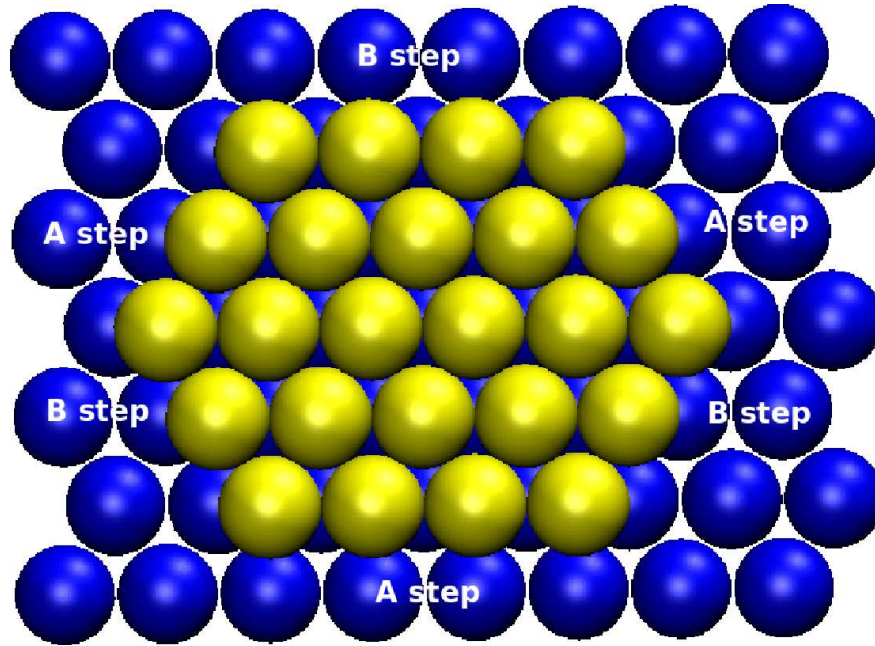
Figure 4.7: Sphere model of a monolayer island on a fcc(111) surface. Atoms in topmost layer are indicated in yellow, atoms in the lower lying layer are in blue. The two types of close packed step are indicated.

to reduce the lattice constant in that direction by an average value of 1/23 or about 4.3%. Because of the compression, the stacking along the close-packed direction varies periodically from fcc to hcp and back to fcc. It turns out that the compression is not uniform across the whole surface. In fact, within fcc- and hcp-like regions, surface atoms are almost in registry with the underlying lattice positions, but the transition between the two regions is occupied by a partial dislocation running along the $[11\bar{2}]$ direction. The atoms in the transition regions are raised up in the z direction by an amount dependent on their position along the $[1\bar{1}0]$ direction; furthermore they are more closely spaced than the atoms in the fcc- and hcp-like areas. These dislocations, called discommensuration lines, usually appear as brighter stripes in STM images (see Fig. 4.9). The overall reconstruction turns out to be a $(22 \pm 1) \times \sqrt{3}$ reconstruction, where in every unit cell 22 atoms are accommodated along the close-packed $[1\bar{1}0]$ direction and 2 atoms in the orthogonal $[11\bar{2}]$ direction.

Due to the three-fold symmetry of the Au(111) surface, three equivalent rotational
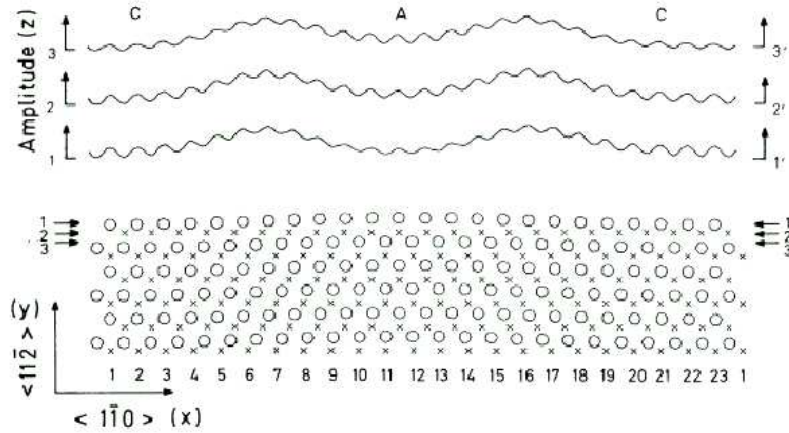
Figure 4.8: Top: hard-wall corrugation functions at three points in the unit cell (the vertical scale is exaggerated for clarity). C indicates areas where the stacking is fcc-like, whereas A is used to denote areas with an hcp-like stacking. Bottom: proposed structure. Crosses represent the second-layer and circles the surface-layer atoms (from Ref. [12]).

domains exist. In some cases a transition between two domains is observed on the reconstructed surface, which in STM images shows as a correlated bending of the dis-commensuration by 120° and −120°. This periodic sequence of domain boundaries results in a zig-zag pattern superimposed on the pattern caused by the $22 \times \sqrt{3}$ recon-struction and is called the *herringbone* reconstruction (see Fig. 4.10).

Although this model has been largely accepted from the experimental point of view, the situation is much less clear when the reconstruction is investigated with theoretical methods. Much of the theoretical work on the Au(111) surface relies on the *Frenkel-Kontorova* (FK) model. Originally developed for one-dimensional systems [95] and later extended to two-dimensional systems [96], this model describes situations where competition arises between a layer of topmost atoms which prefer to contract their inter-atomic bond distances with respect to the bulk atoms, and the potential due to the bulk which tends to keep the surface atoms in registry with it. The FK model, though, failed in predicting the reconstruction of several fcc (111) metal surfaces. In particular, in theoretical studies based on the FK model, the (111) surface of gold does
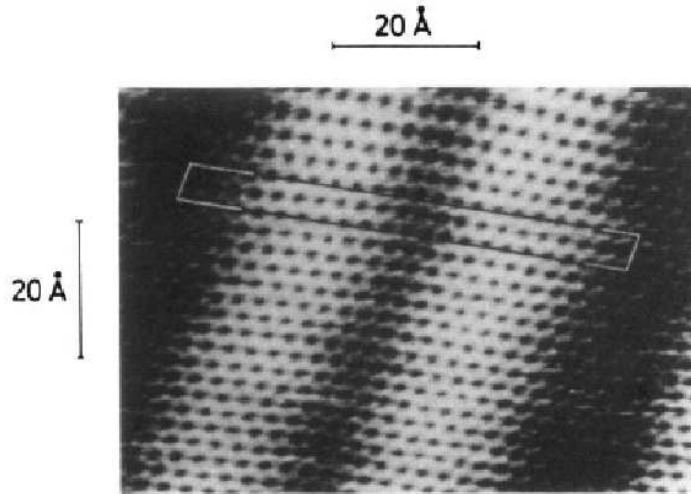
Figure 4.9:   Atomic resolution image obtained during an STM scan showing the $22 \times \sqrt{3}$ reconstruction of Au(111) ($I_t = 631$ nA; $V = 69$ mV). The unit cell of the reconstructed surface, marked in the figure, has dimension of approximately 64×4 Å^2. The measured atomic corrugation is 0.2 Å. (From Ref. [13]).

not appear as prone to reconstruct as is normally observed in experiments [97, 98].

A different approach has recently been attempted [99], where a thermodynamic model has been derived in order to determine the likeliness for a surface to reconstruct. Particular attention is devoted to the $22 \times \sqrt{3}$ reconstruction of the Au(111) surface. A version of the EAM model developed in a previous study [100] has been used to try to simulate the experimental reconstruction. Unfortunately, the input parameters to the EAM, when fitted to bulk properties of gold, did not stabilise the surface. Therefore, it was adjust one of the parameters in order to stabilise the $22 \times \sqrt{3}$ surface. After this was accomplished, simulated features of the reconstructed unit cell turned out to agree with the observations of previous experimental STM studies.

4.4   Growth of fingers on Au(111): the experiment

Recently Q. Guo, F. Yin and coworkers [14, 101, 102] performed a series of experiments in which a nanoscale pattern was induced on an originally straight step edge on Au(111) simply by repeatedly scanning with an STM the surface at room temperature and at
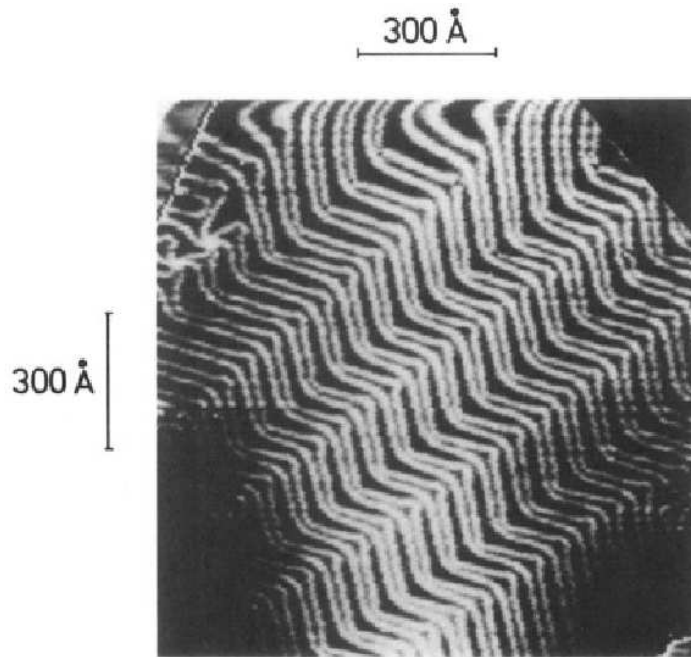
Figure 4.10: STM image of a Au(111) surface showing the herringbone reconstruction. (From Ref. [13]).

particularly high conditions of electric field. The scan parameters ordinarily used to image Au(111) are a tunnelling current between around 100 pA and 10 nA, and a bias voltage of around 1 V or lower. But when the tunnelling current is increased to a value between 30 and 50 nA and, at the same time, the voltage is between 2 and 3 V, then the step is observed to start meandering. The step rearranges giving rise to elongated structures resembling fingers. The fingers are one atomic layer high, have widths between 3 and 8 nm and they can reach lengths up to 200 nm (see Fig. 4.11).

The remarkable fact about these nanostructures is that they always grow aligned and, regardless of the scan direction, they grow along well determined crystallographic axes. The growth direction of the fingers turns out to correspond to one of the three equivalent close-packed directions of the (111) plane. This means that the fingers can either lie perpendicular to or form an angle of 150° with the direction [11$\bar{2}$] (or one of the two other directions equivalent to it), along which surface dislocations run (see Fig. 4.12). In order for the fingers to grow, there must be a component of the scan
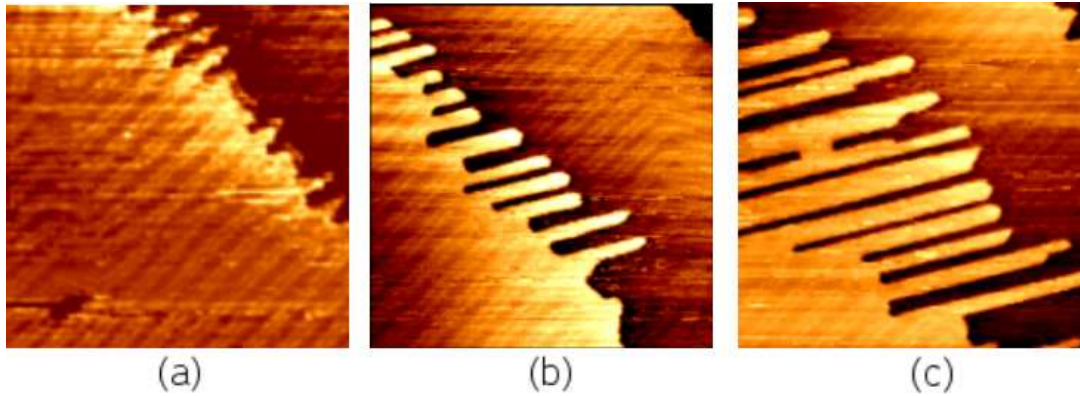
Figure 4.11: Series of $(103 \times 103)\,\mathrm{nm}^2$ STM images showing three different stages in the gold nanofinger growth (from Ref. [14]).

direction along one of the close-packed directions. It has been observed that the smaller the angle between the scan direction and the close-packed direction is, the faster the growth of the pattern [14].
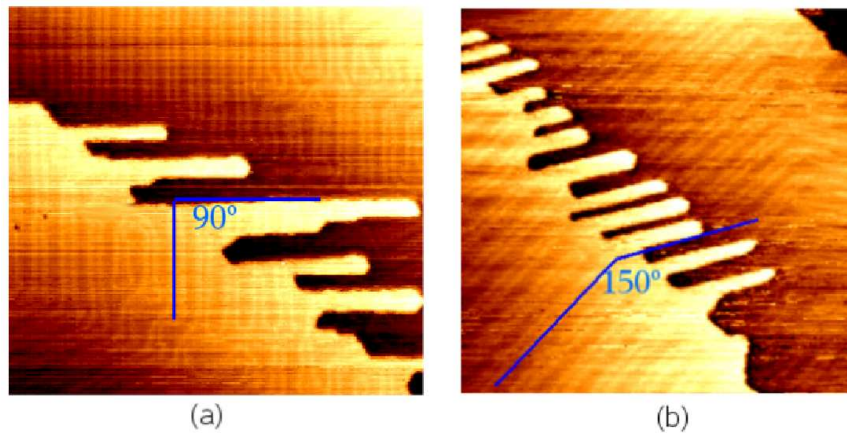
Figure 4.12: $\approx$ 100 nm $\times$ 100 nm and $\approx$ 150 nm $\times$ 150 nm images ((a) and (b), respectively) where the angle between the direction of gold nanofinger growth and the discommensuration lines is indicated. In both cases the fingers run along one of the three equivalent $\langle 1\bar{1}0 \rangle$ directions (from Ref. [14]).

The STM induced step self-reorganisation must be due to a rearrangement of atoms in the topmost surface layer. The experimental measurements [103] provide strong evidence to suggest that the mechanism underlying the finger growth is the detachment of atoms out of the upper terrace brought about by the intense electric field established

between the STM tip and the substrate.

Based on the experimental observations, it is possible to draw a picture of the phenomenon wherein some of the atoms, previously embedded in the upper terrace and in close proximity to the step edge, are detached from the step by the tip. This creates on the lower terrace a distribution of adatoms which can diffuse across the surface much more easily than before due to their decreased in-plane coordination. In their random walk across the plane, these freed adatoms may hit the step edge, where they are very likely to be captured.

Chapter 5

Surface diffusion and crystal growth

5.1   Introduction

Surface diffusion is a field of study of intense interest in solid state physics as particle mobility is the key for the understanding and control of dynamical processes occurring on surfaces. For instance, heterogeneous catalysis requires that the reactants adsorb onto and diffuse on the catalyst surface and in thin film epitaxial growth the deposited particles explore several sites before reaching the equilibrium state. Diffusion is also the natural mechanism for the formation of spontaneous and artificial nanostructures on surfaces. This is the aspect in which we are most interested and on which we shall focus throughout this chapter.

Sect. 5.2 introduces the basic concepts and equations of surface diffusion. Sect. 5.3 is a review of previous work on the diffusion of a single adatom on a bare surface, in particular metallic systems will be discussed. Subsequently, an overview of the existing literature regarding diffusion and nanostructure formation on metallic substrates will be provided in Sect. 5.4. Finally, Sect. 5.5 reports the methodology and results of the calculations of activation barriers to diffusion on the Au(111) surface.

5.2   General concepts

When an atom or a molecule is adsorbed on a surface, it is expected to feel the effect of the periodic potential $V_l(\mathbf{r})$ produced by the substrate. The adsorbate preferentially

occupies the sites of local equilibrium of the potential, which represent binding sites for the adsorbate. By exchanging thermal energy with the phonon bath of the substrate, the adsorbed particle is subject to local oscillations around the binding site. Statistically, the adsorbate can receive enough energy to hop across the potential energy barrier separating two neighbouring binding sites. The difference between the particle energy at the adsorption site and at the saddle point connecting two neighbouring minima is the classical activation barrier, E_d, for the diffusion process. After the jump, the particle loses memory of the process which has just occurred if the amount of energy yielded by the particle to the thermal bath is enough to allow the particle to spend a longer time in the new binding site than the typical time of thermal vibrations. When this condition is fulfilled, the particle motion on the surface is fully stochastic, consisting of a random walk in two dimensions.

As is the case with all thermally activated processes [104], the rate of diffusion ν is expected to be the product of a prefactor expressing the attempt frequency and an Arrhenius exponential factor giving the temperature dependence. Therefore we can express the diffusion rate ν as [105]:

$$\nu = \nu_0 \exp\left[\frac{-E_d}{k_B T}\right]; \tag{5.1}$$

where ν_0 is known as the *attempt frequency* and k_B is the Boltzmann constant. Several attempts have been made to derive (5.1) from physical properties of the system - i.e. the substrate plus adsorbate. One of the most popular approaches is *transition state theory* [106] (TST), which assumes that the system is in equilibrium both when the adsorbate is in the binding site and in the transition state at the saddle point. The diffusion rate can then be expressed as the ratio of the partition functions of the system in the two states. A harmonic approximation leads to the expression of ν_0 as a function of the normal mode frequencies of the adsorbate both in the equilibrium and the transition state.

We now define the *surface tracer diffusion coefficient D_T* as:

$$\langle (\Delta \mathbf{r(t)})^2 \rangle = 4 D_T t. \tag{5.2}$$

From elementary considerations [107–109], one obtains that the mean square displacement $\langle |\mathbf{r(t)} - \mathbf{r(0)}|^2 \rangle$ of a particle performing a random walk in two dimension with a hopping rate ν is:

$$\langle (\Delta \mathbf{r(t)})^2 \rangle = \langle |\mathbf{r(t)} - \mathbf{r(0)}|^2 \rangle = a^2 \nu t; \tag{5.3}$$

where $\mathbf{r(t)}$ and $\mathbf{r(0)}$ are the particle position at time t and time 0, respectively, and a is the jump length. If the diffusing particle can only hop between neighbouring adsorption sites on the surface, then a is the periodicity of the surface lattice.

By comparing (5.3) and (5.2), a relationship between the tracer diffusion coefficient and the hopping rate can be found:

$$D_T = \frac{1}{4} a^2 \nu. \tag{5.4}$$

Or, by using (5.1):

$$D_T = D_0 \exp\left[\frac{-E_d}{k_B T} \right]; \tag{5.5}$$

where:

$$D_0 = \frac{1}{4} a^2 \nu_0. \tag{5.6}$$

This model is expected to be valid as long as the diffusing particle loses enough energy after each hop so that the system is thermalised between two jumps. This certainly happens if thermal energies are much lower than the activation energy for diffusion (i.e. $k_B T \ll E_d$). The description provided by TST starts breaking down for $k_B T \sim E_d$, when the adsorbed particle may perform longer jumps than simply hopping to nearest neighbouring adsorption sites. Long jumps increase the mobility of the adsorbed particle, thus transforming the constant of proportionality a in (5.6) from the surface lattice constant into the mean square jump length $\langle l^2 \rangle$ [110]. Finally, when $k_B T \gg E_d$, Brownian motion is expected for the diffusion of a single adatom on the surface [111].

The tracer diffusion describes the motion of a single particle adsorbed on a surface and is neither quantitatively nor conceptually the same as the *collective diffusion coefficient* D_c entering Fick's diffusion equation:

$$\frac{\partial n}{\partial t} = D_c \nabla^2 n, \tag{5.7}$$

which describes the evolution of a group of adsorbed particles of density $n(\mathbf{r}, t)$. For high surface covergages, the interactions between adsorbates become important and the diffusing particles cannot be treated as independent. However, in the limit of low coverages, the two diffusion coefficients tend to coincide in value.

In the following, the discussion will be restricted to the diffusion of metal adsorbates on metal surfaces. We shall focus our attention in particular on noble and transition metals. The reader who wants to know more about different aspects of diffusion is referred to one of the many comprehensive reviews available in the literature [15, 105, 111–115].

5.3   Single adatom diffusion on flat metal surfaces

The experimental study of surface diffusion experienced dramatic progress following the invention of the field ion microscope (FIM) [90], which allows the observation of adsorbate motion in real time [112, 113]. Single adatom displacement on the FIM tip can be followed and registered. An atom is initially deposited on a sharp metal tip, which makes FIM the most reliable and accurate experimental technique for diffusion coefficient determination. The tip is heated to allow the adsorbate to diffuse for a certain time interval, after which the tip is cooled down to a lower temperature. An image of the system in this *frozen* state is then taken by applying an intense electric field between the tip and an electrode acting as the screen. The mean square displacement of the atom on the tip is obtained after repeated heating and imaging cycles. By means of (5.2), the tracer diffusion coefficient D_T is then easily worked out. After repeating

the measurements over a large enough range of temperatures, the value of both the prefactor D_0 and of the activation energy E_D can be extracted by means of (5.5).

FIM was employed, for instance, to provide experimental evidence of an alternative diffusion mechanism to hopping. On the Ir(110) surface, the adatom cross-channel diffusion was proved to occur by atom exchange [116], in which the diffusing adatom kicks out and replaces a lattice atom on the side of the channel, as is depicted schematically in Fig. 5.1. The displaced atom then continues the diffusion process. FIM also allowed the observation of atom exchange mechanisms in self-diffusion on (100) surfaces of such fcc metals as Ir [117] and Pt [118] (see Fig. 5.2). To date, atom exchange diffusion has never been observed experimentally on any flat fcc(111) surfaces.
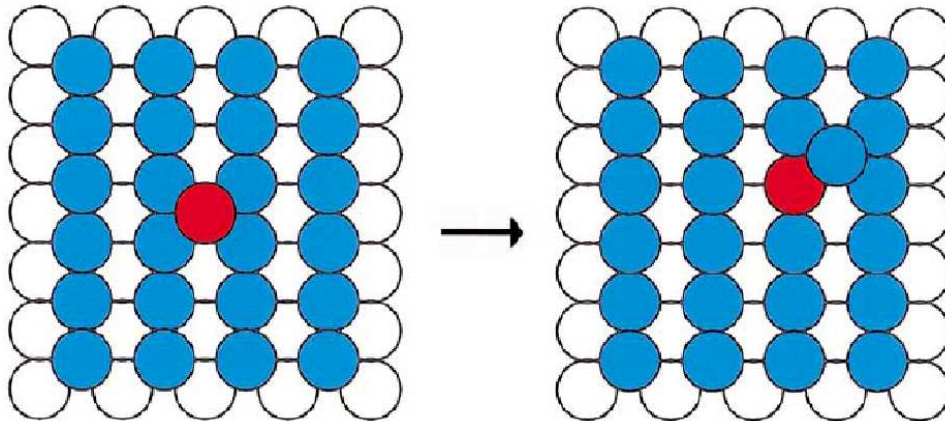
Figure 5.1: Mechanism of diffusion by atom exchange on a fcc(110) surface. The diffusing adatom (red) kicks out an atom in the substrate (blue), and takes its place; the latter emerges in a neighbouring channel and continues the diffusion process (from Ref. [15]).

The inherent limitation of the FIM lies in its extremely narrow range of applicability. The metal acting as the substrate must be easy to process and to shape into a sharp tip while at the same time displaying high resistance to intense electric fields. The use of the FIM is therefore limited to a few noble and transition metals. These limitations have been overcome by Scanning Tunneling Microscopy (STM). Direct observations of adatom motion by STM, though still possible [119], are technically more demanding
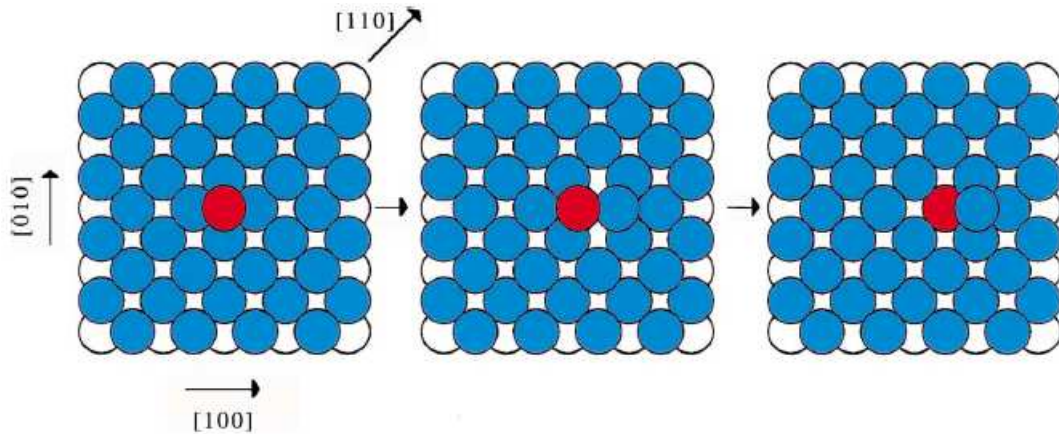
Figure 5.2: Mechanism of diffusion by atom exchange on a fcc(100) surface. The diffusing adatom (red) kicks out an atom from the top layer of the substrate (blue), and takes its place; the latter emerges in a next nearest neighbour site and continues the diffusion process (from Ref. [15]).

than with FIM. In the case of STM, the heating and imaging cycles are much slower than with FIM, because heating a field emitter of small mass is much easier than heating a large STM sample. This increases the possibility of having the sample affected by contaminant adsorbates. Furthermore, as the sample stage is normally subject to thermal drift, it might not be easy to retrieve the same area of a typical STM sample after heating. Therefore, the diffusion coefficient has to be deduced indirectly by fitting the experimental data to some model predicted by theory. One of the most popular among these indirect methods uses *classical nucleation theory* [120, 121], and was first used for the study of Si diffusion on Si(100) [122]. Nucleation theory establishes a relationship between the number of islands formed during an epitaxial growth experiment and the surface diffusion coefficient. The assumption underlying the theory is that, for a given deposition rate, the faster the diffusion across the surface, the higher the chances are for an adatom to come across and be trapped by an already existing island before bumping into another isolated adatom, thus giving rise to a new island. The density of nucleated islands is therefore expected to be lower than under conditions of hindered diffusion.

Due to the difficulty in carrying out experimental investigations, theoretical approaches have been extensively used to study diffusion on surfaces. Where possible, full *ab-initio* methods such as Density Functional Theory (DFT) have been used to calculate static properties of adsorbates on surfaces. Semiempirical potentials of the type of derived from DFT such as the Embedded Atom Method (EAM) [36, 100] or Effective Medium Theory (EMT) [39] have been extensively used for the study of physical properties of metals. Also many-body potentials obtained from the second moment approximation to the Tight Binding Theory such as the Gupta or RGL potential, have been used to describe interatomic interactions in a variety of metals. All these potentials can easily be incorporated into an algorithm reproducing the system dynamics, which is typically provided by classical Molecular Dynamics (MD). Table 5.1 lists the values of diffusion activation barriers (E_d), prefactors for diffusion (D_0) and hopping attempt frequencies (ν_0) for some of the investigated systems.Results obtained with different experimental and theoretical techniques are compared.

System	E_d (eV)	D_0 (cm^2/s)	ν_0 (s^{-1})	Method	Ref.
Rh/Rh(111)	0.16 ± 0.02	2×10^{-4}	10^{12}	FIM	[123]
Rh/Rh(100)	0.88 ± 0.07	10^{-3}	3×10^{12}	FIM	[123]
Ir/Ir(111)	0.27 ± 0.04	$10^{-4 \pm 0.15}$	$5 \times 10^{11 \pm 0.15}$	FIM	[124]
	0.22 ± 0.03	$8.8 \times 10^{-3 \pm 0.9}$	$4 \times 10^{13 \pm 0.9}$	FIM	[125]
	0.24 ± 0.03			DFT	[126]
Ir/Ir(100)	0.84 ± 0.05	$6.3 \times 10^{-2 \pm 1}$	$2 \times 10^{14 \pm 1}$	FIM	[117]
	1.39 ± 0.04			DFT	[126]
Ir/Ir(110) ($\parallel$)	0.80 ± 0.04	$4 \times 10^{-3 \pm 0.8}$	$2 \times 10^{13 \pm 0.8}$	FIM	[127]
Ir/Ir(110) ($\perp$)	0.71 ± 0.02	$6 \times 10^{-2 \pm 1.8}$	$2 \times 10^{14 \pm 1.8}$	FIM	[127]
Pt/Pt(111)	0.24 ± 0.02			FIM	[128]
	0.260 ± 0.003	2.0×10^{-3}	10^{13}	FIM	[129]
	0.26 ± 0.01	$10^{-3 \pm 0.5}$	$5 \times 10^{12 \pm 0.5}$	STM	[130]
	0.38			DFT	[128]
	< 0.080			EAM	[128]
	$0.159, 0.048$			EMT	[131, 132]
Pt/Pt(100)	0.47 ± 0.01	1.3×10^{-3}	3×10^{12}	FIM	[133]
Pt/Pt(110) ($\parallel$)	0.72 ± 0.07	3×10^{-4}	8×10^{11}	FIM	[112]
Pt/Pt(110) ($\perp$)	0.69 ± 0.07	6×10^{-4}	2×10^{12}	FIM	[112]
Ag/Ag(111)	0.097 ± 0.010	$1.9 \times 10^{-3 \pm 0.4}$	$10^{13 \pm 0.4}$	STM	[19]
	0.14 ± 0.02			DFT	[126]
	0.081			DFT	[18]
	0.055	1.5×10^{-4}	1.5×10^{12}	EAM	[134]
	$0.064, 0.020$			EMT	[131, 132]
Ag/Ag(100)	0.50 ± 0.03			DFT	[126]
	$0.52, 0.45$			DFT	[135]
	0.48	3.1×-3	1.5×10^{13}	EAM	[134]
	0.365			EMT	[132]
Au/Au(111)	0.22 ± 0.03			DFT	[126]
	0.015	7×10^{-5}	1.1×10^{12}	EAM	[134]
	0.12	3.4×10^{-4}	1.6×10^{12}	RGL	[16]
	$0.029, 0.102$			EMT	[131, 132]
Au/Au(100)	0.62 ± 0.04			DFT	[126]
	0.26	5.8×10^{-3}	1.4×10^{13}	EAM	[134]
	0.49			EMT	[132]
Al/Al(111)	0.042 ± 0.004	$2 \times 10^{-9 \pm 0.25}$	$8 \times 10^{6 \pm 0.25}$	STM	[136]
	0.04			DFT	[137]
	$0.054, 0.074$	10^{-3}	5×10^{12}	EAM	[138]
Al/Al(100)	0.35			DFT	[139]
	$0.69, 0.25$	4×10^{-2}	2×10^{13}	EAM	[138]
Al/Al(110) ($\parallel$)	0.33			DFT	[139]
	0.26			EAM	[138]
Al/Al(110) ($\perp$)	0.62			DFT	[139]
	< 0.30	5×10^{-2}	3×10^{13}	EAM	[138]

Table 5.1:   Activation energies (E_d), prefactors (D_0) and hopping attempt rates (ν_0) as found by means of different experimental and theoretical methods.

Some points are worth mentioning. Comparing self-diffusion on different crystallographic planes of the same fcc metal, both experimental data and calculations show that diffusion is always faster on the (111) than on the (100) plane. The reason for

this is that the denser packing of the (111) surface causes the adatom to be bound less strongly to the surface. The surface potential the adatom experiences is thus less corrugated than in more open lattice planes. For (110) surfaces, the situation is complicated by the high anisotropy of the structure. There are two migration paths for an adatom on a (110) plane. *In-channel* diffusion occurs in the $\langle 1\bar{1}0 \rangle$ direction parallel to the channel formed by two neighbouring rows of close packed atoms; on the other hand, *cross-channel* diffusion occurs in the $\langle 100 \rangle$ perpendicular to the channel. The activation barriers for these two processes can be profoundly different for the same material and often they proceed through different mechanisms. For instance, on both Pt(110) and Ir(110) cross-channel diffusion occurs through atom exchange, whereas in-channel diffusion occurs by means of normal hopping.

Table 5.1 also shows that semiempirical many-body potentials tend to underestimate activation barriers as compared to both experimental data and ab-initio calculations. Semiempirical methods have long been known to be reliable in predicting general behaviour or trends for materials, but one cannot expect a high quantitative accuracy when calculating physical properties.

Despite the relatively large range of activation energies (E_d) for the system listed in Table 5.1, hopping attempt frequencies ν_0 do not seem to vary appreciably, most of them falling in the range $10^{12} - 10^{13}$ s^{-1}. In fact, this is the order of magnitude for the attempt frequency for rate processes at surfaces predicted by classical TST in the approximation of harmonic crystals. The value of the prefactor for Al/Al(111) derived by Barth et al. [136] using nucleation theory seems to deviate from this range dramatically and semiempirical calculations showed that there seems to be a correlation between barrier height and prefactor [134, 140, 141]: when the activation energy increases, the prefactor also increases so as to compensate for the increased difficulty in overcoming the barrier. This empirical law, called the Meyer-Neldel or compensation rule, is far from universal. Experimental evidence is not stringent enough to prove it and numer-

ous counterexamples can be found in the literature. For example, Wang et al. [142] have studied by FIM the diffusion of several different metals on the W(211) surface, finding in all cases the expected value of 10^{12} s^{-1} for the prefactor, despite the widely different activation energies measured.

In the case of self-diffusion on Au(111), the normal expected attempt frequency of 10^{12} s^{-1} is found in two different semiempirical studies [16, 134]. The two studies also agree regarding the diffusion mechanism, which is identified as simple hopping, rather than exchange, at least up to 750 K. Ferrando and Treglia [16] point out that diffusion on Au(111) can be well described by a random walk model for a wide range of temperatures. At 500 K the adatom still spends most of the time in the three-fold hollow sites on the surface, as shown in Fig. 5.3. The study of the dependence of the diffusion coefficient D on temperature, reveals that the dependence is Arrhenius-type at all temperatures in the range investigated (see Fig. 5.4). A comparison, between the activation energies extracted from the plot of D versus temperature and those obtained from a full system relaxation at 0 K, shows that the values are in perfect agreement. A result which is found also in Ref. [134]. Therefore, the activation energy to diffusion can be worked out from static calculations simply by taking the difference in energy of the system in the equilibrium and the transition state.

Both of the studies discussed above were performed on the ideal Au(111) surface, with no regard to the $22 \times \sqrt{3}$ reconstruction. The presence of a uniaxial compressive strain on the surface, though, is expected to affect adatom diffusion on the reconstructed surface. EAM calculations, where diffusion on the bulk-like and reconstructed diffusion were compared, have confirmed this hypothesis [17]. Diffusion on the reconstructed surface was found to be significantly slower than on the ideal Au(111) surface, as shown in Fig. 5.5. Diffusion coefficients were calculated to differ by a factor of 1.3 at room temperature and by up to an order of magnitude at the lowest examined temperature of 75 K [17]. Furthermore, diffusion becomes anisotropic on the reconstructed
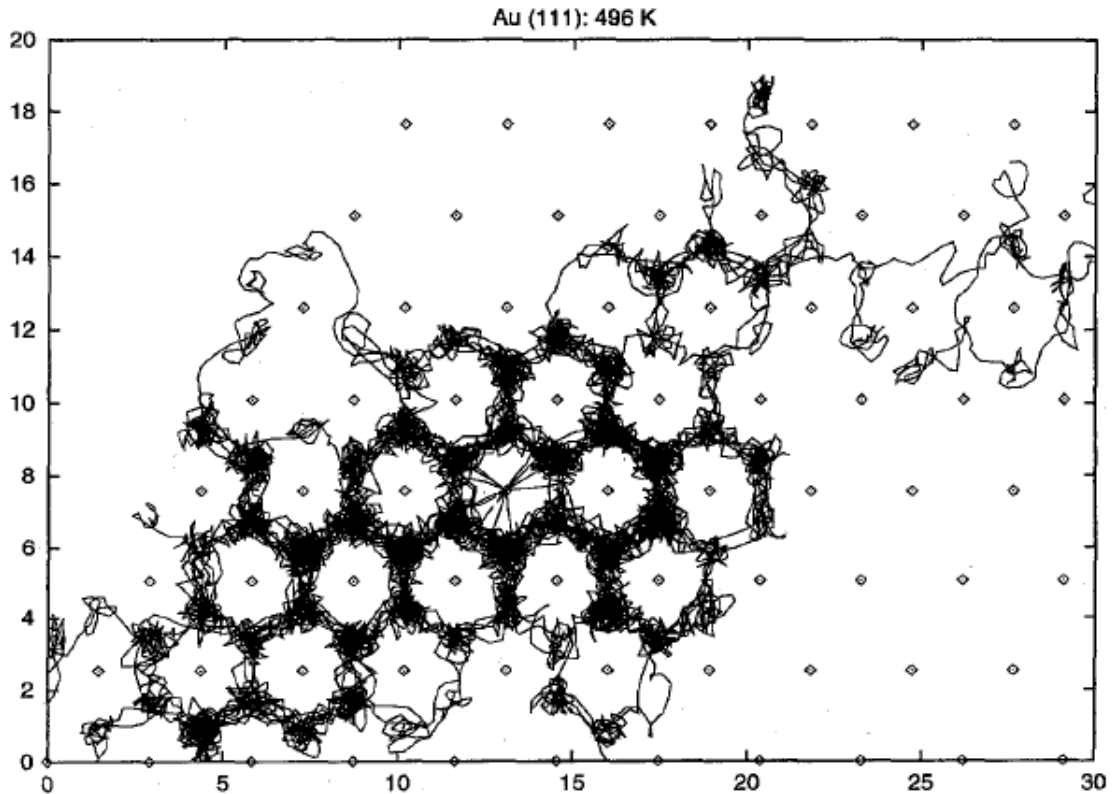
Figure 5.3: Trajectory of a Au adatom diffusion on Au(111) as obtained in a series of MD calculations with the RGL potential. All calculations were carried out at 496 K for a time interval of 180 ps. The adatoms starts from the same position with different initial conditions (from Ref. [16]).

surface, where preferential diffusion channels arise perpendicular to the strain direction. Activation barriers for diffusion along and across the channel were found to be in the ratio of 2.1 to 1. The semi-empirical study performed by Liu et al. [143] leads to similar conclusions. In this work, self-diffusion on Au(111) was studied in the presence of the $22 \times \sqrt{3}$ reconstruction. Anisotropic local strain was found to affect the adatom binding energy to equilibrium sites as well as the activation energies for diffusion. As a result of the reconstruction induced strain, the barriers for diffusion were found to be different, according to both the adatom position on the surface and the diffusion direction. Activation energies were calculated to range from ≈ 0.12 to ≈ 0.75 eV and to differ by up to ≈ 0.40 eV for diffusion in different directions from the same equilibrium site. The strain causes the creation of preferential diffusion channels on the
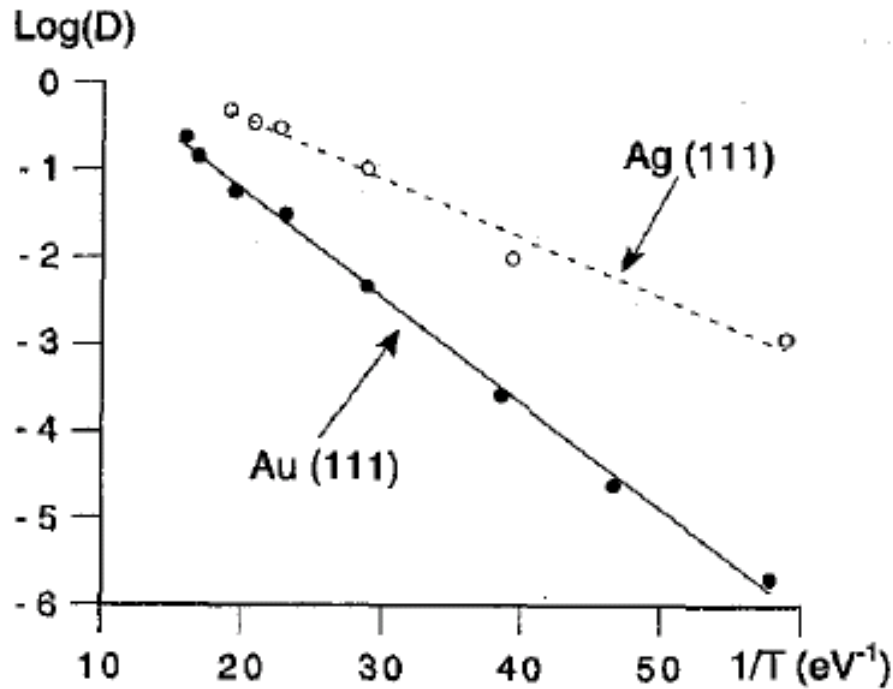
Figure 5.4: Arrhenius plot of the diffusion coefficient for self-diffusion on Au(111) and Ag(111) (from Ref. [16]).

reconstructed surface. Since diffusion is faster in the transition regions than in fcc-like or hcp-like stacking regions, adatoms are expected to segregate in the former areas and to diffuse preferentially along the open direction parallel to the discommensuration lines.

Apart from Au, Pt is the only other fcc metal whose (111) crystallographic plane has been found to display a reconstruction similar, though not identical, to the herringbone reconstruction of Au(111). Above $\approx$ 1330 K, Pt(111) has been observed to reconstruct spontaneously [144], but the reconstruction can also be induced down to 400 K by exposing the surface to a supersaturated Pt gas [145]. From the theoretical point of view, EMT calculations tried to study the phenomenon of the reconstruction and the question of the adatom mobility on the reconstructed surface [146]. For the displacement in the direction perpendicular to the discommensuration lines, it was observed that, on approaching the discommensuration lines, the activation energy for adatom
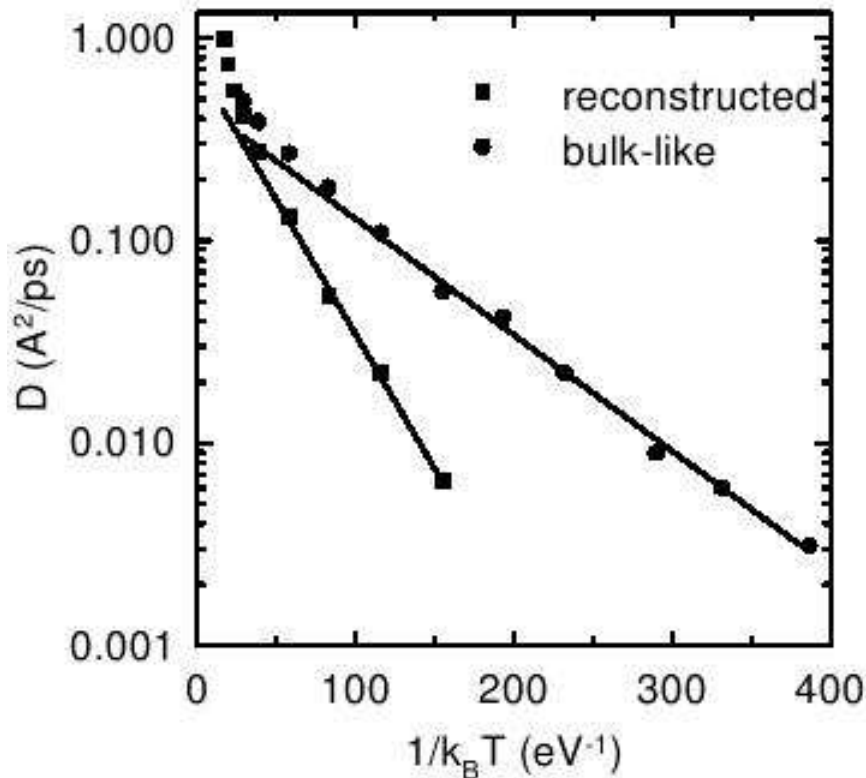
Figure 5.5: Arrhenius plots of the diffusion coefficients for the reconstructed and bulk-like Au(111) surface. Diffusion coefficients are extracted from MD simulations at constant temperature with the EAM potential. The straight lines indicate low-T fits to data (from Ref. [17]).

diffusion increased from 0.18 eV (the value calculated for the flat surface) to about 0.28 eV. Furthermore, the binding energy of the Pt adatom was found to decrease on approaching partial dislocations. This study is far from conclusive, in that the question of a possible anisotropy of diffusion, which could cause a preferential diffusion direction on the reconstructed surface, was not considered at all.

Finally, altered adatom diffusion due to strained substrates can be found in systems grown by means of heteroepitaxy. For example, on depositing Ag on a Pt(111) substrate, Brune and coworkers [19] found a high dependence of the Ag adatom mobility on the number of Ag layers previously deposited. In particular, it was demonstrated that diffusion of an Ag adatom on one monolayer of Ag deposited on Pt(111) is faster

than self-diffusion on Pt(111). The decrease of the diffusion barrier is due to the 4.2% isotropic compressive strain that an Ag monolayer grown on a Pt(111) surface experiences. This assumption was proved and generalised by an EMT calculation of diffusion barrier for an Ag adatom in presence of a strained Ag(111) substrate. The calculations show that compressive strain causes a decrease of activation barrier to diffusion, whereas tensile strain an increase [19]. This conclusion has been confirmed by first-principles calculations on the same system, where a linear dependence of the activation energy for self-diffusion on the strain was found [18], as shown in Fig. 5.6. But this does not seem to be the whole story, because strain affects surface diffusion differently, depending on whether it is isotropic or anisotropic. For example, the second monolayer of Ag deposited on Pt(111) relaxes via the formation of periodic arrays of dislocations, thus giving rise to an anisotropic inhomogeneous strain on the topmost surface. When Ag diffusion is studied on this surface, it is found that dislocations act as repulsive barriers for adatoms, which tend to segregate in pseudomorphic areas [19]. This is not always the case, for instance dislocations can act as attractive sinks for diffusing adatoms, as in Ni and Fe diffusion on Au(111) (see below). The influence of dislocations on diffusion is, therefore, a subtle and, as yet, not completely clear topic.

5.4 Growth of nanostructures on metal substrates

Nanostructure formation on surfaces is a process of crucial importance, both from a fundamental and a technological point of view [120, 147]. This field of study has received ever increasing attention in the last few decades, since the electronic industry has displayed a tendency towards the progressive reduction of device characteristic dimensions. Structures on surfaces can be arranged by direct manipulation of atoms or molecules adsorbed on the substrate by means of an STM [148, 149] tip. Alternatively, one can exploit the surface properties and allow the adsorbate to self-organise into patterns. The latter phenomenon is observed during homoepitaxial or heteroepitaxial
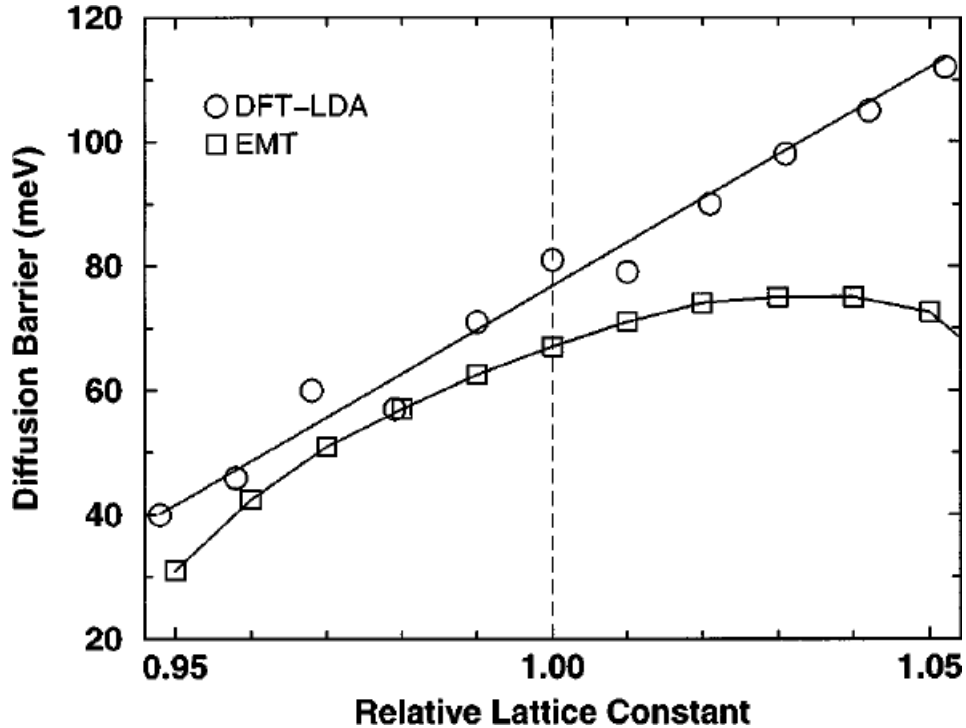
Figure 5.6: Diffusion barrier for Ag on Ag(111) as a function of the relative lattice constant. The values of the lattice constant are normalised with respect to the calculated bulk lattice constant of Ag (4.05 Å for DFT and 4.075 Å for EMT). The DFT calculations performed in Ref. [18] are compared with semiempirical EMT calculations carried out in Ref. [19] (from Ref. [18]).

growth of metals and semiconductors. The particles, previously in the vapour phase, are deposited onto the substrate where they diffuse until they hit another adsorbed particle. This process causes the formation of clusters on the substrate, which can either be two-dimensional (islands), or three-dimensional (mounds). These structures usually assume a wide range of shapes, depending on the surface characteristics.

In order to be able to control the formation of nanostructures on metal surfaces, it is essential to understand the atomistic mechanisms which underlie the growth phenomena [150, 151]. The understanding of self-organised growth on surfaces, in particular, requires a careful study of adatom diffusion in the presence of step edges, besides migration on the open surface. Therefore, epitaxial growth and diffusion in the presence of surface defects are so strongly related that it is not possible to treat them separately.

In what follows, we shall give an overview of the research carried out to date to explain phenomena observed in epitaxial growth in terms of atomistic processes. We shall restrict the discussion to two dimensional structures, or islands, which form during thin film metal growth.

It is important to point out that thin film growth is inherently a non-equilibrium process. Under conditions of thermodynamic equilibrium, in fact, all atomic processes proceed at equal rates in both the forward and reverse direction. Therefore, at equilibrium, as many particles are adsorbed on the surface as desorb per unit of time; thus giving a null net growth rate. In order to have net growth, the system has to be brought out of thermodynamic equilibrium. This is the reason why self-organised growth on surfaces obeys kinetic, rather than, thermodynamic rules and why the study of microscopic events underlying self-organised growth is so important.

One of the most studied systems is Pt(111), where a spectacular series of island morphologies have been obtained during deposition at submonolayer coverages at different temperatures [20]. After deposition at 200 K, branched fractal-like islands called dendrites are formed (Fig. 5.7 a). At 400 K, adatoms aggregate in compact triangular islands bounded by A-type steps (Fig. 5.7 b). Upon increasing the temperature to 455 K, hexagonal islands are formed (Fig. 5.7 c), and at 640 K triangles are again found, but this time the edges are oriented along B-type steps (Fig. 5.7 d). Finally, at 710 K, islands assume the form of distorted hexagons with B-type steps forming longer sides than A-type (Fig. 5.7 e_1). This is the equilibrium as it has been demonstrated that it does not depend on the system history [20].

One of the most surprising points in this experiment is the inversion of the triangular shape displayed by the islands when varying the substrate temperature. This was explained in the original work [20] and in a later theoretical investigation by the same group [152], as a difference of step advancement for the A- and B-edges. It is assumed that the island boundary which advances faster will disappear as growth proceeds.

The reason for this difference in growth speed was traced to an anisotropy in adatom migration along the two types of close-packed step edges. The suggested scenario is that the edge where the speed of migration is lower will grow faster because the presence of step adatom is higher and, thus, the probability of nucleation of a new step edge line is greater. If one could prove the different temperature dependence of the diffusion coefficients on the two types of step, then this postulated reason for the inversion of the triangular shape would be proved.
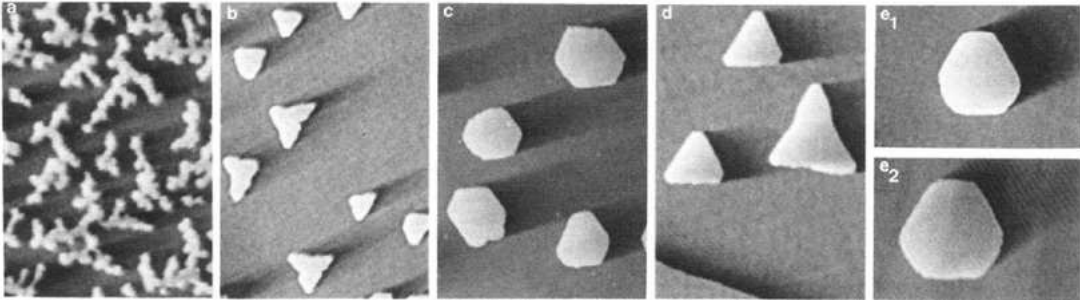
Figure 5.7: Islands grown on Pt(111) upon deposition of a fraction θ of a monolayer (ML) of Pt at a substrate temperature of T_S. In all cases the typical deposition rate is 10^{-2} ML/s. (a) $T_S = 200$ K, $\theta = 0.2$ ML, image size 280 Å × 400 Å; (b) $T_S = 400$ K, $\theta = 0.08$ ML, image size 1300 Å × 1900 Å; (c) $T_S = 455$ K, $\theta = 0.14$ ML, image size 770 Å × 1100 Å; (d) $T_S = 640$ K, $\theta = 0.15$ ML, image size 2300 Å × 3300 Å; (e$_1$) $T_S = 710$ K, $\theta = 0.08$ ML, image size 1540 Å × 1100 Å; (e$_2$) deposition at 425 K, followed by annealing at 710 K for 1 min, image size 630 Å × 900 Å (from Ref. [20]).

This explanation, however, was proven not to be satisfactory in a later work by Jacobsen and coworkers [153] where KMC simulations on a lattice model demonstrated that, if only anisotropy in step edge diffusion is assumed, then the step with the fast edge diffusion disappears, as opposed to the thesis supported by Michely and coworkers [20]. Rather, the asymmetry in corner diffusion is found to have a much stronger effect. In the same study [153], the transition from dendritic to compact island shapes is investigated. The transition occurs when edge diffusion and corner crossing are sufficiently fast for the adatoms to diffuse back and forth between two adjacent step edges.

The puzzle of the inversion of the triangular shapes of islands grown on Pt(111) be-

came clearer when the same group published the results of an experiment [154], where epitaxial growth on Pt(111) was studied with and without the presence of CO contaminants. The experiment shows that the switch from the triangular shape bounded by A-steps to that bounded by B-steps is not a temperature effect, but, rather, it is mediated by CO. In absence of contaminant particles, triangular shaped islands bounded by B-steps are also observed at the lower temperature of 400 K.

Using these findings, Ovesson and coworkers [155] developed a lattice model of the surface to account for the formation of compact triangular islands on fcc(111) surfaces. KMC was again used, with a set of barriers previously calculated by ab-initio methods [156], for homoepitaxy on Al(111). One of the conclusions drawn from the study was that edge diffusion anisotropy has no effect at temperatures at which corner diffusion is active. However, corner diffusion anisotropy can determine the orientation of triangular islands. It was shown that adatoms tend to accumulate on A-steps as a consequence of corner crossing, thus causing an increase of A-step growth and, finally, their disappearance. Anisotropy in step edge diffusion, though, is important at intermediate temperatures, when corner crossing is not active, in that it determines the transition from dendritic to compact islands. The results found in the study were claimed to be independent of the particular system chosen (Al(111)) but to be valid for all fcc(111) surfaces [155].

The extensive DFT calculations of activation barriers for diffusion of Pt on flat and stepped Pt(111) surfaces by Feibelman [157], allowed a realistic modelling of island formation on Pt(111) through a KMC algorithm making use of the DFT barriers as input values [158]. Besides terrace diffusion, the three other processes included in the model were edge-to-edge (or simply edge) diffusion, edge-to-corner diffusion, and corner-to-edge diffusion. It was first noted that compact islands can only be formed when adatoms can travel frequently from one step to a neighbouring one after crossing the corner between the two. The observation that corner crossing is necessary for

the formation of compact islands, already made in Ref. [153], was thus corroborated. Subsequently, the influence exerted by anisotropy in the three elemental processes on island growth was studied. In agreement with Ref. [155], a switch of edge diffusion anisotropy was found to produce no effect on the island shape, which is a distorted hexagon bounded by B-type steps longer than A-type steps, as obtained by Comsa's group upon deposition above 700 K [20]. The conclusions differ from Ref. [155], when, by reversing corner-to-edge anisotropy, it is found that the island shape stays basically unaltered. It was then shown that only when the disparity in edge-to-corner diffusion is reverted, is the island orientation also inverted. An important conclusion follows from the above observations. In the compact growth regime, most adatoms arriving at the islands from the terrace approach one of the island sides, rather than a corner, due to the lower presence of kinks and corners in compact islands as compared to fractal or dendritic growth. Therefore, the redistribution of the step adatoms determines the island shape evolution much more decisively than the fewer corner adatoms.

The transition from dendritic to compact island structures in epitaxial growth was investigated by means of atomistic methods in a study by Lagally's group [21], where the substrate chosen was a generic fcc(100) surface. The three processes taken into account in the lattice gas model were terrace, edge, and corner diffusion. KMC simulations proved that, where island-corner crossing is suppressed, dendritic, fractal-like islands grow on the substrate. The necessary condition for compact island formation is frequent corner crossing. A basic formalism was also developed which showed that island-corner crossing, and not edge diffusion, is the ultimate process separating fractal and compact growth. Further proof was provided by a growth simulation, starting from an initial square seed where edge diffusion was assumed to be infinitely fast and corner crossing infinitely slow. In this case, the impossibility for the adatoms to cross island edge corners causes a fingering instability which is amplified as the growth proceeds. Several stages of growth are depicted in Fig. 5.8.
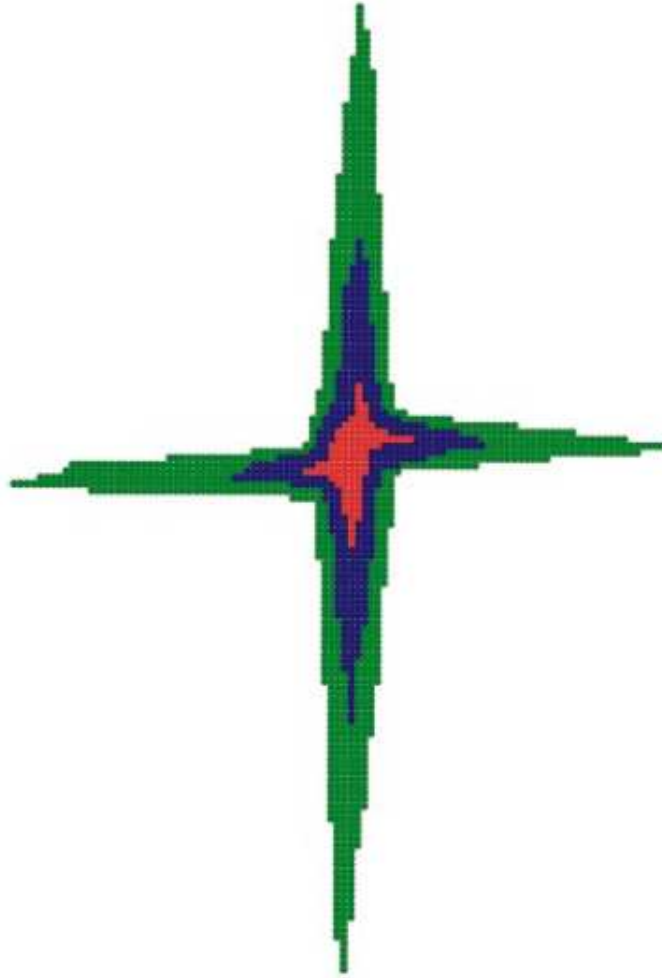
Figure 5.8: Island morphology obtained by means of KMC calculations on an fcc(100) surface assuming infinitely fast edge diffusion and infinitely slow corner crossing. Different colours denote different stages of growth. The number of atoms are 100, 400, and 1000 in the red, blue, and green area, respectively (from Ref. [21]).

STM and atomistic methods were used in one of the seminal studies of Ag island nucleation on Pt(111) and Ag(111) [159]. This investigation, focusing mainly on dendritic growth has been extended in a later study [160], where Ag submonolayer growth on Ag(111) was investigated for a wide range of temperatures. The KMC calculations were performed using barrier heights taken from EMT and EAM calculations and adapted to fit experimental data. These simulations allow useful considerations of those atomistic processes which are responsible for growth. In particular, corner diffusion anisotropy is recognised to cause island shape anisotropy both in growth of

dendritic and compact islands.

Diffusion and pattern formation on strained surfaces deserves a separate discussion. The strain present on reconstructed surfaces determines a modification of adatom diffusion with respect to the ideal bulk-like surface. This can in some cases induce self-organised growth on the surface giving rise to pattern formation.

One of the most widely used substrates for studying nanostructure growth is Au(111), due to the reconstruction naturally displayed at room temperature. Several elements have been deposited on Au(111) in order to follow their diffusion and aggregation. Examples are Ni [161–163], Fe [164], Co [165], Al [166], and Ag [22, 167, 168]. An interesting case of self-ordering on Au(111) was observed when Ni is thermally deposited [161, 162]. Ni islands are observed to nucleate in correspondence with elbows at the confluence of neighbouring $22 \times \sqrt{3}$ domains with different orientations. The reason for this was assumed to be an attractive potential well experienced by Ni adatoms approaching elbows of Au(111). However, the actual mechanism for this ordered nucleation has been found to be a site selective exchange of Ni adatoms with Au surface atoms lying in the elbows [163]. On the other hand, in one of the studies by Chambliss and coworkers [162] it has been pointed out that, where only a single uniaxial domain of the Au(111) reconstruction appears, e.g. in proximity to step edges, Ni islands are observed to nucleate forming a similar finger like pattern to Ag islands previously investigated [162].

The study of Ag growth on Au(111) has also received a good deal of attention [22, 167, 168]. When deposited on Au(111) at submonolayer coverages, Ag adatoms nucleate and form elongated islands, which are either anchored to step edges, for very low coverages (see Fig. 5.9 (a)), or lie on flat terraces far from step edges, when the coverage is increased (see Fig. 5.9 (b)). The islands clearly follow the structure of the underlying Au(111) reconstruction and nucleate parallel to the discomensurration lines on the areas which are not fcc stacked. The fingerlike islands disappear upon annealing to 300^oC,

thus indicating that they represent metastable configurations of the system, rather than the equilibrium state. After one or more monolayers of Ag are deposited, the surface reconstruction disappears altogether and subsequent islands nucleated on the Ag substrate assume a more compact, hexagonal shape.
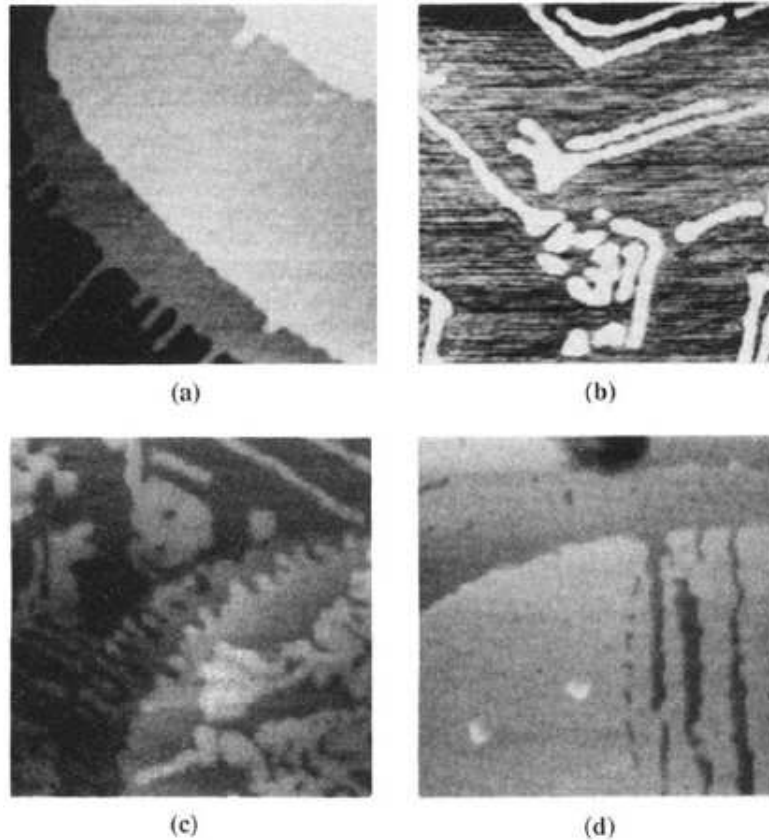
Figure 5.9: $1150 \times 1150\text{Å}^2$ STM images of Ag deposited on Au(111) at different coverages. (a) 0.1 ML, (b) 0.25 ML, (c) 0.75 ML, (d) 1.5 ML (from Ref. [22]).

5.5 Atomistic calculations of diffusion barriers

From the above discussion it clearly emerges how diffusion and self-organised growth on surfaces are deeply related phenomena. In order to gain physical insight into the growth of gold nanofingers, therefore, a thorough numerical study of diffusion on the Au(111) surface has been carried out. Particular attention has been devoted to diffusion along step edges, which are either straight or affected by defects such as kinks or corners.

This study extends a previous work by Ferrando and Treglia, where activation energies for some selected diffusion processes were studied on stepped (111) surfaces of Au and Ag [169].

5.5.1   Methodology

We have compared the height of the barriers obtained in diffusion calculations for different surface configurations but with equal arrangements of first-neighbours of the diffusing adatom. We have found that the number of first-neighbours is by far the most important determinant of the barrier height and that different configurations of second-neighbours and above affect the calculations to a negligible extent.

All diffusion processes have been classified on the basis of the in-plane coordination of the diffusing adatom before and after diffusion. This simplification is allowed by the observation that, in gold, second nearest-neighbour interactions and above have insignificant effects with respect to first nearest-neighbour interactions. In fact, I have compared the height of the barriers obtained in diffusion calculations for different surface configurations but with equal arrangements of first-neighbours of the diffusing adatom. It has been found that the number of first-neighbours is by far the most important determinant of the barrier height and that different configurations of second and more distant neighbours affect the calculations to a negligible extent. In the atomistic calculations included in this thesis, those processes whose occurrence is more likely during the KMC simulations of finger growth have been considered. These processes are shown in Fig. 5.10. In the figure, all processes are labelled by two positive integers connected by an arrow which indicate, respectively, the initial and the final in-plane coordination of the diffusing adatom. Given a diffusion process where the adatom hops from a site of in-plane coordination n to a site of coordination m, we define its inverse by that process where the adatom diffuses from an m-fold to an n-fold coordinated lattice site. In the figure, we choose to show only one process for each pair ($n \rightarrow m$, $m \rightarrow n$). Inverse processes can be obtained in a straightforward manner.
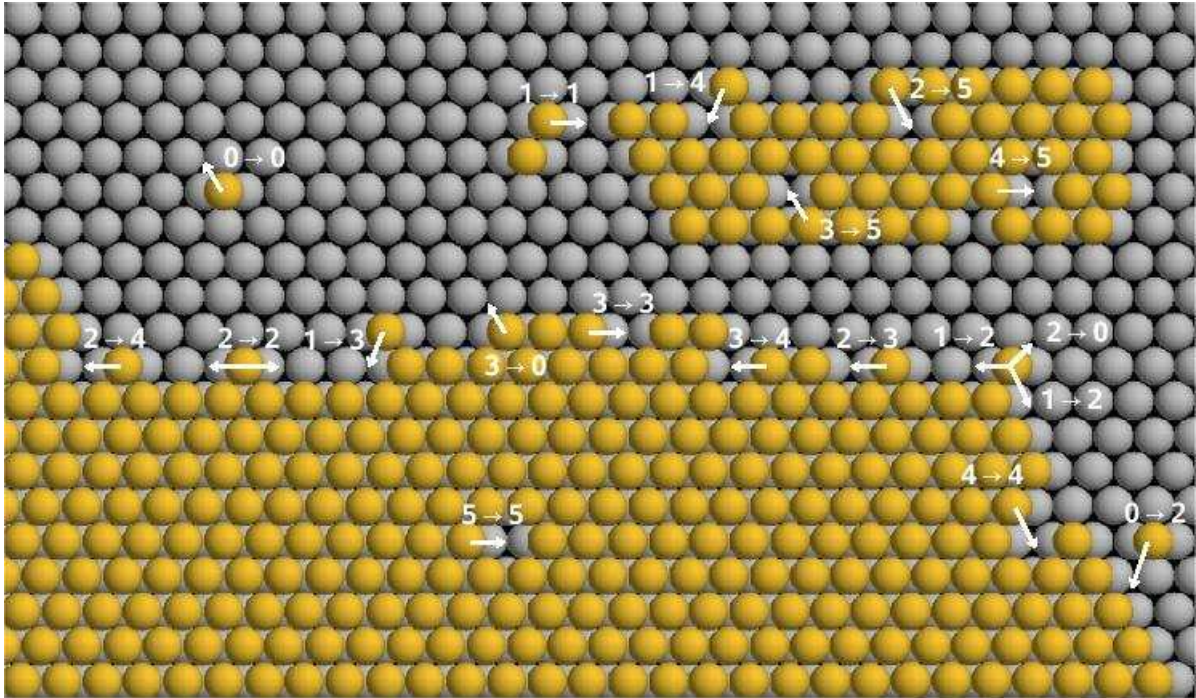
Figure 5.10: Different processes whose activation barriers have been calculated. The first and the second integer indicate the initial and the final in-plane coordination of the diffusing adatom, respectively. Inverse processes are not shown (see text).

The potential chosen to describe interatomic interactions in Au is again the Gupta or RGL potential, which has been described above (see Sect. 2.2). The parameterisation is the same as that used for the optimisation of Au clusters (see Table 3.1).

The unit cell used in the calculations is a slab made of 7 Au(111) planes stacked in ABC fashion, as shown in Fig. 5.11. Each plane contains 10 atoms in the $\langle 1\bar{1}0 \rangle$ close packed direction and 10 atoms in the orthogonal $\langle 11\bar{2} \rangle$ open direction. Periodic boundary conditions are applied in both directions across the surface plane. The diffusing adatom rests on the topmost plane and is led through a straight path connecting the initial and the final site. At each point along the path, the system energy is minimised locally while fixing the diffusing adatom coordinate parallel to the surface plane. The remaining coordinates of the diffusing adatoms, along with the degrees of freedom of the other atoms in the slab, are relaxed. The atoms making up the bottom plane constitute an exception, in that they are kept fixed in their respective positions so as

to simulate the effect of the bulk crystal on the outermost planes.
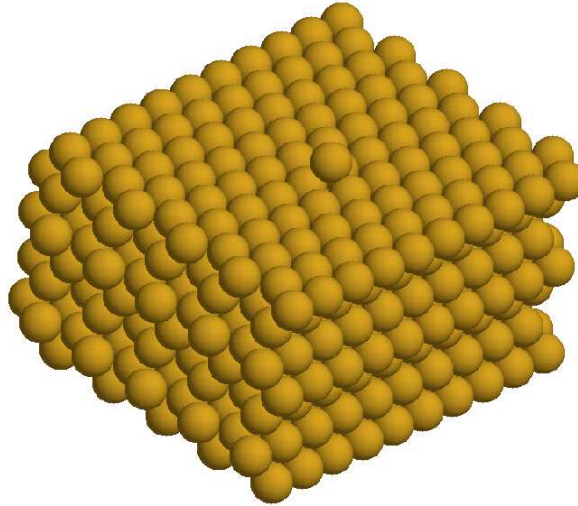
Figure 5.11: Unit cell used for the atomistic calculations of diffusion barriers. Periodic boundary conditions are applied on the surface plane.

Energy minimisation is achieved through a quenching procedure making use of classical MD. Initially, with the system in its unrelaxed state, the classical equations of motion are integrated by means of the velocity-Verlet algorithm [170]. The quenching is accomplished by cancelling all those components of an atom's velocity whose scalar product with the force acting on the atom are negative. This allows the system to relax into the closest local minimum. Quenching is terminated when the system temperature is lower than 10^{-5} K. The diffusion barrier for the process is then obtained by taking the difference between the system energy in the transition state and in its initial state with the diffusing adatom resting on a three-fold hollow site.

5.5.2 Results of atomistic calculations

The results of the diffusion barrier calculations are listed in Table 5.2. Our calculations generally agree with the results found by Ferrando and Treglia [169], with a different

parametrisation of the potential likely being responsible for the slight differences observed.

Process $i \to f$	E_b/eV A |B	Process $i \to f$	E_b/eV A|B	Process $i \to f$	E_b/eV A|B
$0 \to 0$	0.10	$2 \to 0$	0.52 | 0.54		
$0 \to 1$	0.08	$2 \to 1$	0.39 | 0.25	$4 \to 1$	0.57 | 0.67
$0 \to 2$	0.09 | 0.11	$2 \to 2$	0.33 | 0.24	$4 \to 2$	0.54 | 0.63
$0 \to 3$	0.10	$2 \to 3$	0.33 | 0.22	$4 \to 3$	0.53 | 0.61
		$2 \to 4$	0.21 | 0.30	$4 \to 4$	0.56 | 0.55
		$2 \to 5$	0.02	$4 \to 5$	0.31 | 0.31
$1 \to 0$	0.31	$3 \to 0$	0.70		
$1 \to 1$	0.33	$3 \to 1$	0.55 | 0.44		
$1 \to 2$	0.16 | 0.04	$3 \to 2$	0.45 | 0.40	$5 \to 2$	0.54
$1 \to 3$	0.15 | 0.04	$3 \to 3$	0.48 | 0.41	$5 \to 3$	0.52 | 0.51
$1 \to 4$	0.04 | 0.12	$3 \to 4$	0.45 | 0.39	$5 \to 4$	0.52 | 0.53
		$3 \to 5$	0.15 | 0.16	$5 \to 5$	0.46

Table 5.2: Barriers for the diffusion processes included in the KMC model, as calculated with the Gupta potential.

By studying the processes of adatom detachment from a corner site, step edge and kink site, denoted by $1 \to 0$, $2 \to 0$ and $3 \to 0$, respectively, one can notice a roughly linear increase in the height of the activation barrier with increasing initial coordination: the height of the barrier increases by around 0.20 eV for each new first-neighbour in the initial position.

By contrast, the inverse processes, i.e. the capture of a free adatom by a defect on the step, display almost the same activation barrier, regardless of the nature of the final position after diffusion. The values are very similar to the case of diffusion on the bare surface. The reason for this is that the perturbation created by the presence of the defect on the surface (corner, step or kink) is not experienced by the diffusing adatom in the transition state, due to the extremely short-range nature of the interaction. In fact, we have found that the potential of an adatom is influenced dramatically by the presence of a surface defect. However, the effect is noticeable only in close proximity to the defect. For instance, by comparing the system energy at the beginning and at the

end of the processes $0 \to 2$ and $0 \to 3$, we notice that the difference in bonding energy of the diffusing adatom between the two states is 0.44 eV and 0.60 eV, respectively. But the bonding energy of the adatom in the initial position is not significantly lower than for the adatom in an fcc three-fold hollow site far from the defect, the difference being only $2 - 3$ meV.

We can calculate the typical times for each diffusion process occurring at a temperature of 300 K by means of (5.1). For instance, an atom occupying a corner position (in-plane coordination of 1) can move to the nearest step edge site (in-plane coordination of 4) within a typical time of the order of a few ps for an A-type step and 100 ps for a B-type step. Other options are capture by a neighbouring kink site $(1 \to 3)$ and diffusion into the channel opposite the step edge $(1 \to 2)$. Both these processes occur within similar time scales of the order of 100 ps and a few ps for A-type and B-type steps, respectively. However, the expulsion from the corner into the lower terrace $(1 \to 0)$ and the diffusion into an adjacent corner site $(1 \to 1)$ are much slower processes with a characteristic time of around 100 μs. Analogously, an adatom resting in the channel right opposite a step (in-plane coordination of 2) can either diffuse along the step $(2 \to 2)$, or be captured by a kink $(2 \to 3)$ or step edge site $(2 \to 4)$ with almost the same probability. However, the activation energy required for the adatom to leave the channel and reach the terrace $(2 \to 0)$ is much higher than for the former processes.

In conclusion, we have found that the kinetics of free adatom trapping by a surface defect occur on the same time scale, regardless of the particular type of defect. Furthermore, the probability for a free adatom to be captured by a defect is almost the same as that for diffusion on the bare surface. In other words, when an adatom approaches a defect, it will move away from and towards the defect with almost the same probability. However, once the atom is trapped by the defect, it has a low probability of being released back onto the lower terrace. This is due to the extremely sticky, short

range nature of the interatomic potential of gold [41].

The calculations described in this section provide a set of barriers for a natural hierarchy of diffusion processes to be used in an atomistic model of the surface. The kinetics of the adatoms diffusing on the Au(111) surface can then been simulated by means of an algorithm such as Monte Carlo as will be described in Sect. 7.1.

Chapter 6

Atomistic modelling of nanofinger growth

6.1 Lattice gas model

After a careful examination of the experimental data, a model for the finger growth has been set up, where the phenomenon results from the combination of two processes: the continuous flow of extracted atoms from the upper to the lower terrace, and the subsequent diffusion of these isolated atoms across the lower terrace. In this model, only atoms belonging to the uppermost surface are considered. The system is treated as a lattice gas. The only possible sites for atoms to rest in are represented as nodes in a two dimensional grid with three-fold symmetry. Each node in the grid corresponds to a three-fold hollow site on the fcc(111) surface which is the substrate of the lattice gas. Fig. 6.1 gives a schematical depiction of the model.

Thermally activated diffusion is reproduced by allowing each atom to hop into one of the unoccupied neighbouring lattice sites. The rate r for an atom to hop into a nearest neighbour site is expressed by the usual Arrhenius law already seen in Sect. 5.2:

$$r = \nu_0 \exp\left(-\frac{E_b}{k_B T}\right);$$ \hfill (6.1)

where E_b is the energy barrier to diffusion in the considered direction, k_B is the Boltzmann constant, T is the system temperature, and ν_0 is the hop attempt frequency.

An atom can hop into each one of its 6 neighbouring sites with a different rate r_i
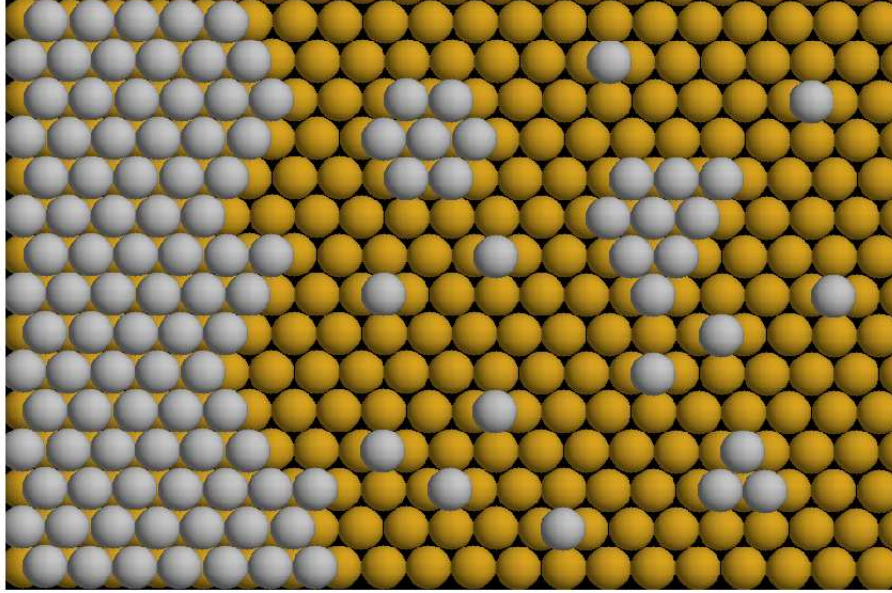
Figure 6.1: Sphere model of a lattice gas. The topmost atoms (grey) are those taken into account in the model. The atoms rest in three-fold hollow sites between three adjacent atoms in the substrate (yellow), which are not included in the lattice gas.

($1 \leq i \leq 6$), depending on the height of the barrier E_i to diffuse into that particular site. Each atom k in the lattice gas is thus associated with a diffusion rate $r(k)$, which is obtained by summing up the single rates for the diffusion onto each of the unoccupied nearest neighbour sites in the following way:

$$r(k) = \sum_{i=1}^{6} r_i(k).$$ (6.2)

A total rate for the whole system can then be calculated as:

$$r_T = \sum_{k} r(k);$$ (6.3)

where the sum is over all atoms making up the lattice gas.

Since we are concerned with a stepped surface, the initial configuration has been chosen to be a monoatomic step running along the [11$\bar{2}$] direction (one of the three

equivalent open directions) on the close-packed surface. The simulation unit cell is rectangular, with one of the close packed directions of the surface running parallel to the longer side of the rectangle. Periodic boundary conditions are imposed only in the surface plane, in the direction parallel to the step edge. Typically, at the beginning of each simulation the lattice gas is made up of ≈ 400 close packed horizontal rows, each containing ≈ 250 atoms - i.e. the total number of atoms making up the system is $\approx 10^5$. This simulation cell is shown in Fig. 6.2.
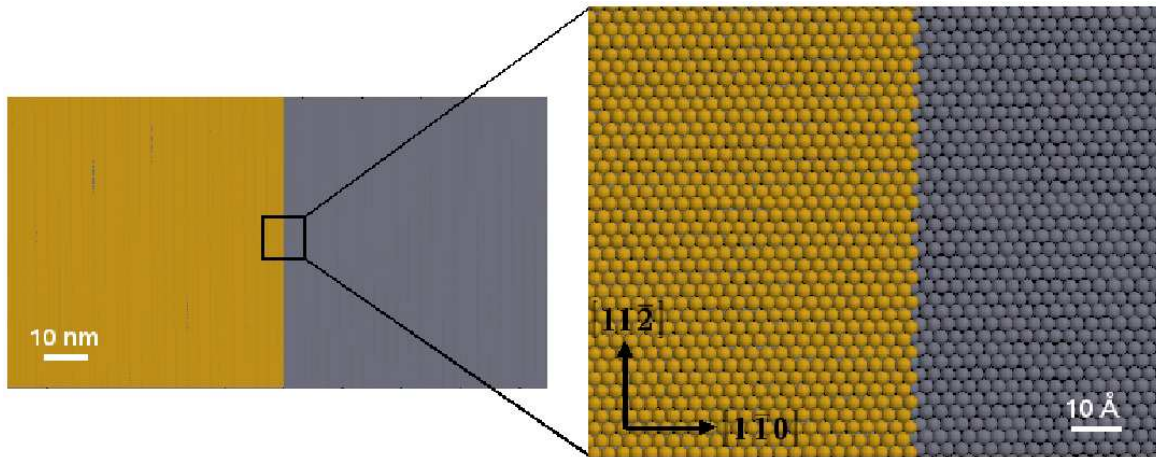
Figure 6.2: (Left) Simulation unit cell used in the KMC calculations. The atoms in the upper terrace are indicated in yellow and those on the lower terrace in grey. (Right) Magnified view of the step edge area, where the initial structure and orientation of the step edge are shown.

The dynamics of the atoms on the surface are simulated by means of a Kinetic Monte Carlo (KMC) algorithm based on the Bortz, Kalos and Lebowitz (BKL) algorithm [171, 172], to which some modifications have been made. During each iteration of the algorithm, an atom is selected to diffuse, the selection being biased according to the diffusion rate of each atom. The diffusion rate is proportional to the probability for the atom to diffuse. Once the diffusion step has been accomplished, the system is updated (i.e. the diffusion rates of the atoms affected by the diffusion process are recalculated) and the next iteration takes place. At the end of each iteration the system time is advanced by an amount which depends on the system configuration before

diffusion. In order to assign a time interval Δt for the current step, a random number α is generated in the range $0 - 1$, and Δt is calculated as:

$$\Delta t = -\frac{\ln \alpha}{r_T}. \tag{6.4}$$

The above expression is derived from the theory of random processes, which predicts that, for a system with a mean lifetime of τ, the probability of not decaying scales with the length of the time interval dt as:

$$p(dt) = \exp \frac{-dt}{\tau}. \tag{6.5}$$

By replacing the mean lifetime τ in (6.5) by the inverse of the total rate $1/r_T$, one obtains (6.4), where the random number α replaces the probability $p(dt)$.

The effect of the STM tip on the surface is the element which differentiates our algorithm from the typical BKL. The perturbation produced by the STM tip on the system is taken into account by letting the outermost atom on the upper terrace be extracted from the step edge. After extraction, the atom is displaced a variable distance away from its original position along the scan direction, which is always orthogonal to the orientation of the initial step. One atom is extracted at each simulated tip passage, with the atom selected for extraction-displacement being the one located at the site of the orthogonal projection of the tip apex onto the surface. The modelled tip is assumed to follow the same trajectory as the actual raster scan performed by the real STM tip during a scan. The distance between two consecutive scan lines - i.e. the vertical displacement of the tip - is determined by the ratio of the vertical dimension of the scanned area to the number of scan lines. As the scan area in all simulations is ≈ 60 nm high and the typical number of scan lines chosen is ≈ 250, in agreement with experiment, the tip vertical displacement is roughly equal to the distance between two consecutive rows of close packed atoms in the ideal Au(111) surface (≈ 2.5 Å). The flow chart in Fig. 6.3 briefly describes the algorithm structure.

In our model the $22 \times \sqrt{3}$ reconstruction of the Au(111) surface is not explicitly
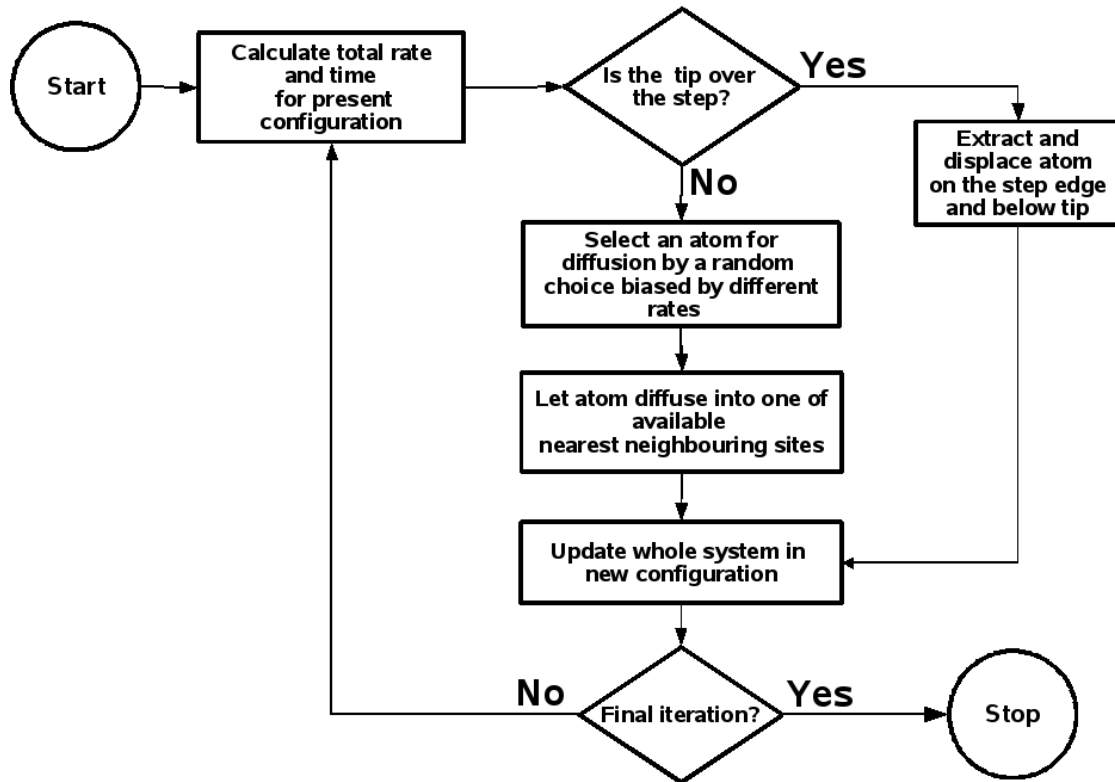
Figure 6.3: Flow chart of the modified BKL algorithm used in the calculations of finger formation on Au(111).

taken into account, because a model with reconstruction would be so complicated as to become practically intractable. In fact, on the reconstructed surface, even the diffusion barrier for a single isolated adatom depends strongly on its position within the reconstruction elementary cell (cfr. Sect. 5.3), so that the single barrier of the unreconstructed surface is replaced by a large set of barriers. When considering a growing finger, the environment of each atom in the finger is different, so that the set of possible barriers becomes enormous. In this case, simple KMC becomes infeasible. On the other hand, accelerated MD or on-the-fly Monte Carlo methods [173–175], even though applicable in principle, are not yet able to cope with the very large sizes and long time scales involved in the gold nanofinger growth. Our choice has thus been to consider the unreconstructed surface, to show that the fingering instability itself is not due to reconstruction, and to discuss what are the possible effects of reconstruction on

finger shape.

6.2 Simple model

As a test of the validity of the model, some calculations have been carried out after introducing a further, dramatic simplification. It is assumed that only interactions between the diffusing adatom and its nearest neighbours are responsible for the height of the energy barrier the adatom has to overcome in order to diffuse. Therefore the diffusion rate is the same for each of the available nearest neighbouring sites around the adatom. The diffusion barriers are assumed simply to increase linearly with the number of nearest neighbours of the adatom in the position it occupied before diffusion. This choice was motivated by the atomistic picture of surface diffusion, whereby an isolated adatom on the bare surface experiences a certain energy barrier. When the adatom is a part of a structure on the surface, i.e. if it has any in-plane nearest neighbours, the energy barrier to jump to an adjacent unoccupied site will be increased by an amount proportional to the number of neighbours. This is tantamount to assuming that, due to the atomic interactions, each in-plane neighbour contributes to the bonding energy of the adatom in its present position by the same amount.

The maximum in-plane coordination of an adatom lying on an fcc(111) surface is 6, the number of processes taken into account in the model is also 6, corresponding to diffusion from a site where the adatom can have a number of nearest neighbours between 0 and 5. Atoms with an in-plane full coordination of 6 are not allowed to diffuse. Given an adatom with an in-plane coordination of n_{nb}, then, the activation energy E_d for diffusion into any of the available directions is obtained as:

$$E_d = E_0 + n_{nb}E_B; \tag{6.6}$$

where E_0 is the diffusion barrier on the bare surface and E_B is the contribution from each neighbour to the adatom binding energy. The diffusion rate r then is immediately

found as:

$$r = n_{nb}\nu_0 \exp\left(\frac{E_d}{k_B T}\right); \qquad (6.7)$$

where, as usual, ν_0 is the hop attempt frequency, k_B is the Boltzmann constant, and T is the temperature.

The barrier calculated in (6.6) represents an oversimplification with respect to the diffusion barriers actually experienced by an adatom resting on the Au(111) surface. The arrangement of the neighbouring atoms to the diffusing adatom in the final site after diffusion is not taken into account. This provides the same energy barrier for processes which have been calculated to be different (cfr. Sect. 5.5 and Ref. [169]).

A Fortran 90 code has been developed to implement this simplified model. All diffusing adatoms are divided into 6 classes, depending on the number of in-plane nearest neighbours, and therefore on their diffusion rate. Atoms belonging to the same class are equivalent. Let r_i be the diffusion rate of all atoms belonging to class i ($0 \le i \le 5$). At each iteration, one of the atoms is either extracted out of the step edge and displaced by the tip, or allowed to diffuse, according to the algorithm of Fig. 6.3. When a diffusion step takes place, a class is first selected. A random number β is generated between 0 and the system total rate r_T. If β is within the interval $[0, r_0]$, then the class 0 is selected; otherwise the first class i is selected for which the inequality $\sum_{j=0}^{i-i} r_j < \beta \le r_i$, with $1 \le i \le 5$, holds. After the choice of the class, and therefore of the diffusion process, has been accomplished, one atom belonging to the selected class is randomly picked for diffusion. After diffusion the system is updated and a new iteration starts.

6.3   Results of the simplified model for Au(111)

For this series of KMC calculations, the set of barriers listed in Table 6.1 have been used, where E_i is defined as the activation barrier for a diffusion process where the adatom has i in plane nearest neighbours in its initial lattice site. The value of 0.20 eV

has been chosen as the binding energy due to each nearest neighbouring atom, and 0.15 eV as the activation energy to diffusion on the flat terrace. This choice was motivated by both my own atomistic calculations of diffusion barriers (see Sect. 5.5) and previous results in the literature [126, 134, 169]. The hopping attempt rate has been set to the *typical* value of 10^{12} s^{-1}, in agreement with earlier calculations (see Table 5.1).

Starting in-plane coordination of diffusing atom (i)	Energy barrier (E_i / eV)
0	0.15
1	0.35
2	0.55
3	0.75
4	0.95
5	1.15

Table 6.1: Energy barriers for the different diffusion processes included in the model. Fully 6-coordinated atoms cannot diffuse.

As described above, at each forward passage over the step edge, the tip displaces the outermost atom of the upper terrace by 100 times the nearest neighbour distance from its previous position. For gold the nearest neighbour distance is ≈ 2.9 Å. By simulating a scan rate of 200 Hz and by setting the distance between two consecutive scan lines to approximately 2.5 Å, corresponding to the distance between two adjacent close-packed rows of atoms, we were able to reproduce the instability giving rise to the finger pattern.

The fingers thus created have been found to display a thickness ranging from about 9 to 16 nm. However, experimentally the finger thickness was measured to be distributed within the interval 3.5 to 10 nm, with an average value between 5.50 and 6 nm. Furthermore, the simulated fingers are more closely spaced than the experimental ones. Typically, the spacing between two calculated fingers is between 1.5 and 3 nm, as opposed to a much broader distribution ($2 - 20$ nm) obtained from the experiments. An example of a typical result obtained in the course of this series of calculations is

shown in Fig. 6.4. The vertical straight line in Fig. 6.4 (b) and (c) indicates the position occupied by the step edge at the beginning of the simulation run. The overall effect of the etching by the STM tip is to cause the step edge to recede from its original position.
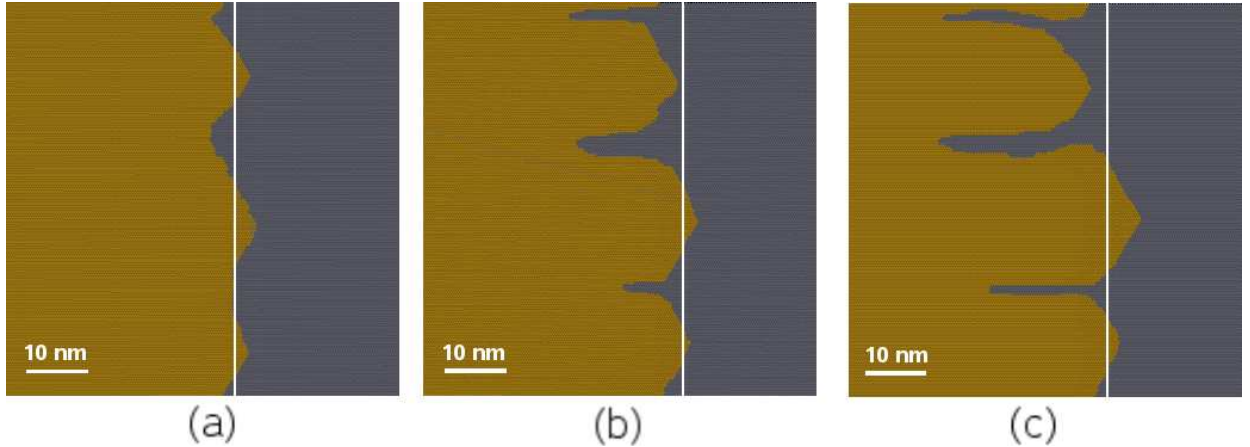
Figure 6.4: Series of images taken during the process of simulated finger growth at 300 K with a scan rate of 200 Hz and the set of barriers listed in Table 6.1. (a) System configuration after 6×10^6 iterations, system time 818.8 s; (b) system configuration after 10^9 iterations, system time 1317.5 s; (c) system configuration after 1.3×10^9 iterations, system time 1672.0 s. The vertical white line indicates the initial step edge.

The remarkable result is that, even with such a simplistic model, a kinetic instability, causing the fingering of the step edge, can be predicted and simulated. The differences between the simulated and the experimentally obtained pattern are probably due to the approximations inherent in our model.

The configuration assumed by the system as an effect of the STM induced perturbation is a metastable state, as proved by the experiments [14] and confirmed by the calculations. In Fig. 6.5 the annealing of a fingered step is simulated. Under annealing at 400 K for about 1 minute, the pattern is completely smoothed out and the step regains the original quasi straight configuration before manipulation.

An investigation of the effect of modifying the value of the scan rate has been carried out, which has led to the conclusion that, when the scan rate is increased from
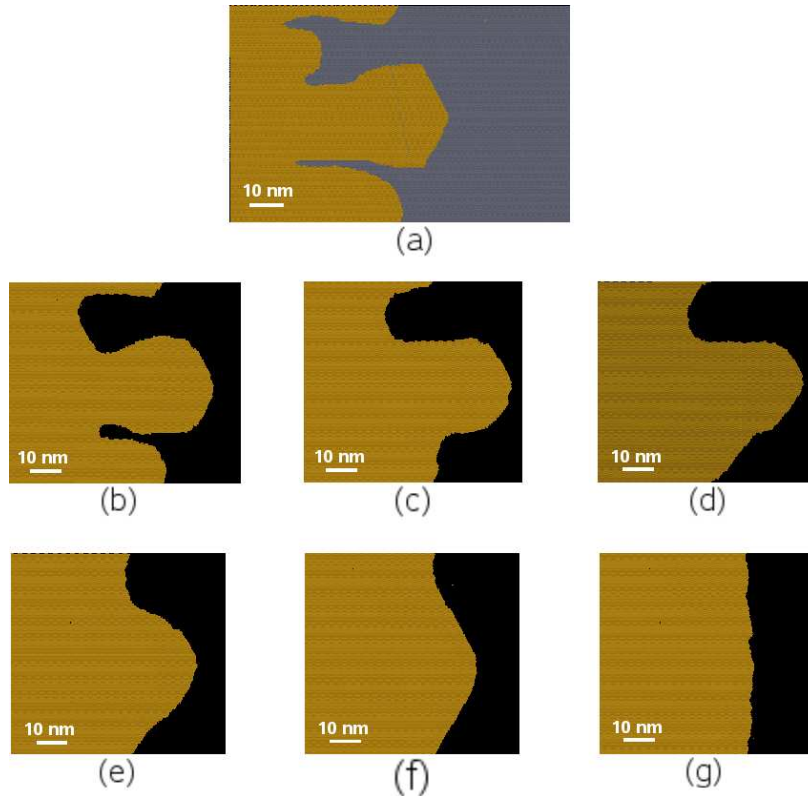
Figure 6.5: Simulated annealing of a fingered step edge at 400 K. In panels (b) to (g), only the atoms in the topmost plane are shown. (a) Initial configuration, system time 0 s; (b) configuration after 10^8 iterations, system time 1.3 s; (c) configuration after 3×10^8 iterations, system time 3.9 s; (d) configuration after 6×10^8 iterations, system time 8.0 s; (e) configuration after 1.5×10^9 iterations, system time 20.4 s; (f) configuration after 2×10^9 iterations, system time 27.5 s; (g) configuration after 4×10^9 iterations, system time 57.0 s.

the initial value of 200 Hz, the finger formation occurs more rapidly in terms of system time, but the pattern remains the same, with the finger thickness distribution and spacing unchanged. On the other hand, when the scan rate is decreased, a threshold rate is reached below which no instability is observed. With the set of barriers of Table 6.1 and at a temperature of 300 K, the threshold for the rate can be located within the interval of 50 to 100 Hz.

In order to understand the influence of the six types of diffusion processes considered here on the pattern formation and growth, we selectively changed the energy barriers regulating each process class. The barrier responsible for the diffusion of an adatom

with initial in-plane coordination of 2 (i.e. E_2) turns out to be crucial. When its value is lowered to 0.45 eV, the pattern is modified as shown in Fig. 6.6 (a). The step is observed to rearrange along two of the three equivalent close packed directions thus giving rise to a quasi-regular zig-zag pattern. On the other hand, by increasing the E_2 barrier height to 0.65 eV, the pattern is modified as shown in Fig. 6.6 (b). Thinner fingers appear on the edge of the upper terrace, along with a number of islands on the lower terrace. Some of the fingers, as well as the islands, lose the compact shape assumed in the previous calculations and display a more rugged profile of fractal type.
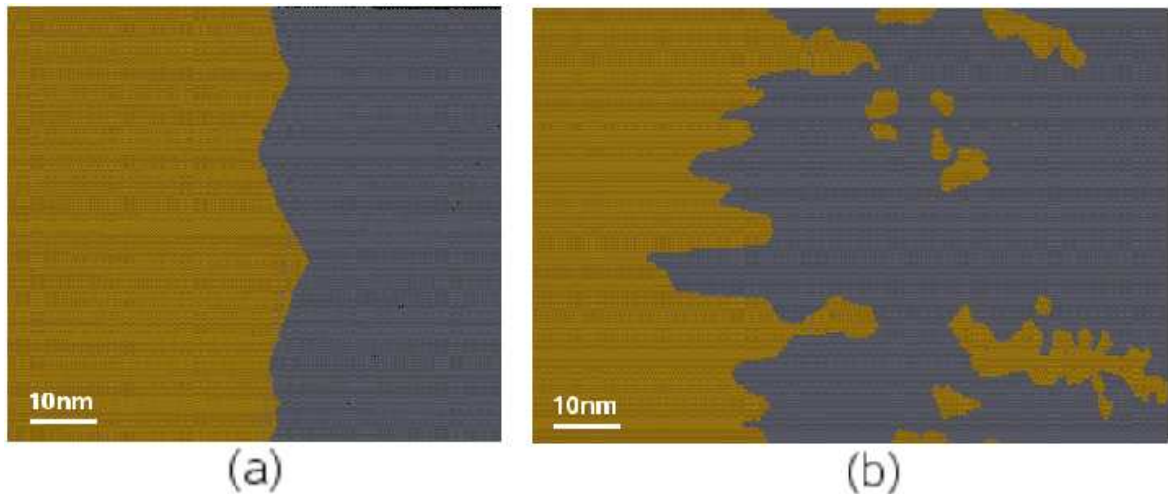
Figure 6.6: Patterns obtained after 109 iterations at 300 K (t = 110 s and 111 s for (a) and (b), respectively), with a scan rate of 200 Hz and E_2 barrier of 0.45 eV (a), and 0.65 eV (b).

Fractal growth is also encountered when the system temperature is lowered to 250 K. Using the set of barriers listed in Table 6.1 and with a scan rate of 200 Hz, a pattern of the type shown in Fig. 6.7 is obtained. In this case, the thickness of the fingers is reduced dramatically, with most of them displaying a width within the range 2.5 to around 4 nm. In this case, as well as in the previous one, fairly compact, elongated structures are observed, along with structures following a fractal like growth.

A comparison of the number of processes occurring during a typical run at room temperature and one at 250 K has also been made. In both cases, the great majority of
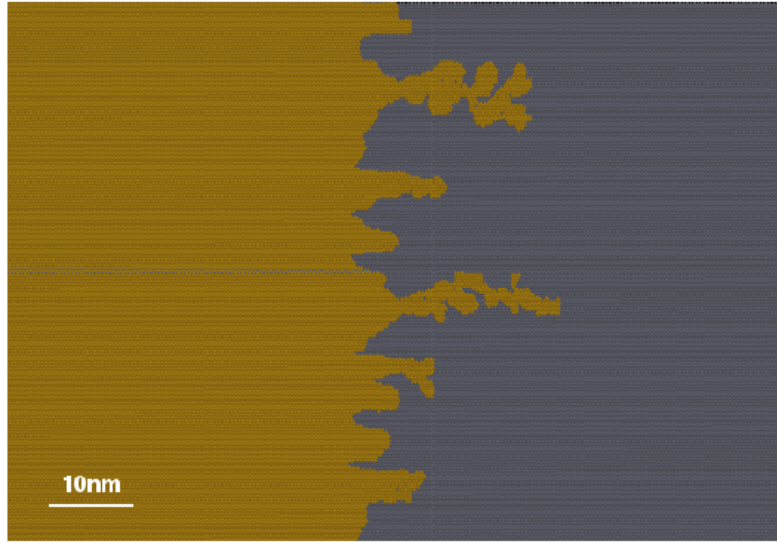
Figure 6.7: Pattern obtained after 10^9 iterations at 250 K (t = 30 s), with a scan rate of 200 Hz and the set of barriers listed in Table 6.1.

processes are diffusions of free adatoms on the lower terrace, which amount to 99.978% and 99.999% of the total number of diffusion events for the calculations carried out at 300 K and 250 K, respectively. On the other hand, as the temperature is lowered, the remaining diffusion processes are affected in a different way. The ratio of diffusion of adatoms with initial single coordination to the total number of diffusions decreases to 0.0019% at 250 K, from the value of 0.0043% at 300 K. An even more pronounced fall can be seen for the diffusion of adatoms with initial double coordination. The ratio of these processes to the total plummets from 0.017% at 300 K, to 0.002% at 250 K. The probabilities for other processes to occur are negligible compared to these. The decrease of temperature thus causes an increase in probability for the diffusion of free adatoms on the bare surface, while at the same time hindering those processes with higher energy barriers. In particular, the decreased probability of edge diffusion, which is included among the processes with initial coordination of 2, explains the reason why at 250 K the structures grown at the step edge are much less compact and smooth than those which are found at room temperature.

The mechanism giving rise to the onset of the instability seems to be a delicate

interplay between all of the processes involved. Counting the processes which occur during diffusion can help us to understand the transition between compact elongated finger structures in the pattern and branched, fractal-like formations. Comparing calculations for the same set of barriers but at temperatures of 250 K and 300 K, the kinetics of the system turn out to be different in the two cases. At the lower temperature, some processes are *frozen*, thus resulting in those processes with lower activation barriers being favoured. This is to be expected given the Arrhenius law governing the probability/rate for each class of events. If we define a process as active when its occurrence rate is at least $1\,\mathrm{s}^{-1}$, then it is possible to work out an onset temperature T_{ons} for each process. From Eq. (6.1) one obtains immediately that the onset temperature for a thermally activated process with energy barrier E_i is [121]:

$$T_{ons} = 420\,\mathrm{K} \times (E_d/\mathrm{eV}) . \tag{6.8}$$

From Eq.(6.8) it can be calculated that at 250 K, the diffusion of adatoms with initial double coordination (E_2) is seriously frustrated because the onset temperature for this type of process lies just below 250 K.

In conclusion, a model of the Au(111) surface subject to the external perturbation of an STM field has been set up, in an attempt to reproduce the experimentally observed phenomenon of step fingering while preserving the highest possible degree of simplicity. The phenomenon investigated here is reminiscent of the BZ instability for homoepitaxial growth of metals in the step-flow regime [84,85,176,177] (see Sect. 4.2.2). In our case, as well as in the case studied by BZ, the instability is prompted by the tendency displayed by free adatoms to accumulate at regions of higher convex curvature. The fundamental difference between the present system and the BZ instability is that the whole phonemon occurs here on the lower terrace, which allows one not to assume anything like an Ehrlich-Schwoebel barrier [90] in the model.

An imperfect quantitative correspondence with the experimental data has been reached, probably due to the significant approximations inherent in the model. This

prompts the need for a more refined model, in order to give a more realistic description of the physical system. Such a model will be presented in Chap. 7.

6.4   Results for Ag(111)

By means of a different choice of barriers, a simulation of nanofinger growth on Ag(111) has also been performed using the simple model. The set of diffusion barriers have been chosen on the basis of the experimental evidence [19] and previous calculations [16, 18, 126, 131, 132, 134] (see also Table 5.1) and are listed in Table 6.2.

Starting in-plane coordination of diffusing atom (i)	Energy barrier (E_i / eV)
0	0.10
1	0.18
2	0.25
3	0.5

Table 6.2: Energy barriers for the different diffusion processes included in the model. Adatoms with in-plane coordination higher than 3 cannot diffuse.

At a temperature of 300 K the threshold scan frequency to obtain a pattern such as that shown in Fig. 6.8 is of the order of 1 MHz. As in the simulation of pattern formation on Au, high scan rates are required in order to prevent step annealing, as the diffusion barriers chosen are probably too low. Overall, the typical pattern obtained at 300 K on Ag(111) does not seem to differ dramatically from that on Au(111) at 300 K (Fig. 6.4). Also in this case a pattern made of thick, closely spaced fingers is produced. As opposed to gold, the spread out pattern obtained on silver bears a closer resemblance to the available experimental data (Fig. 6.9).

As the temperature is varied, the pattern on Ag(111) follows a similar trend to that on Au(111). At lower temperatures a tendency of fingers to develop secondary branches is observed, which leads to a fractal profile for temperatures lower than 200 K. A phase transition between multiple branched and compact fingers is observed between 260 and 280 K, which corresponds to a sudden increase in diffusion of double coordi-
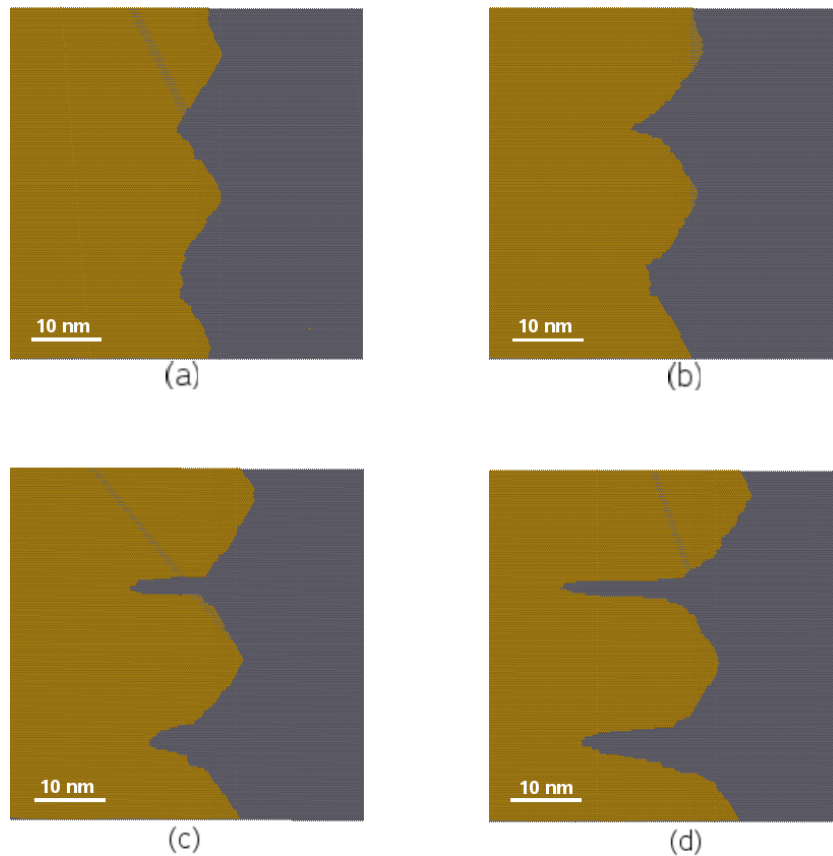
Figure 6.8: Pattern obtained with the set of barriers listed in Table 6.2 at 300 K and with a scan frequency of 2 MHz. (a) System configuration after 5×10^8 iterations, system time 29 ms; (b) configuration after 6×10^8 iterations, system time 34 ms; (c) configuration after 8×10^8 KMC iterations, system time 45 ms; (d) configuration after 1×10^9 KMC iterations, system time 55 ms.

nated adatoms at the expense of diffusion of free adatoms (Fig. 6.11). As diffusion of single coordinated atoms seems to remain basically invariant in the range of investigated temperatures, the passage from branched quasi-fractal to compact fingers can be attributed to diffusion of doubly coordinated adatoms. Doubly coordinated adatoms are those which are attached to step edges, therefore a high mobility of this class of atoms is expected to produce a smoothing effect on the pattern. On the other hand, if the diffusion on step edges is hindered, the system is brought out of equilibrium by a further amount, which results in random bumps accidentally formed on a finger edge to give rise to secondary branches instead of being smoothed out.
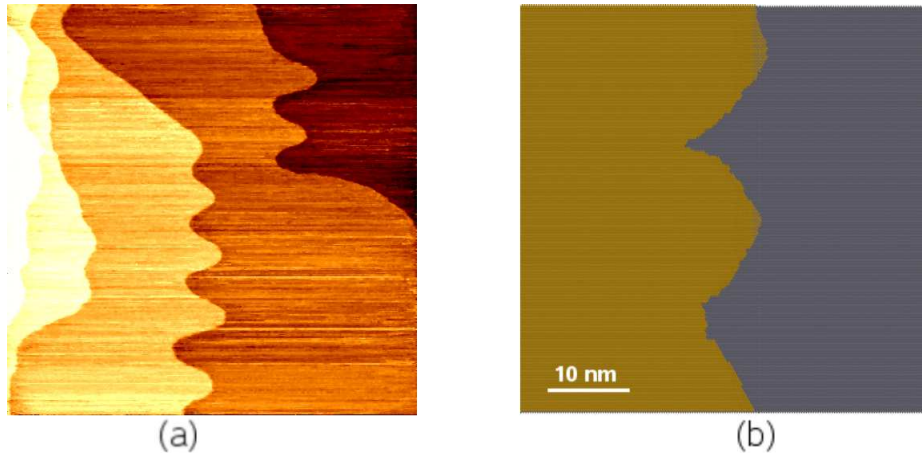
Figure 6.9: Comparison between calculated and experimental fingers on Ag(111). (a) 200×200 nm^2 STM scan (tunneling current = 0.2 nA, tip-sample bias = 1.0 V) of a vicinal Ag(111) surface previously manipulated by scanning at a tunneling current of 50 nA and a tip-sample bias of 2.3 V. (b) Results of KMC calculations on Ag(111). System configuration after 6×10^8 iterations, system time 34 ms.

In conclusion, the simulations carried out with this simplified model on Ag(111) resemble the experimental data better than on the simulations on Au(111). The model describes fairly well the phenomenon of nanofinger growth on Ag(111) as a kinetic instability driven by the effect of the STM tip on the step edge adatoms.
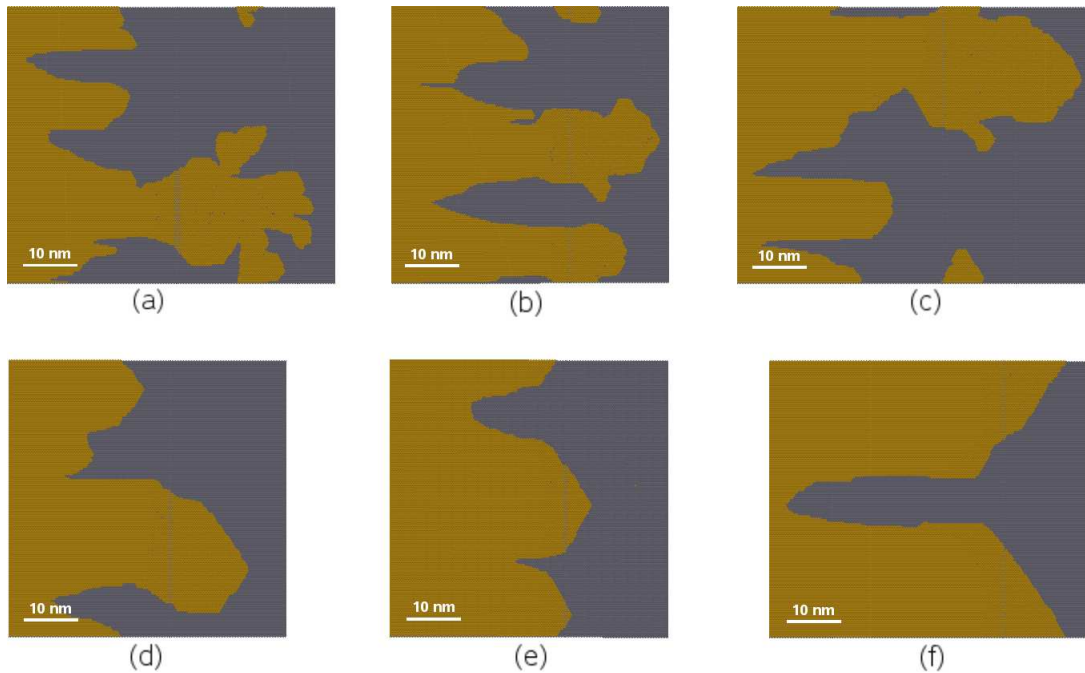
Figure 6.10: Examples of patterns obtained on Ag(111) at different temperatures using a scan rate of 2 MHz; (b) T = 250 K, configuration after 7×10^8 iterations, system time 10 ms; (c) T = 260 K, configuration after 9×10^8 iterations, system time 14 ms; (d) T = 280 K, configuration after 1×10^9 iterations, system time 12 ms; (e) T = 310 K, configuration after 1.9×10^9 iterations, system time 20 ms; (f) T = 320 K, configuration after 2×10^9 iterations, system time 20 ms.
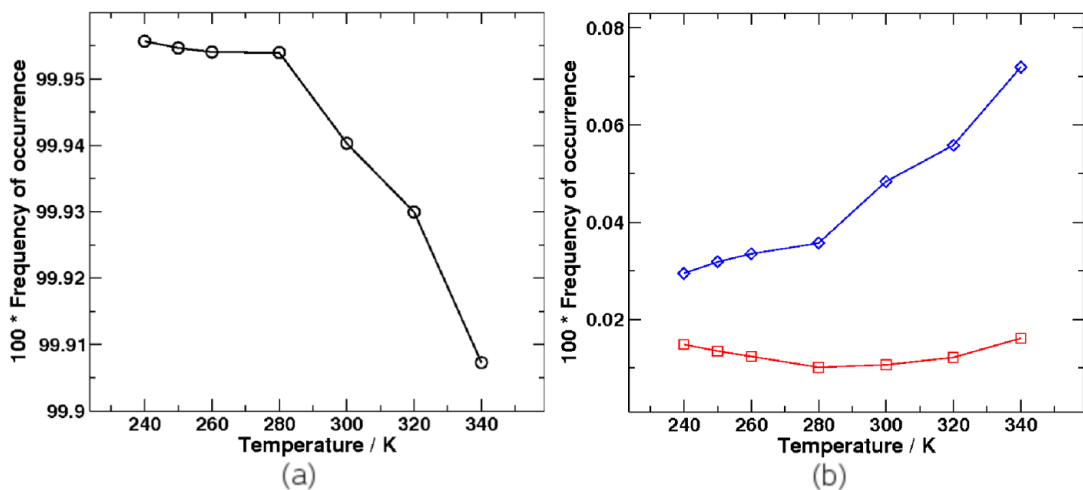
Figure 6.11: (a) Frequency of occurrence of diffusion on the bare terrace as a function of temperature. (b) Frequency of occurrence of single coordinated (red) and doubly coordinated (blue) adatoms as a function of temperature.

Chapter 7

Modelling atomistic processes

7.1 Improved lattice gas model

The simple bond-breaking model described in Sect. 6.2 is able to reproduce a fingering instability, thus allowing a qualitative explanation of the phenomenon. However, neither the shape nor the thickness of the fingers obtained with that model are in agreement with experiments. These results have motivated the development of a more refined model, incorporating more realistic activation barriers for the diffusion processes. As we shall see in the following, this new model allows a deeper insight into the phenomenon.

In order to reproduce the adatom diffusion on the surface, I have used the natural hierarchy of processes whose activation energies have been calculated as described in Sect. 5.5. Therefore, the same algorithm presented in Sect. 6.1 and Fig. 6.3 has been modified to take into account the series of processes listed in Table 5.2.

A c++ code has been developed which can implement this more realistic model of the surface. The two branches of the algorithm in Fig. 6.3 - i.e. adatom diffusion and adatom extraction/displacement by the tip - remain substantially the same, but the diffusion of an adatom can now follow many more channels than in the simplified version of the algorithm in Sect. 6.2.

The code is based on several classes built to reproduce the different elements making up the system. The *grid* where the adatoms move is provided by a class which is

implemented by two interpenetrated two dimensional arrays of *sites*, in order to repro-
duced the three fold symmetry of the fcc(111) surface. A site, i.e. a node in the grid,
is surrounded by 6 nearest neighbouring sites and can either be empty or occupied by
an adatom. The grid keeps track of the occupation numbers and updates the values
on a site when needed.

An adatom hopping between two adjacent nodes in the grid is modelled by the *atom*
class. An atom is characterised by an index and three positive integers which give its
coordinates in the grid. Each atom bears a series of neighbour lists. In one array
the nearest neighbours to the atom in the current position are stored. The rates for
diffusion into each of the available neighbouring unoccupied sites are stored in another
array. The rates are calculated as in (6.1), where the hopping attempt ν_0 has been
set to a typical value of 10^{12} s^{-1}. The value of the activation energy E_b depends on
the particular diffusion process. According to the calculations in Sect. 5.5, all possible
diffusion processes have been classified on the basis of the number of nearest neighbours
to the adatom in its initial and final position before and after diffusion, respectively.
Each process can thus be assigned an activation energy (see Table 5.2) and, therefore,
a rate. The total rate $r(k)$ for an atom k can then be obtained simply by summing up
the rates for diffusion in one direction, as shown in equation (6.2).

A *surface* is made of a grid and an array of atoms resting on the grid nodes. The
surface class calculates adatom diffusion rates and, when an adatom is selected for
diffusion, chooses the site for the adatom to diffuse into. The direction selection is
accomplished by first generating a random number β between 0 and the total rate
$r(k)$ of the selected atom k. The random number is then compared to the diffusion
rates $r_j(k)$ for diffusion into each of the available sites stored in the list associated to
the atom k. If $\beta \leq r_0(k)$, then the first direction in the list is chosen for diffusion.
Otherwise, the first direction associated with the rate $r_i(k)$ is selected for which the
inequality $\sum_{j=0}^{i-1} r_j < \beta \leq r_i$ $(1 \leq i \leq 6)$ holds.

The selection of which adatom is to diffuse during an iteration is accomplished by a binary tree built on the grid node. The tree comprises the leaves, a root and the branches connecting the former to the latter. Each leaf of the tree is associated with two grid nodes. A leaf contains a *value* field which is filled with the sum of the total diffusion rates of the adatoms occupying each of the two grid nodes (0 is considered as the diffusion rate of an unoccupied node). The upper level of the tree is constructed by associating a new tree element for each pair of leaves. The value field of a tree element in the upper level is obtained as the sum of value fields of the lower-lying branch associated with it. New levels can be constructed in the same way until a level is reached containing only one element. This is defined as the tree root. Of course all tree levels, as well as the grid, have to contain a power of two elements. The choice of an atom for diffusion starts by generating a random number between 0 and the value contained in the root. If the random number is less than or equal to the value stored in the first tree element associated with the root, then this is the next element to consider. Otherwise the other tree element is considered. Another random number between 0 and the value in the selected tree element is generated and the same procedure as for the root is undertaken to choose one element in the level below the current element. The iteration is continued until the level of the grid is reached and one of the grid nodes is selected. The above procedure is particularly efficient and it displays the advantage that its complexity scales as the logarithm of the number of adatoms (or grid nodes) considered in the model.

Finally, the *tip* class is introduced to take into account the perturbation caused by the STM tip. As in the simplified model, the effect of the electric tip is simulated by extracting one atom out of the step edge at each tip passage. The tip, thus, selects the outermost atom in the upper terrace at the current scan line and moves it by an arbitrary distance along the scan direction. The typical displacement distance has again been chosen to be 100 times the nearest neighbour distance in Au, which is ≈ 2.9 Å.

7.2   Results of KMC calculations of finger growth

The set of activation barriers listed in Table 5.2 have been used as input parameters for the KMC code described in Sect. 7.1. In those cases where the barrier for A-type and B-type steps differ, the average between the two values in the KMC calculations has been chosen.

When the code is run at a system temperature of 300 K, a distinctive zig-zag pattern is observed for the step reorganisation after the STM scan. The step tends to rearrange along two of the three equivalent close packed directions, giving rise to an alternation of straight segments forming alternatively angles of 120° and 240° to each other. The system eventually relaxes towards a quasi-periodical pattern, with periodicity around 30 nm, probably due to the periodic boundary conditions imposed on the simulation unit cell. This configuration is finally reached, irrespective of the scan rate and the displacement length chosen for the atom detachment from the upper terrace. In Fig. 7.1, a series of images are shown for a KMC calculation carried out at 300 K, using a scan rate of 500 Hz and a displacement of 100 times the nearest neighbour distance.

When the system temperature is reduced to 200 K, the pattern formed on the step edge changes completely. For a sufficiently high scan rate, the instability producing the finger pattern starts to appear after a certain number of iterations. The fingers grow perpendicular to the step, along one of the $\langle 1\bar{1}0 \rangle$ close-packed directions, as observed experimentally. As an example of the pattern which can be produced at a temperature of 200 K with the set of barriers quoted in Table 5.2, Fig. 7.2 shows a series of images taken during a typical run, where a scan rate of 500 Hz and an atom displacement of 100 times the nearest neighbour distance were chosen. This pattern looks quite similar to that observed in the experiments at room temperature. There is, therefore, a mismatch between the experiments and the simulations, which is a clear indication that the atomistic calculations have underestimated the barrier heights. The reasons
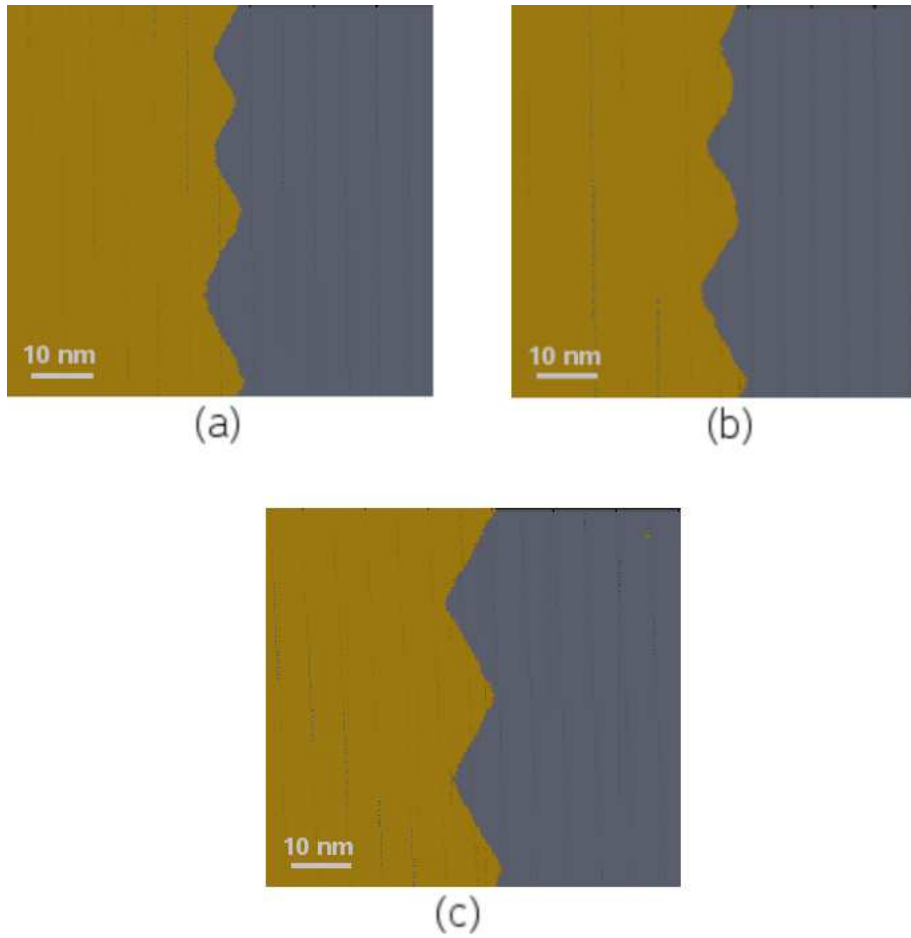
Figure 7.1: Series of images taken during a KMC simulation at 300 K. (a) System configuration after 2×10^8 iterations, system time 4 s; (b) configuration after 4×10^8 iterations, system time 7 s; (c) configuration after 10^9 iterations, system time 18 s.

for this are twofold. It is known that semiempirical potentials tend to underestimate the surface free energy [41], thus providing too low values for transition state energies. Furthermore, previous calculations have shown that the self-diffusion on the Au(111) surface is hindered when the presence of the $22 \times \sqrt{3}$ reconstruction is taken into account [17, 143].

Since my atomistic calculations have been carried out on the unreconstructed Au(111) surface, the calculated barrier heights are likely to be too low. Therefore, all the barriers listed in Table 5.2 have been multiplied by the same factor of 1.5. This value matches well the factor of 1.3 found by Boisvert and Lewis [17] for the
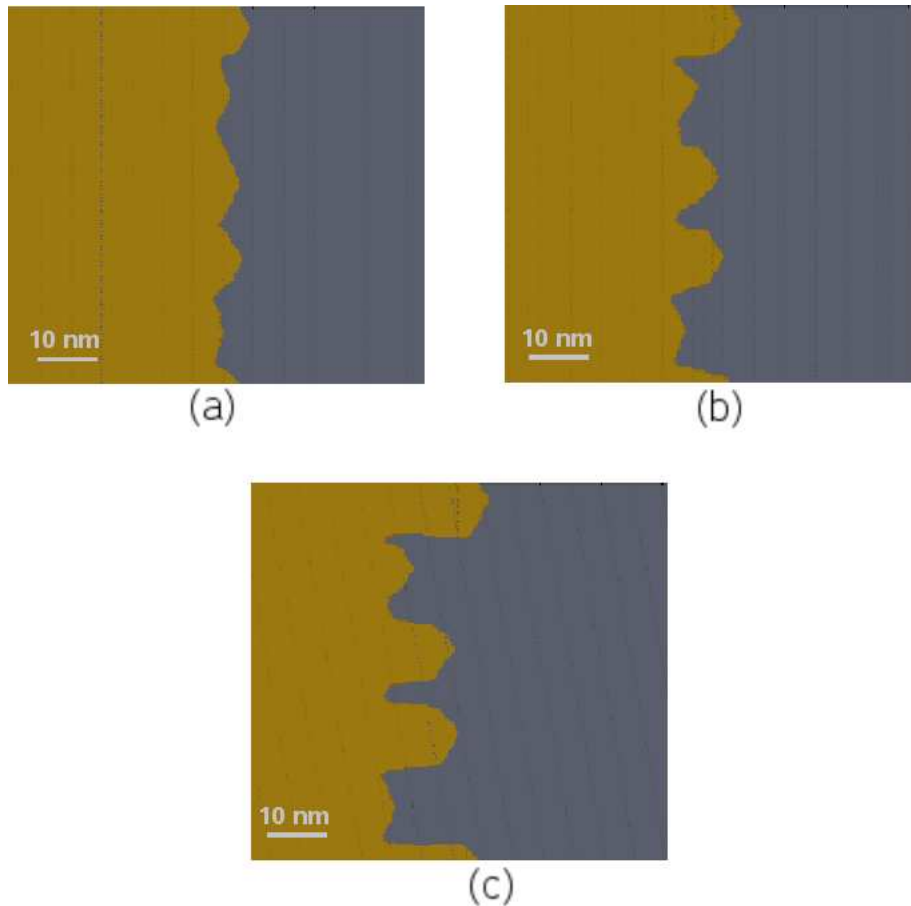
Figure 7.2: Series of images taken during a KMC simulation at 200 K. (a) System configuration after 10^9 iterations, system time 24.3 s; (b) configuration after 1.2×10^9 iterations, system time 29.7 s; (c) configuration after 1.4×10^9 iterations, system time 35.4 s.

ratio of the diffusion activation energy on the reconstructed to that on the bulk-like Au(111) surface. A new series of KMC calculations have been performed using the set of rescaled barriers. With these new values, the simulation produces, at the correct temperature of 300 K, the same finger pattern as that previously obtained using the calculated activation energies at 200 K. An example of the results typically observed at 300 K, using a scan rate of 500 Hz is displayed in Fig. 7.3.

A statistical analysis of the finger width, both in the case of the simulated and the experimental pattern, has been undertaken. It has been found that the distribution is in both cases close to normal, with almost the same amplitude. However, one can notice
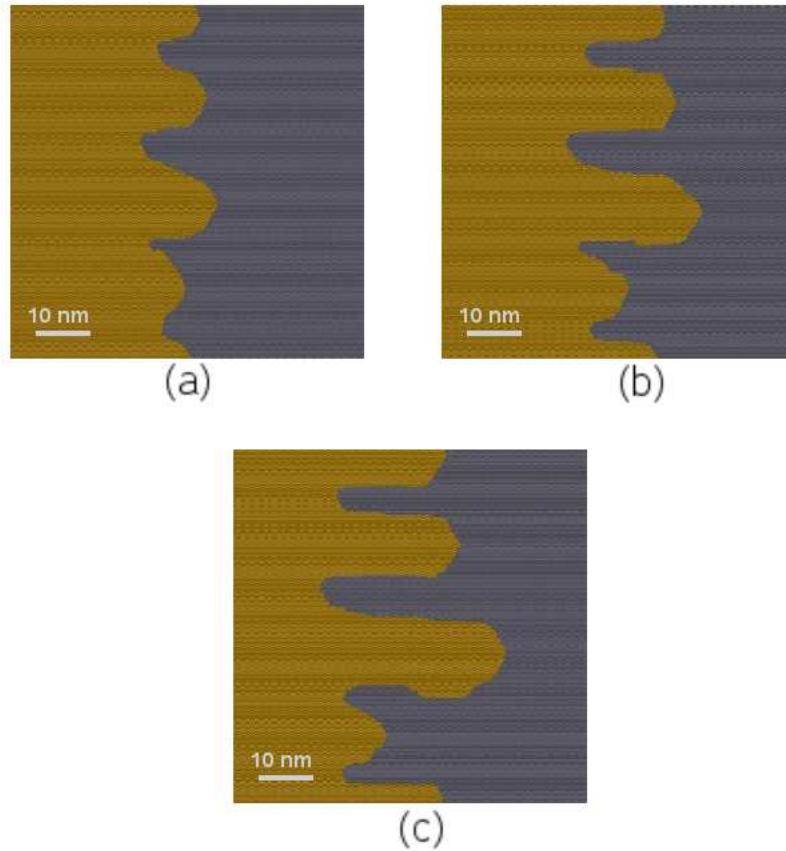
Figure 7.3:   A typical result obtained at 300 K with the set of barriers quoted in Table 5.2 multiplied by a factor of 1.5. (a) System configuration after 1.2×10^9 iterations, system time 29.8 s; (b) configuration after 1.5×10^9 iterations, system time 38.8 s; (c) configuration after 1.7×10^9 KMC iterations, system time 46.2 s.

a clear difference between the two histograms in Fig. 7.4, in that the whole thickness distribution of the simulated fingers is shifted to higher width by approximately a factor of 2 with respect to the distribution of the experimental fingers. Therefore, the simulated pattern, though qualitatively similar, cannot reproduce the experimental data faithfully.

By registering the frequency of occurrence of each diffusion process class, it has been noticed that the overwhelming majority of events are diffusions of free adatoms on the lower terrace $(0 \rightarrow 0)$, which contribute 99.89% of the total diffusion processes.
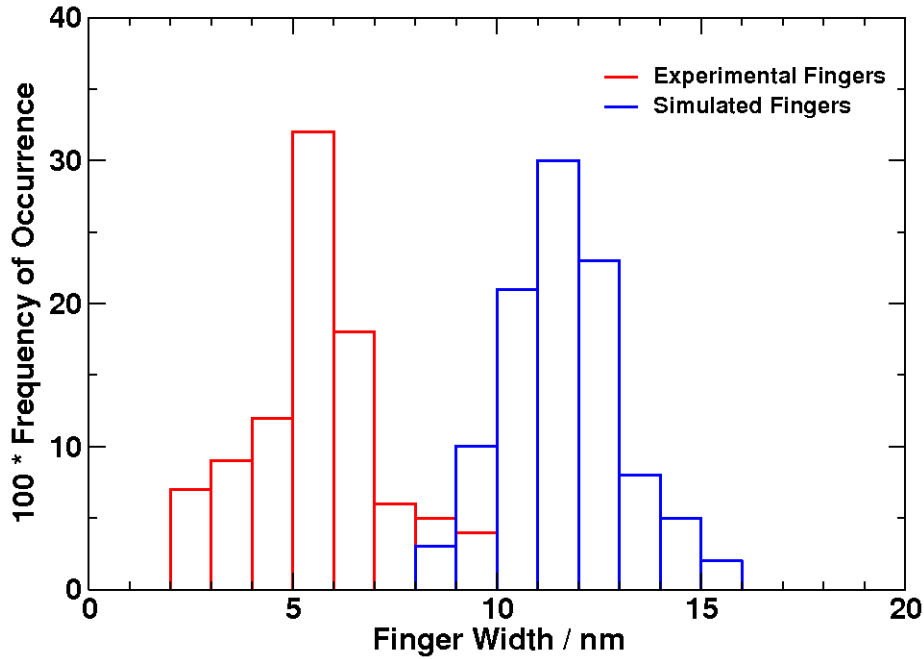
Figure 7.4: Width distribution of the finger pattern obtained experimentally (red) and in our calculations (blue).

Step edge diffusion $(2 \rightarrow 2)$ is the second most frequent process, with an occurrence of $8.9 \times 10^{-2}\%$, followed by adatom attach to a step kink $(2 \rightarrow 3)$, $7 \times 10^{-3}\%$. Finally, one observes that the number of atoms that attach to a step edge from the lower terrace (process $0 \rightarrow 2$) is almost the same as the number of atoms extracted by the tip from the edge. These observations allow one to understand the adatom kinetics on the surface. Once the adatoms are released by the tip onto the terrace, they perform a random walk across the surface until the edge of the upper terrace is approached. When attached to a close-packed step, the adatoms are allowed to migrate along the edge, but as soon as they come across a kink, they are trapped by the step defect.

In order to study the effect of diffusion on the pattern formation, the values of those barriers which are responsible for the most influential diffusion processes affecting finger shape have been selectively modified. The relationship between adatom diffusion and the formation of adatom islands on surfaces is by now a well established field of study. Island formation during homoepitaxial growth has been studied on close-

packed surfaces such as Pt(111) [20, 152, 153, 158], Al(111) [155] and Ag(111) [160]. Both experimental surface characterisation techniques and atomistic modelling have been employed to cast light on the atomic processes which are most likely to influence the wide range of patterns observed during epitaxial metal growth. Among these are diffusion across a bare terrace, along a step edge and around a corner or a kink on a close-packed step.
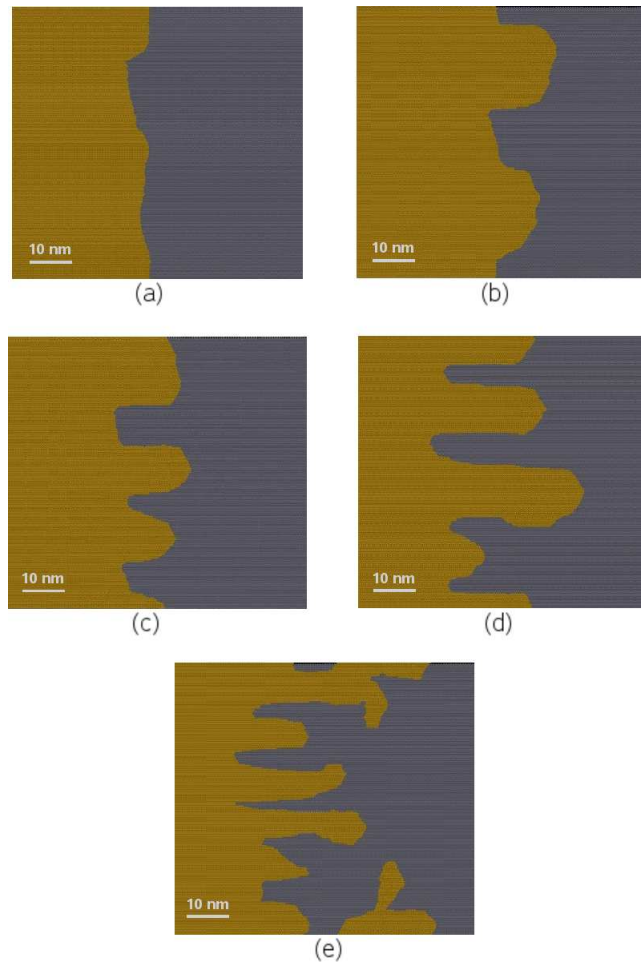
Figure 7.5:   Different patterns obtained by modifying the barrier E_{22}. (a) $E_{22} = 0.28$ eV. Configuration after 2×10^9 iterations, system time 47.3 s. (b) $E_{22} = 0.36$ eV. Configuration after 2×10^9 iterations, system time 49.6 s. (c) $E_{22} = 0.40$ eV. Configuration after 1.8×10^9 iterations, system time 45.3 s. (d) $E_{22} = 0.43$ eV. Configuration after 1.7×10^9 iterations, system time $= 46.2$ s. (e) $E_{22} = 0.50$ eV. Configuration after 1.4×10^9 iterations, system time 45.0 s.

We have started with the study of the influence of edge diffusion on finger growth.

In Fig. 7.5, the results obtained for different values of E_{22} are compared, while in the graph in Fig. 7.6 the frequency of occurrence of some particularly significant processes is plotted as a function of E_{22}. If the step edge diffusion is too fast (E_{22} is too low), no instability can set in, since the step has time to rearrange to a lower energy configuration. As E_{22} is increased, the finger pattern starts to appear. The steady decrease in the occurrence of edge diffusions as the barrier height increases is accompanied by an equally steady increase in the occurrence of other processes, such as corner rounding and detachment from and attachment to a kink, which at very low E_{22} occur in much lower proportion. The instability manifests itself as thick bulges along the step for low values of E_{22}. The fingers get thinner and thinner as edge diffusion gets slower. Finally, when the barrier responsible for step diffusion is too high, bifurcations, giving rise to secondary branches, are observed due to the tendency displayed by the fingers to develop bulges on top. This is reflected in the high frequency of all processes other than edge diffusion.

We subsequently turned our attention to diffusion processes at or around corners. The barrier E_{21} has proven to be particularly influential for the pattern appearance, as can be seen in Fig. 7.7. Lowering E_{21} leads to an enhancement of corner diffusions ($1 \rightarrow 2$ and $2 \rightarrow 1$), resulting in the formation of thick, closely spaced fingers. On the other hand, by making the corner diffusion more difficult, a more rugged, irregular pattern is induced. The formation of islands is observed in this case, along with rough profile fingers whose width is much less than in the previous case.

The influence of the kinks on the step rearrangement has also been studied. One process we have identified as particularly important is adatom release by a kink followed by migration of the adatom to an edge site ($3 \rightarrow 2$). We have said before that kinks act as *traps* for adatoms diffusing on step edges. Once trapped in kink sites, the adatoms are released back to the step with low probability and stand almost no chance of reaching the corner site adjacent to the kink or a terrace site. If E_{32} is lowered, a

Figure 7.6:   Frequency of occurrence of some particularly significant diffusion processes plotted as a function of E_{22}. For clarity of display, all curves have been rescaled by a factor of 100, except that for the $2 \rightarrow 2$ process.

tendency of the fingers to bend laterally and to develop bifurcations is observed (see Fig. 7.8 (a) and (b)). On the other hand, when the step adatom release by kinks is made slower, the fingers tend to grow along the same close-packed direction, thus resulting in a well aligned, parallel pattern (see Fig. 7.8 (c) and (d)). In other words, the *trapping power* of kinks affects the directionality of the finger growth. A too high adatom release rate from a kink to an edge site hinders the finger growth by causing the fingers to bend laterally. If, instead, kink sites are traps which the adatoms can barely leave, the growth of straight fingers is favoured. We also point out that the fingers in Fig. 7.8 (c) and (d) are thinner and more widely spaced than those in Fig. 7.7 (a) and (b). The decreased width is most probably due to the dramatically reduced amount of adatom corner crossing (processes $1 \rightarrow 2$ and $2 \rightarrow 1$) with respect to the case in Fig. 7.7 (a) and (b), where this type of processes occurs an order of magnitude more frequently.
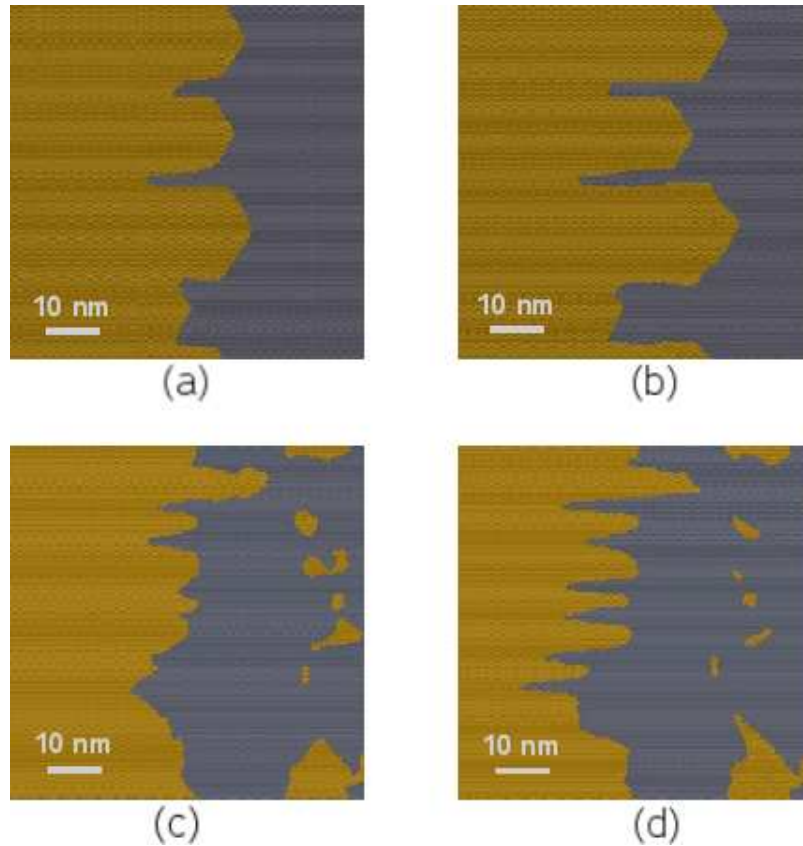
Figure 7.7:   Patterns obtained by altering the value of E_{21}. (a) and (b) System configuration during a session of calculations with $E_{21} = 0.38$ eV, after 1.4×10^9 iterations (system time = 35.4 s) and 1.8×10^9 iterations (system time = 47.2 s), respectively. (c) and (d) System configuration during a session of calculations with $E_{21} = 0.59$ eV, after 1.2×10^9 iterations (system time = 47.7 s) and 1.3×10^9 iterations (system time = 67.5 s), respectively.

Finally, the effect of terrace diffusion on the finger pattern has been investigated. The effects of the alteration of E_{00} are dramatic, as shown in Fig. 7.9. Generally speaking, one notices that by increasing the height of the barrier for terrace diffusion, the pattern produced displays thinner and better aligned fingers. This qualitative observation has been confirmed by a quantitative statistical analysis of the width distribution obtained for each value of E_{00}. In Fig. 7.10 we have plotted the mean value of each distribution as a function of E_{00}, the error bars representing the standard deviation of the mean. The mean width decreases steadily as the barrier increases. For values of E_{00} greater than 0.35 eV, a plateau is reached. This trend is similar to that which
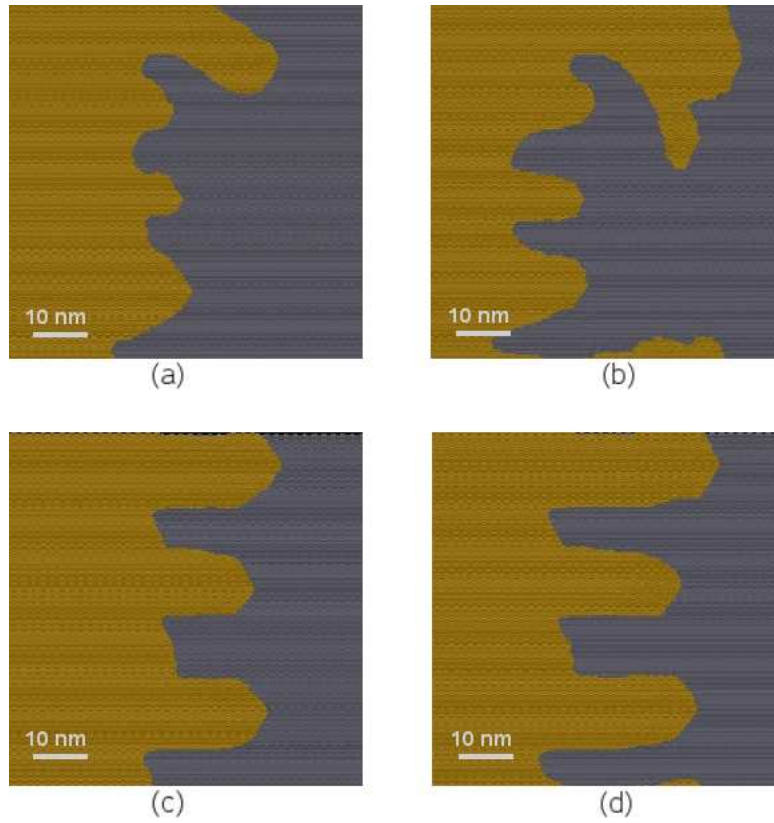
Figure 7.8:   Patterns obtained by altering the value of E_{32}. (a) and (b) System configuration during a session of calculations with $E_{32} = 0.60$ eV, after 1.5×10^9 iterations (system time = 35.4 s) and 1.9×10^9 iterations (system time = 58.2 s), respectively. (c) and (d) System configurations during a session of calculations with $E_{32} = 0.67$ eV, after 1.6×10^9 iterations (system time = 41.8 s) and 1.8×10^9 iterations (system time = 49.2 s), respectively.

we have found when comparing the most relevant diffusion processes. For E_{00} in the range $0.20 - 0.35$ eV, the diffusions on the bare surface undergo a steep decrease in favour of step, corner and kink diffusions, whose occurrence increases just as rapidly. This increase seems to slow down for E_{00} above 0.35 eV.

The hindering of terrace diffusion (by increasing E_{00}), obviously leads to an increase in probability of the other processes. In particular, corner diffusion ($1 \rightarrow 2$ and $2 \rightarrow 1$) undergoes the sharpest rise as the $0 \rightarrow 0$ barrier is increased. But also corner and kink diffusions are faster when terrace diffusion slows down, which causes the step edge to rearrange more swiftly. This, together with the increasing density of isolated adatoms

on the lower terrace, brings the system out of equilibrium to a greater extent, which, in turn, leads to the formation of thinner fingers. We note that the pattern obtained by fine-tuning E_{00} bears a striking resemblance (same shape and thickness) to the experimental data shown in Fig. 7.12.
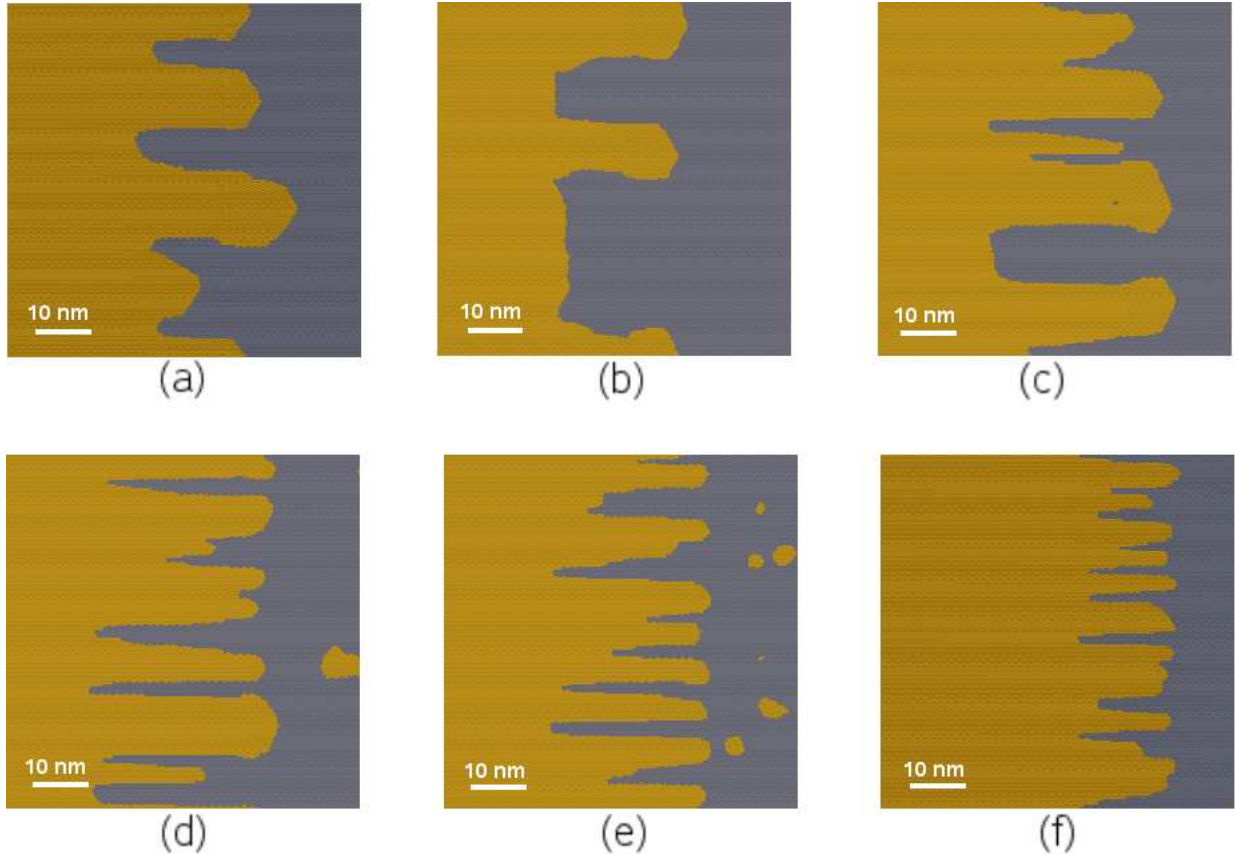
Figure 7.9: Patterns obtained by altering the value of E_{00}. (a) $E_{00} = 0.15$ eV. Configuration after 1.6×10^9 iterations, system time 42.2 s. (b) $E_{00} = 0.25$ eV. Configuration after 7×10^8 iterations, system time 27.0 s. (c) $E_{00} = 0.30$ eV. Configuration after 4×10^8 iterations, system time 46.4 s. (d) $E_{00} = 0.35$ eV. Configuration after 1.4×10^8 iterations, system time 56.2 s. (e) $E_{00} = 0.40$ eV. Configuration after 10^8 iterations, system time 55.6 s. (f) $E_{00} = 0.45$ eV. Configuration after 10^8 iterations, system time 41.3 s.

In conclusion, a realistic model of diffusion on the Au(111) surface in the presence of a step edge and an STM induced electric field has been set up. This is an example of a system which is brought out of equilibrium by a perturbation, which in this case is represented by the STM tip. Experimentally, the step proves to be unstable under
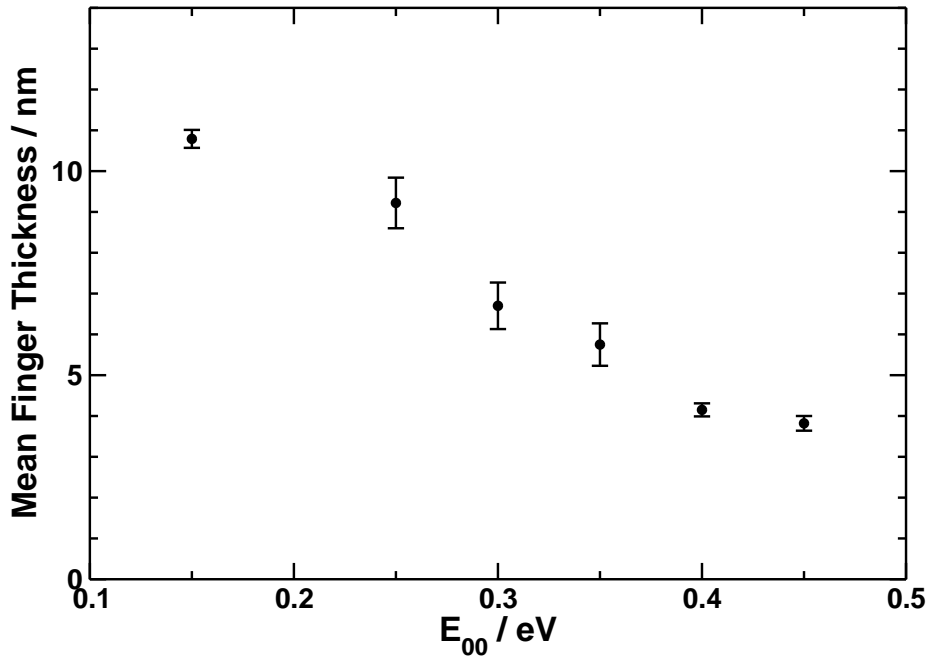
Figure 7.10:   Mean finger thickness as a function of E_{00}.

the effect of such a perturbation. This instability has been reproduced to an excellent degree of accuracy, both from a qualitative and a quantitative point of view. My atomistic calculations of diffusion barrier, together with the KMC algorithm I have set up, have indicated that the pattern resulting from the instability is a delicate interplay between all of the processes considered in the model. I have managed to relate the pattern appearance to some important processes such as diffusion on the bare surface, along step edges, around corners and in proximity to kinks.

Furthermore, it has been found that the kinetic instability driving gold nanofinger growth is not caused directly by the substrate reconstruction, since the instability manifests itself also when reconstruction is not taken into account. However, the results found in the present work indicate that reconstruction is important for determining the actual finger shape and thickness. In fact, the reconstruction induces an increase of diffusion barriers [143] for isolated adatoms. My simulations have explicitly shown that this increase causes the growth of thinner and better aligned fingers. For a barrier
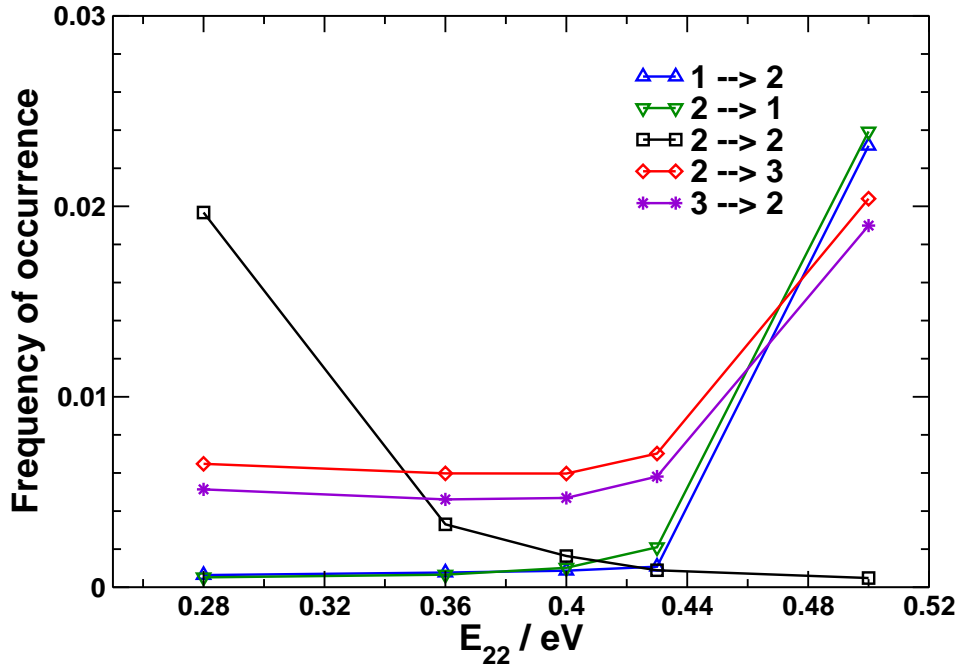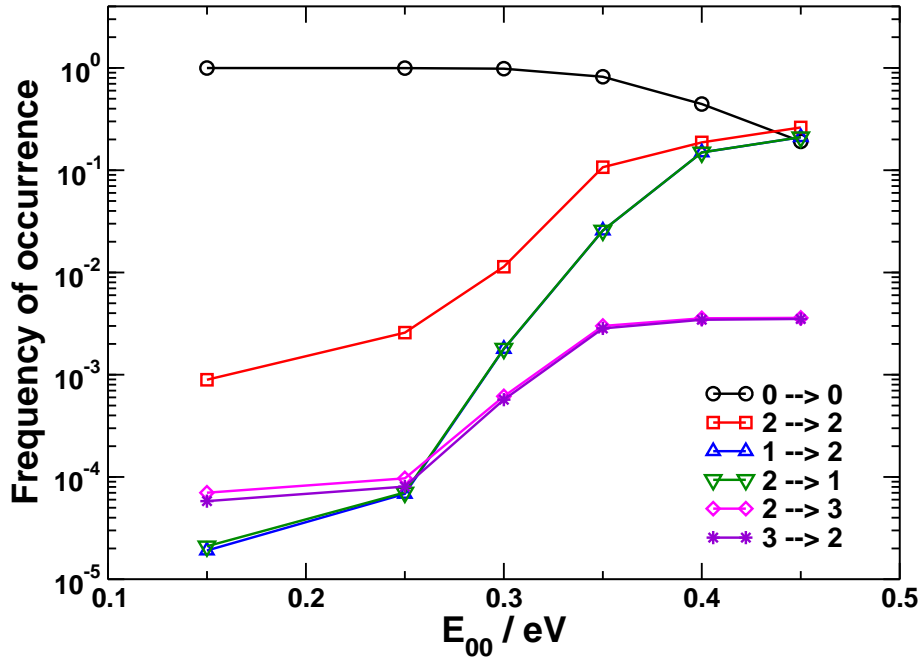
Figure 7.11:   Frequency of occurrence of some particularly significant diffusion processes plotted as a function of E_{00}.

of 0.35 eV (a barrier which is too high for diffusion on unreconstructed Au(111)), simulated fingers perfectly match the experimental results.

7.3   Improved modelling of the STM tip effect

So far, no attempt has been made to model the effect of the STM tip on the system realistically. The experimental evidence points to a picture in which some step edge atoms are detached by means of the STM tip and are released to the lower terrace, whence they diffuse back towards the step, as discussed in Sect. 4.4. However, the detachment mechanism cannot be determined by the experiments. In the present section, an account is given of that part of my work aimed at introducing the STM induced atomic manipulation into the atomistic model.
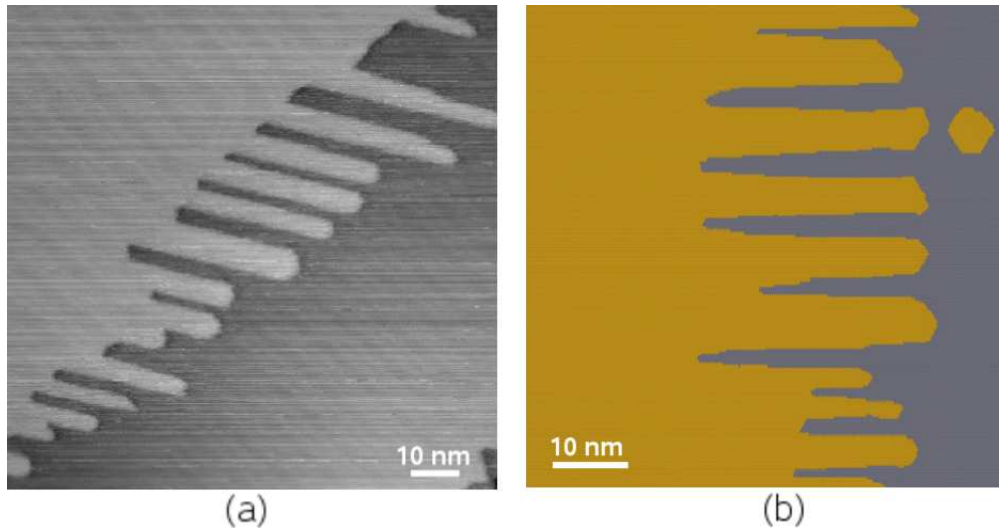
Figure 7.12:   (a) Experimental STM scan taken after manipulation of a step edge on Au(111). Bias Voltage = 1 V, Tunneling Current = 0.2 nA (courtesy of Dr. F. Yin). (b) Simulated pattern with $E_{00} = 0.35$ eV. System configuration after 10^8 iterations, system time 56.7 s.

7.3.1   STM atomic manipulation

Since its invention, the STM has proven not only to be an invaluable imaging tool able to resolve features down to atoms on a surface, but also a revolutionary technique with which atoms and molecules can be manipulated and arranged across a surface with a degree of precision of the order of the Ångstroms. Since the pioneering work in which Don Eigler and coworkers managed to move laterally [148] and vertically [178] a single Xe atom on a Ni surface, the STM has been used in various experiments for the manipulation of an adsorbate on a metal or semiconductor substrate [179]. One of the most spectacular successes achieved by STM atomic manipulation is the *quantum corral*, obtained by Eigler's group by arranging 48 Fe atoms adsorbed on a Cu(111) surface to form a ring with a diameter of approximately 14 nm [149].

Lateral atomic manipulation is performed by exploiting different types of interactions arising between the tip and substrate atoms. Due to the strong directional bonds in semiconductors, adsorbates on semiconductor surfaces can be manipulated by using the effects of the strong electric field established in the gap between the tip apex and

the substrate [180, 181]. On the other hand, manipulation of atoms on metal surfaces relies on the forces arising from the interaction between the atoms making up the tip and the substrate. Depending on tunnelling parameters, three mechanisms have been singled out for atomic manipulation on metal surfaces: pulling, sliding and pushing. The three modes have been used in the manipulation of different adsorbates on the Cu(211) surface, a vicinal surface to the (111), in an experiment performed by Bartels and coworkers [182] in a variable temperature STM kept at a temperature of 30 K. It has been shown that a Cu adatom on Cu(211) can be moved in pulling mode by approaching the tip to the sample at such a distance that a tunnelling resistance of 400 kΩ is established. In the pulling mode, the adparticle jumps between neighbouring adsorption sites following the tip movement with a delay which depends on the tip-sample distance. Pb atoms on Cu(211) are also manipulated via atom pulling when the tunneling resistance is of 120 kΩ. But when the tunnelling resistance is reduced down to around 40 kΩ, sliding manipulation mode is observed, where the adsorbate follows the tip continously during its motion. Finally, pushing mode is observed when manipulating CO molecules on Cu(211) at a tunnelling resistance between $\simeq 300$ and $\simeq 600$ kΩ. In this mode the tip, when lying on the molecule, causes it to jump to a neighbouring adsorption site away from the tip position. It is clear that the pulling and sliding modes are determined by an attractive interaction between the tip atoms and the adsorbate: weaker in the pulling mode and stronger in the sliding mode. On the other hand, the pushing mode is made possible by a repulsive interaction exerted by the tip atoms on the adsorbed species.

Experimental evidence is also available for lateral manipulation of atoms embedded in structures such as step edges and kinks. Extraction of atoms packed in close packed edges of a Cu(211) surface has been achieved at a temperature between 30 and 40 K, thus creating a vacancy in the step and a free adatom on the lower lying terrace [183]. In the same work, other manipulation processes have been performed such as the lateral

manipulation of an adatom parallel and perpendicular to a step, the extraction of an atom out of the step in the step-up direction, and the filling of a step edge vacancy by moving a nearby atom lying on a kink site. This shows that it is possible to manipulate substrate atoms located in fivefold, sixfold, and sevenfold coordinated sites. In general the force needed to move atoms with different coordinations is different, with higher coordinated atoms requiring higher forces, and, therefore, lower tunnelling resistances. The range of tunnelling resistance used in the experiment spans from $\simeq 70 \, \text{k}\Omega$, for the extraction of one atom out of the step edge, to $\simeq 700 \, \text{k}\Omega$, for the displacement of an atom along a step edge, depending on the tip. For all the processes induced by means of the STM tip in their investigations, the authors point out that only attractive forces between the substrate atom and the tip have been used. The evidences supporting this claim are manyfold. Firstly, the relatively high tunnelling resistances used in the experiments are significantly above the resistance for point contact, which excludes the close proximity of the tip to the substrate required for manipulation in pushing mode. Secondly, no transfer of atoms has been observed, either between the substrate and the tip, or vice versa. Finally, it is observed that moving atoms across a step edge would not be possible using repulsive forces. Because of these reasons, one can conclude that the processes induced by the STM tip in this work are operated in one of the two attractive manipulation modes, i.e. pulling and sliding.

Evidence of atom extraction by an STM tip is also provided by a series of experiments where a step edge on a metal surface is observed to be modified after scanning the surface under conditions of enhanced electric field. Li and coworkers [184] have performed an experiment where, at a temperature of 295 K, a straight step can be modified by inducing a protrusion on the edge if the tunneling resistance is reduced to $\simeq 400 \, \text{k}\Omega$ from the value of $\simeq 4 \, \text{G}\Omega$ used for imaging. The structure thus formed has been recognised to be a nonequilibrium state of the step, in that on a time span of 20 min the artificially modified step profile decays back into the original straight

configuration. The suggested scenario for the formation of the protrusion is that the STM tip is able to extract a few atoms from the step and to pull them on the lower terrace. Subsequently, diffusing atoms can condense between the adatoms fixed by the tip and the atoms on the edge. This process is prompted by the attractive force exerted by the tip on the diffusing adatoms.

A similar scenario is proposed by Mugele and collaborators in their work concerning the modification of a monoatomic straight step on an Ag(111) surface [185]. The whole experiment is carried out at room temperature and, following the same procedure as in Ref. [184], a close packed step was scanned repeatedly along the same line perpendicular to the step direction. It has been found that the STM tip perturbs the system to an extent which depends on the tip-sample distance, i.e. on the tunneling resistance. In turn, the effect of the tip-induced perturbation depends dramatically on the apex configuration of the particular tip used. The range of tunneling resistances used spans from $\simeq 100$ MΩ, to $\simeq 10$ GΩ. At all tunneling gaps, the authors have observed significant tip-induced fluctuations of the step edge. The fluctuations are more pronounced when the tunneling resistance is above $\simeq 1$ MΩ. Analogously to Ref. [184], the scenario suggested to give account of the phenomenon is one where some adatoms are detached from the step edge under the effect of the STM tip. These detached adatoms diffuse across the lower terrace or along the step edge, until they stick on a step kink. The mechanism responsible for step edge atom detachment is ascribed to a short-range atomic interaction between the tip atoms and the topmost atoms in the substrate. Possible effects of the STM electric field on atomic manipulation are ruled out, since a reduction of electric field seems to enhance the atom extraction out of the step edge, rather than quenching it. Furthermore, no effect of the polarity of the bias voltage has been observed in the experiment. At least for static dipole moments, one would expect a polarity dependence.

Atomic manipulation on surfaces can also be performed vertically. By reducing the

distance between the tip and the substrate, surface modification is induced as soon as the two electrodes experience a *jump to contact.* For example, three dimensional Au clusters on Au surfaces have been produced in this way in a series of studies performed at room temperature by Pascual and collaborators [186, 187]. The structures thus created were explained in terms of biased surface diffusion caused by the STM electric field, analogously to the case of Cs molecules on GaAs studied by Withman et al. [180]. The authors argument that, due to their non negligible atom polarisability, atoms adsorbed on a surface are affected by the inhomogeneous electric field established between the STM tip and the atom. The electric field gradient is expected to induce a force on the diffusing adatom, which is directed towards the tip projection onto the surface. This interpretation seems to disagree with that given in other similar experiments where jump to contact regime is studied both experimentally and by means of simulations based on semiempirical potentials [188, 189]. The focus is here on the adhesive atomic forces between tip and substrate, which are responsible for the downwards relaxation of the tip atoms, and for the upwards relaxation of the substrate atoms below the tip. As a result of this relaxation, the actual separation between tip and surface is smaller than in the case of a rigid tip above a rigid substrate.

Jump to contact has systemically been investigated by Limot and collaborators [190] on Cu(111) and Ag(111) at cryogenic temperatures. The data experimentally obtained match well with ab-initio calculations previously performed [191], where atom relaxation of both tip and substrate atoms had been demonstrated for close proximity of the two electrodes. Both the experiment and ab-initio calculations also show that in the jump to contact regime the adhesion of the tip apex to the tip structure is weakened to such an extent that the tip vertex atom can be transferred from the tip onto the surface. No atom can be transferred to the substrate if an adatom is present below the tip before the jump to contact approach.

Simulation studies have tried to explain the mechanism underlying the lateral ma-

nipulation performed by Li et al. on Ag(111) [184] and by Rieder and coworkers on Cu(211) [182, 183]. Kürpick and coworkers have performed a series of semiempirical calculations on a system made of an adatom lying on a step edge of a Cu(111) and of a Cu(110) surface in the presence of an STM tip made of Cu [23, 192]. The tip is located above the step edge at a certain distance away from the adatom (see Fig. 7.13). Barriers to adatom diffusion along the step edge, for both the motion towards and away from the tip are calculated for several tip-adatom distances. The result of the calculations is that the barrier for diffusion towards the adatom decreases and the barrier for diffusion in the opposite direction increases. The amount of variation of the barriers is different depending on the tip nature (e.g. the results change for a static compared to a relaxed tip, and for a sharp compared to a blunt tip), and on the tip-surface vertical separation. The trend, though, is similar for all types of tip examined and for all tip heights, both on Cu(111) and Cu(110) (see Fig. 7.14). The general conclusion which can be drawn from the calculations is that the the effect of an STM tip is to lower the diffusion barriers for motion towards the tip, and to increase those in the opposite direction. These changes are explained in terms of coordination effects between surface and tip atoms and, therefore, as a result of a modification of the potential energy surface experienced by the diffusing adatom due to the interaction between tip and substrate atoms.

7.3.2   Modelling the STM tip

No systematic study has been attempted to investigate the actual atom detachment mechanism in the nanofinger growth. However, a guess has been given on the basis of both previous theoretical and experimental work. As the experiments show, the STM tip must be responsible for the atom detachment out of the step edge. The extraction can either be due to the effect of the intense electric field as suggested by the authors of the nanofinger growth experiment [14, 101], or to the action of interatomic attractive forces established between the tip and the substrate in close proximity to each other, as
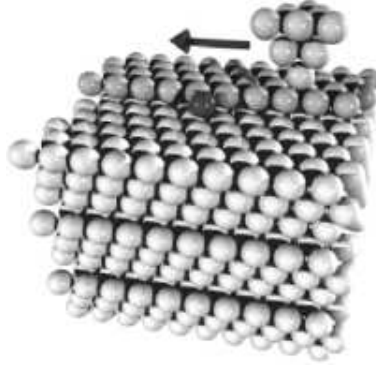
Figure 7.13:   Sphere model of the simulation unit cell used in Ref. [23] for the calculation of the diffusion barrier along a step edge on a Cu(111) surface in the presence of an STM tip. The distance x is defined as the horizontal separation between the tip apex and the adatom on the step edge (from Ref. [23]).

proposed in the experimental work of Mugele and colleagues [185]. In the present work, the interest is focused on the net result of the interaction between tip and substrate, which, following the semiempirical calculations carried out by Kürpick [23, 192], can be thought of as a local decrease of activation barriers to adatom diffusion towards the tip apex.

In order to simulate the effect of the STM tip on the nanofinger growth, the KMC programme described in Sect. 7.1 has been modified by introducing a circular field on the surface lying below the tip apex and wherein the diffusion is enhanced with respect to the unperturbed surface. It has been assumed that the STM tip causes a perturbation of the energy landscape experienced by an adatom, which varies linearly with the distance r between the adatom position and the tip apex projection in the following way:

$$V(r) = \begin{cases} V_0 \left(\frac{r}{r_0} - 1 \right) & \text{if} \;\; r \leq r_0 \\ 0 & \text{if} \;\; r > r_0 \; ; \end{cases} \tag{7.1}$$

where V_0 and r_0 are the intensity right below the tip, and the radius of the circular field, respectively.

Let E_{ij} be the energy barrier experienced by an adatom during diffusion from an i-fold to a j-fold coordinated adsorption site in the absence of electric field. Let r_i and
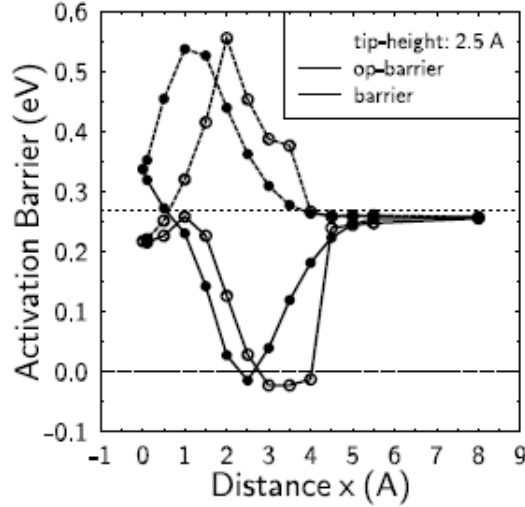
Figure 7.14: Calculated barriers for diffusion for motion towards (continuous line) and away from (dotted line) the tip as a function of the tip-adatom horizontal separation x. The tip is modelled as a 10 Cu atoms stacked in a fcc(111) pyramidlike fashion. The vertical separation between the tip apex and the surface (tip height) is 2.5 Å. Two types of tip are considered: a rigid tip where the tip atoms are fixed in their original position (filled circles), and a non-static tip where atoms are allowed to relax (open circles). The dotted line indicates the barrier of 0.27 eV calculated in the absence of the tip (from Ref. [23]).

r_j be the distance of the initial and final site, respectively, from the projection of the tip apex on the surface. In the presence of the electric field the barrier to diffusion E'_{ij} is modified as follows:

$$E'_{ij} = E_{ij} + V(r_j) - V(r_i). \tag{7.2}$$

This produces a force on the adatom parallel to the surface plane and directed towards the tip apex.

7.3.3 Results of the improved model

By using the improved version of the code described above, a series of calculations have been performed. Due to the intensive use of CPU time required by the improved version of the algorithm, it has not been possible to simulate STM scans across an extended area. However, some sessions of calculations have been successfully carried

out, where a repeated scan along the same line perpendicular to the step edge has been simulated. Experimental data registered during scanning in line-mode was also available for comparison.

A scan frequency of 5 Hz, in agreement with the experiments, has been set in the model. Furthermore, a circular force field has been assumed to be created by the STM tip on the surface, with a typical radius r_0 of $\simeq 5$ nm [180, 193]. All calculations have been performed at a temperature of 300 K, using the set of barriers listed in Table 5.2 multiplied by the same factor of 1.5 as in Sect. 7.2.

Given how the potential has been chosen, the crucial parameter is the ratio V_0/r_0 of the field intensity to the field radius. The field intensity V_0 has been modified while r_0 has been kept at the value of 5 nm. With $V_0 = 2$ eV, little or no step modification is observed (see Fig. 7.15). The effect of the STM tip starts becoming visible at $V_0 = 3$ eV (see Fig. 7.16), when elongated islands are formed made of atoms detached by the tip out of the step edge. A proper finger is formed when V_0 is increased to 5 eV (see Fig. 7.16). Upon further increasing the field intensity while keeping the other parameters unchanged, the finger width narrows down to such an extent that it becomes unstable and breaks into islands (see Fig. 7.18).

The fact that the ratio V_0/r_0 is the most influential parameter on the finger shape has been confirmed by several sessions of calculations where the two parameters V_0 and r_0 have been varied by means of a multiplication by the same factor in order to leave the ratio V_0/r_0 unchanged. It has been observed that in all cases the fingers thus obtained displayed similar characteristics while differing only in their width. In general the finger width has been observed to depend on the field radius, with larger perturbation fields producing thicker fingers.

It is observed that the actual mechanism of finger formation is here a rearrangement of step edge adatoms, rather than the detachment-diffusion-reattachment process on which the model presented in Sect. 7.1 is based. In fact if V_0 is increased while keeping
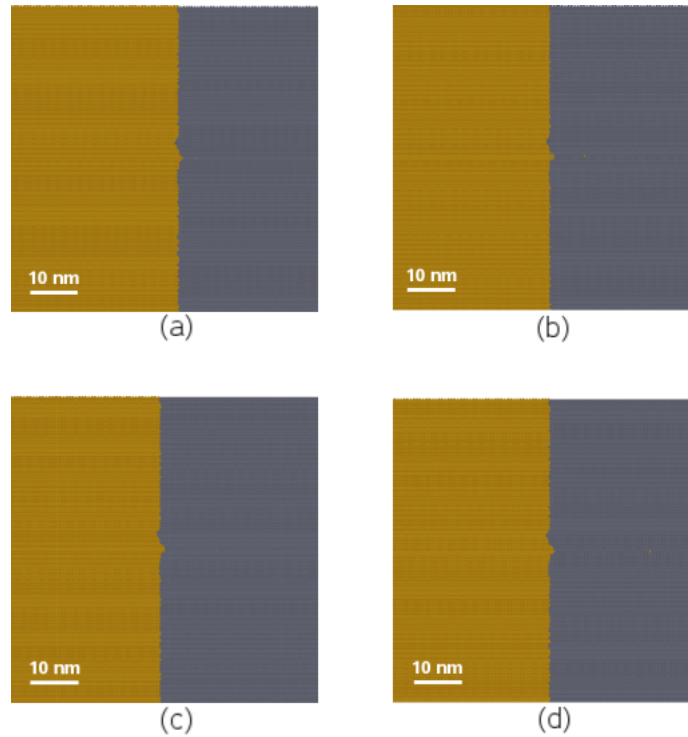
Figure 7.15:   Single line scan at a scan rate of 5 Hz; $V_0 = 2$ eV, $r_0 = 5$ nm. (a) System configuration after 10^6 iterations, system time 0.45 s; (b) configuration after 5×10^6 iterations, system time 0.46 s; (c) configuration after 10^7 iterations, system time 0.47 s; (d) configuration after 2×10^7 iterations, system time 0.49 s.

r_0 constant, one notices a dramatic monotonic decrease of diffusions on the bare terrace in favour of step edge, corner, and kink diffusion. In particular, the analysis of process frequency allows one to infer that the finger growth proceeds by extension of the step edges delimiting the finger. Since the most frequent process during finger growth is by far step edge diffusion ($2 \rightarrow 2$), a picture can be drawn in which the tip, on passing on the step edge, detaches some edge atoms on the border of the circular area where the STM induced force field is active. The detached atoms are pushed towards the centre of the force field, below the tip, where they coalesce. As the tip moves away from the step edge along the current scan line, a reorganisation of the coalesced adatoms takes place whereby the atoms tend to form arrays aligned along the close-packed direction on the surface which form the smallest angle with the scan line direction. This allows the system to relax into the local minimum energy configuration, thus causing the finger
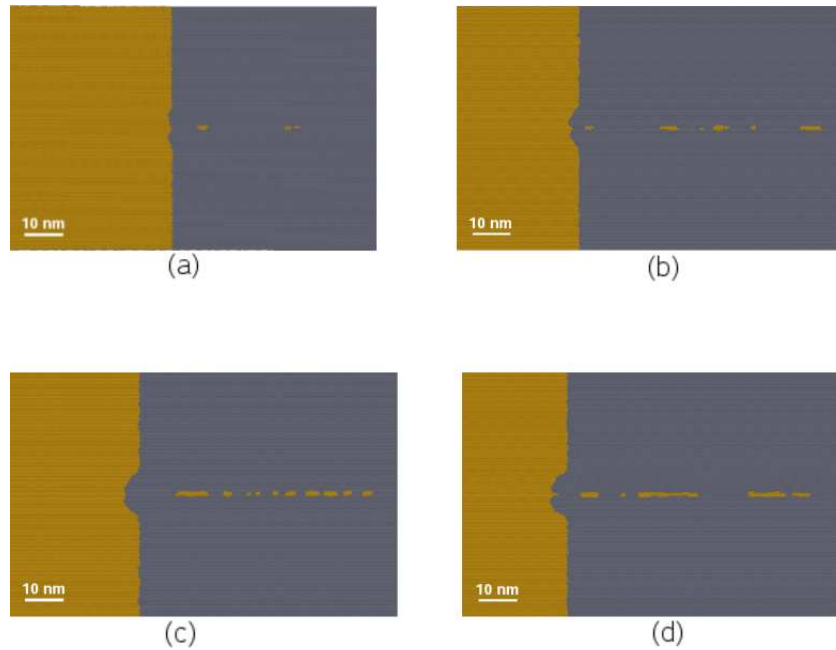
Figure 7.16:   Single line scan at a scan rate of 5 Hz; $V_0 = 3$ eV, $r_0 = 5$ nm. (a) System configuration after 10^6 iterations, system time 2.5 s; (b) configuration after 10^7 iterations, system time 18.7 s; (c) configuration after 1.5×10^7 iterations, system time 36.0 s; (d) configuration after 2×10^7 iterations, system time 47.6 s.

to form. In the course of the subsequent scans along the same line, other adatoms are detached from the step edge and deposited on the finger border at its base. From the finger base, the adatoms diffuse along the finger edge towards its top, where they are pushed by the tip in its scan away from the step. Once the adatoms reach the finger tip, they also tend to form close-packed rows thereby contributing to the finger growth.

The model outlined above seems to be realistic and provide satisfactory results. When compared to the experiments, the fingers obtained with this version of the code turn out to be resemblant to their experimental counterpart (see Fig. 7.19). However, further conclusion cannot be drawn in the absence of a thorough study of the effect of the STM tip on the surface atoms when the electric field is applied. An extension of the present work would particularly benefit from a full ab-initio study where the surface and the tip are modelled and the effects of the electric field between the two electrodes are taken into account.
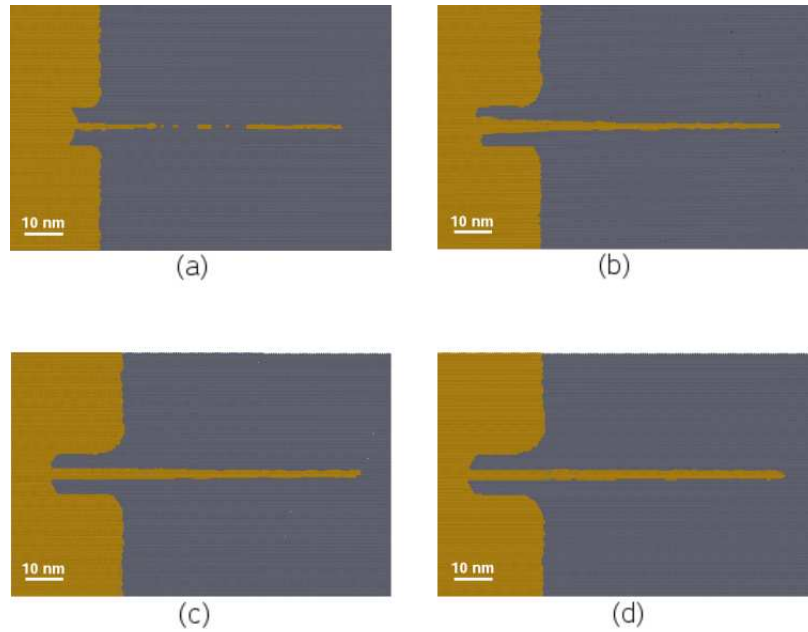
Figure 7.17: Single line scan at a scan rate of 5 Hz; $V_0 = 5$ eV, $r_0 = 5$ nm. (a) System configuration after 10^6 iterations, system time 57.3 s; (b) configuration after 6×10^6 iterations, system time 128.5 s; (c) configuration after 10^7 iterations, system time 1042.8 s; (d) configuration after 1.5×10^7 iterations, system time 1682.6 s.
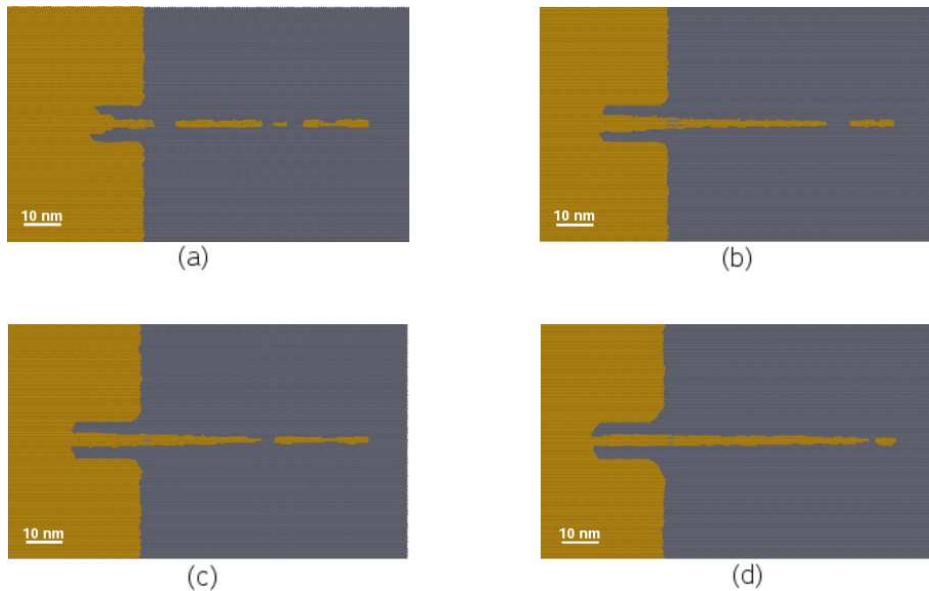
Figure 7.18: Single line scan at a scan rate of 5 Hz; $V_0 = 10$ eV, $r_0 = 5$ nm. (a) System configuration after 2×10^6 iterations, system time 29.3 s; (b) configuration after 4×10^6 iterations, system time 94.6 s; (c) configuration after 6×10^6 iterations, system time 178.4 s; (d) configuration after 1.5×10^7 iterations, system time 783.4 s.
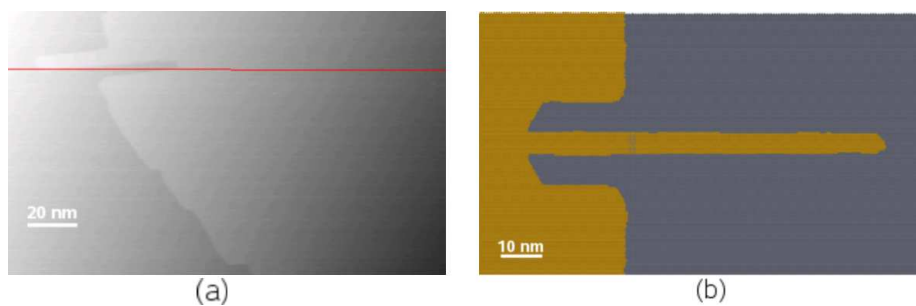
Figure 7.19:   Comparison between fingers obtained in line mode in a real experiment and in a simulation. (a) STM image of a step edge on Au(111) after manipulation along the line marked in red. (b) Simulation of line scan on Au(111) ($V_0 = 10$ eV, $r_0 = 10$ nm). Configuration after 6×10^6 iterations, system time 506.8 s.

Chapter 8

Conclusions

In this thesis some gold nanostructures have been studied within the framework of the semiempirical many-body Gupta potential. The global optimisation of small gold clusters revealed that the preferred structural motif in the size between 53 and 80 is the Marks decahedron. This motif is a compromise between the icosahedral motif, which minimises the surface area for a given volume but is a strongly strained structure, and pseudo-crystalline fcc-based structures such as the truncated octahedron, which minimise the internal stress but which are characterised by a larger ratio of surface area to cluster volume. In contrast with other noble metals, whose preferred structural motif for cluster sizes between $\simeq 50$ and $\simeq 100$ is the icosahedron, gold clusters are more stable in the decahedral motif. This is due to the sticky short-ranged nature of the gold potential which makes highly strained structures such as the icosahedral motif unfavourable.

The surface energy contribution to the cluster binding energy has subsequently been extracted from the data obtained from the global optimisations by using a simple phenomenological model of the cluster energy. The surface energy thus calculated turned out to be much lower than the experimental value. These calculations prove that the Gupta potential, as has observed for many other semiempirical potentials, displays a tendency to seriously underestimate the surface energy.

The finger pattern arising as an effect of an STM induced perturbation of a step edge

on Au(111) and Ag(111) has also been studied. The phenomenon has been identified as a kinetic instability prompted by the detachment of edge adatoms due to the STM tip. A simple lattice gas model including only nearest neighbouring interactions has confirmed this scenario. Simulations of the system kinetics, based on a Kinetic Monte Carlo algorithm, have been performed and have shown that the step edge is unstable under the effect of the STM tip. A fingering instability has been observed in the simulations which resembles fairly well the pattern obtained on Ag(111) but differs from that on Au(111). The initial simple model has therefore been improved by considering more processes in the system kinetics.

The diffusion kinetics of adatoms in proximity to step edges on Au(111) has been investigated by calculating the activation energies for all processes of interest. A conclusion which has been drawn from this series of calculations is that surface defects, such as step edges, corners and kinks tend to trap adatoms diffusing on the bare surface almost at the same rate, regardless of the particular type of defect. Once trapped in the defect, the adatom has a low probability of escaping. The kinetics of trapping, however, is not significantly faster than that of diffusion on the bare terrace, which indicates a limited range wherein the defect is effective as a trap for the adatom. This is again due to the short-range character of atomic interactions in gold.

The calculated set of activation energies have been used as an input to the improved version of the Kinetic Monte Carlo algorithm. Simulations performed at room temperature suggest that the calculated diffusion barriers have been underestimated by the Gupta potential, which is consistent with the previously mentioned conclusion that semiempirical potentials, including the Gupta potential, tend to underestimate surface energies. Therefore, all barriers have been rescaled by the same factor and a similar finger pattern to the experimental one has been obtained at room temperature. Closer quantitative resemblance can be reached by varying the activation barriers of some particularly relevant processes, such as step, corner and kink diffusion. In par-

ticular, it has been found that the finger width can be finely tuned simply by varying the height of the barrier for diffusion on the bare surface.

Finally, the effect of the STM tip on the surface has been introduced explicitly into the model by assuming an area of enhanced diffusion on the surface below the tip apex. This is the most realistic way attempted so far of introducing the effect of an STM tip into an atomistic model. The algorithm has been tested by simulating a single line scan on a step edge of Au(111) and it has produced satisfactory results.

The present work can be extended in several directions. Ab-initio methods can be used to study surface diffusion on Au(111), ideally in the presence of the surface reconstruction, in order to obtain more reliable values of the activation barriers. The effect of the STM tip on surface diffusion can also be investigated at a higher level of theory than semiempirical potential methods. When new insight has been gained in these fields, the atomistic model can be refined accordingly.

Appendix A

Nanofinger growth on Au(111) arising from kinetic instability

Nanofinger growth on Au(111) arising from kinetic instability

Nicola Totó,[1,2] Riccardo Ferrando,[3,*] Quanmin Guo,[1] and Roy L. Johnston[2,†]

[1]*School of Physics and Astronomy, University of Birmingham, Edgbaston, Birmingham B15 2TT, United Kingdom*
[2]*School of Chemistry, University of Birmingham, Edgbaston, Birmingham B15 2TT, United Kingdom*
[3]*Dipartimento di Fisica and INFM/CNR, Università di Genova, Via Dodecaneso 33, 16146 Genova, Italy*
(Received 16 February 2007; published 23 May 2007)

In recent experiments, nanofingers were obtained by repeatedly scanning a Au(111) surface with a scanning tunneling microscope tip. In the present work, a lattice model for the growth of nanofingers on the Au(111) surface is developed. Within this model, the activation barriers for diffusion are obtained by realistic semi-empirical calculations, and the dynamics are reproduced using kinetic Monte Carlo simulations. The simulation results are compared to the experiments, and the influence of various elementary atomic diffusion processes on the shape and size distribution of the nanofingers is analyzed.

I. INTRODUCTION

The tendency displayed by the electronics industry in recent decades toward the progressive reduction of typical device dimensions has prompted considerable interest in physical processes occurring on solid surfaces. Nanostructure formation on surfaces can proceed by direct manipulation of atoms or molecules adsorbed on the substrate by means of a scanning tunneling microscope (STM).[1,2] Alternatively, one can exploit the self-organization observed on surfaces of systems under out-of-equilibrium conditions, where patterns are formed due to kinetic, rather than thermodynamic, effects.[3–5] Such a situation is encountered, for instance, during homo- or heteroepitaxial metal growth, in that the deposition of atoms onto a substrate is inherently a nonequilibrium process.[6,7]

Recently, Guo *et al.*[8–11] have reported a series of experiments where a monoatomic step on a Au(111) surface was modified by repeatedly scanning a STM tip over it. After increasing the intensity of the electric field between the probe and the sample, the step profile started meandering and a pattern was induced, consisting of elongated structures resembling fingers running parallel to each other. The fingers displayed a thickness ranging from about 3 to 10 nm and were observed to grow only along one of the three equivalent close-packed directions on the surface.

In a previous work,[12] we built a simple bond-breaking model to account for the pattern formation on the Au(111) surface. In that model, the energy barrier of each diffusion process was assumed to depend only on the number of surface neighbors at the initial site of the hopping adatom. Although the bond-breaking model was able to reproduce a fingering instability, thus allowing a qualitative explanation of the phenomenon, neither the shape nor the thickness of the fingers was reproduced in agreement with the experiments. These results have motivated the development of a more refined model, incorporating more realistic activation barriers for the diffusion processes. These barriers are calculated within a semiempirical potential scheme. As we shall see in the following, this model will afford us a deeper insight into the phenomenon.

The paper is structured as follows. In Sec. II and III, the model and the calculation of activation barriers are described, respectively. Section IV reports the simulation results and the discussion. Finally, Sec. V contains the conclusions.

II. MODEL

The STM-induced step self-reorganization must be due to a rearrangement of atoms in the topmost surface layer. The experimental measurements[13] provide strong evidence to suggest that the reason underlying the finger growth is the detachment of atoms out of the upper terrace brought about by the intense electric field established between the STM tip and the substrate.

Based on the experimental observations, it is possible to draw a picture of the phenomenon wherein some of the atoms, previously embedded in the upper terrace and in close proximity to the step edge, are detached from the step by the tip. This creates on the lower terrace a distribution of adatoms, which can diffuse across the surface much more easily than before due to their decreased in-plane coordination. In their random walk across the plane, these freed adatoms may hit the step edge, where they are very likely to be captured.

We have, thus, set up a model for the finger growth, where the phenomenon results from the combination of two processes: the continuous flow of extracted atoms from the upper to the lower terrace, and the subsequent diffusion of these atoms across the lower terrace. In this model, only atoms belonging to the uppermost surface are considered. The system is treated as a lattice gas, where the only possible sites for atoms to rest in are nodes in a two-dimensional grid corresponding to threefold hollow sites on the fcc(111) surface. Thermally activated diffusion is reproduced by allowing each atom to hop into one of the unoccupied neighboring lattice sites. The rate r for an atom to hop into a nearest-neighbor site is

$$r = \nu \exp\left(-\frac{E_b}{k_B T}\right), \qquad (1)$$

where E_b is the energy barrier to the diffusion in the considered direction, k_B is the Boltzmann constant, and T is the system temperature.[14] The prefactor ν expresses the hopping

A.0   Nanofinger growth on Au(111) arising from kinetic instability

attempt rate and was chosen to be equal to 10^{12} s^{-1}. Each atom is, thus, associated with a diffusion rate, which is obtained by summing up the single rates for the diffusion onto each of the unoccupied nearest-neighbor sites.

The dynamics of the atoms on the surface are simulated by means of a kinetic Monte Carlo (KMC) algorithm based on the algorithm[15,16] of Bortz *et al.* During each iteration of the algorithm, an atom is selected to diffuse, the selection being biased according to the diffusion rate of each atom. The diffusion rate is proportional to the probability for the atom to diffuse. Once the diffusion step has been accomplished, the system is updated (i.e., the diffusion rates of the atoms affected by the diffusion process are recalculated) and the next iteration takes place.

The initial configuration has been chosen to be a monoatomic step running along the $\langle 11\bar{2} \rangle$ open direction (one of three equivalent open directions) on the close-packed surface. The simulation unit cell is rectangular, with one of the close-packed directions of the surface running parallel to the longer side of the rectangle. Periodic boundary conditions are imposed only in the surface plane, in the direction parallel to the step edge. The lattice gas at the beginning of each simulation is made up of 256 close-packed horizontal rows and 250 layers; i.e., the total number of atoms making up the system is 64 000.

In the model, the effect of the tip on the surface is taken into account by letting the outermost atom on the upper terrace be extracted from the step edge. After extraction, the atom is displaced by a distance of 100 times the nearest-neighbor distance away from its original position along the scan direction, which is always orthogonal to the orientation of the initial step. One atom is extracted at each simulated tip passage, with the atom selected for extraction displacement being the one located at the site of the orthogonal projection of the tip apex onto the surface.

It is clear that a central piece of information for the model is the height of the diffusion barriers associated with each hopping event. We have, therefore, undertaken an extensive series of atomistic calculations of diffusion barriers for an adatom, as described in Sec. III. All possible situations have been considered in terms of the local arrangement of atoms in the area surrounding the diffusing adatoms.

It is essential for the efficiency of the algorithm that all possible diffusion processes are divided into classes on the basis of a predefined criterion. We classify the processes according to the in-plane coordination of the atom on the sites occupied both before and after diffusion. The underlying assumption is that all interactions, other than nearest-neighboring interactions, can be disregarded when studying the system dynamics. This is justified by the extremely sticky, short-range nature of the interatomic potential of gold[17,18] and it has been confirmed by our calculations.

In our model, we do not take into account explicitly the $(23 \times \sqrt{3})$ reconstruction of the Au(111) surface, because a model with reconstruction would be so complicated as to become practically untractable. In fact, on the reconstructed surface, even the diffusion barrier for a single isolated adatom strongly depends on its position within the elementary reconstruction cell,[19,20] so that the single barrier of the unre-

constructed surface is replaced by a very large set of barriers. When considering a growing finger, the environment of each atom in the finger is different, so that the set of possible barriers becomes enormous. In this case, simple kinetic Monte Carlo simulation becomes infeasible. On the other hand, accelerated molecular dynamics (MD) or on-the-fly Monte Carlo methods,[21–23] even though applicable in principle, are not yet able to cope with the very large sizes and long time scales involved in the gold nanofinger growth. Our choice has, therefore, been to consider the unreconstructed surface, to show that the origin of the fingering instability is not due to surface reconstruction, and to discuss the possible effects that the reconstruction may have on finger shape.

III. ATOMISTIC CALCULATIONS OF DIFFUSION BARRIERS

A. Potential and methodology

In order to be able to control the formation of nanostructures on metal surfaces, it is essential to understand the atomistic mechanisms which underlie the growth phenomena.[5,24] We have, therefore, carried out a thorough numerical study of diffusion on the Au(111). We have calculated the values of the energy barriers associated with the diffusion processes which are included in the model. For these calculations, we have used a many-body potential of the tight-binding type in conjunction with a minimization procedure based on MD quenching.

The potential we have chosen is the Gupta or Rosato-Guillopé-Legrand (RGL) potential.[25–28] It was developed within the framework of the second-moment approximation to the density of states in the tight-binding model. In the Gupta potential, the energy of an atom i can be expressed as the sum of two contributions. The first term E_r^i expresses a pairwise repulsive interaction:

$$E_r^i = \sum_{j \neq i, r_{ij} < r_c} A \exp\left[-p\left(\frac{r_{ij}}{r_0} - 1 \right) \right], \qquad (2)$$

where r_{ij} is the distance between atoms i and j, r_c is the cutoff radius, r_0 is the nearest-neighbor distance, and p is a parameter determining the spatial range of the interaction. The second term E_b^i is of many-body character and it describes the binding between atoms due to the delocalized electrons:

$$E_b^i = -\left\{ \sum_{j \neq i, r_{ij} < r_c} \xi^2 \exp\left[-2q\left(\frac{r_{ij}}{r_0} - 1 \right) \right] \right\}^{1/2}, \qquad (3)$$

where ξ is the hopping integral, and the parameter q describes the distance dependence of the hopping integral. The total energy E_c of the system is obtained as

$$E_c = \sum_i (E_b^i + E_c^i). \qquad (4)$$

The four parameters (A, ξ, p, and q) are fitted to experimental values of the cohesive energy, lattice parameter, bulk modulus, and the elastic constants C_{44} and C'. The values of the parameters used in our calculations are as follows: A

195434-2

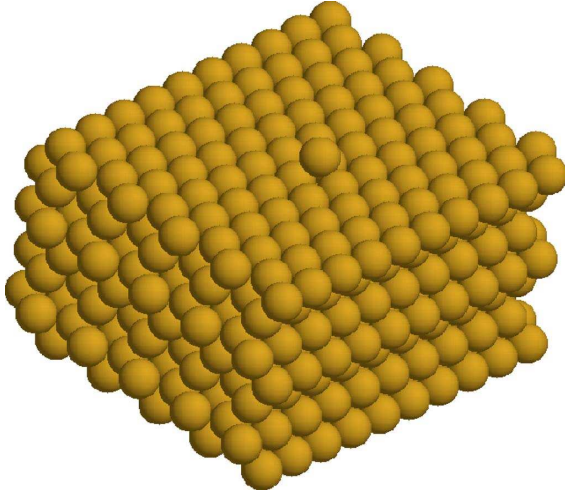# A.0   Nanofinger growth on Au(111) arising from kinetic instability

FIG. 1. (Color online) Unit cell used for the atomistic calculations of diffusion barriers. Periodic boundary conditions are applied on the surface plane.

FIG. 2. (Color online) Different processes whose activation barriers have been calculated. The first and second integers indicate the initial and final in-plane coordinations of the diffusing adatom, respectively. Inverse processes are not shown (see text).

$=0.2096$ eV, $\xi=1.8153$ eV, $p=10.139$, $q=4.033$, and $r_0 =2.884$ Å.[29] The cutoff r_c is taken at the second-nearest-neighbor distance, and the potential is smoothly brought to zero through a fifth-order polynomial at the third-nearest-neighbor distance. Alternative parameter sets[27,28] or longer cutoff distances would produce very small differences in the results reported in the following. This potential has been shown to be able to predict correctly the missing-row reconstruction of the (110) surface. On that surface, the activation barriers for diffusion are in good agreement with the experimental values (see Ref. 17), even though there is some tendency to underestimate the actual values.

The unit cell used in the MD calculations is a slab made of seven Au(111) planes stacked in *ABC* fashion, as shown in Fig. 1. Each plane contains ten atoms in the $\langle 1\bar{1}0 \rangle$ close-packed direction and ten atoms in the orthogonal $\langle 11\bar{2} \rangle$ open direction. Periodic boundary conditions are applied in both directions across the surface plane. The diffusing adatom rests on the topmost plane and is led through a path connecting the initial and final sites. At each point along the path, the system energy is minimized locally while fixing the diffusing adatom coordinate parallel to the surface plane. The remaining coordinates of the diffusing adatoms, along with the degrees of freedom of the other atoms in the slab, are relaxed. The atoms making up the bottom plane constitute an exception, in that they are kept fixed in their respective positions so as to simulate the effect of the bulk crystal on the outermost planes.

Energy minimization is achieved through a quenching procedure making use of classical molecular dynamics. Initially, with the system in its unrelaxed state, the classical equations of motion are solved by means of the velocity-Verlet algorithm.[30] The quenching is accomplished by canceling all those components of an atom's velocity whose scalar product with the force acting on the atom is negative.
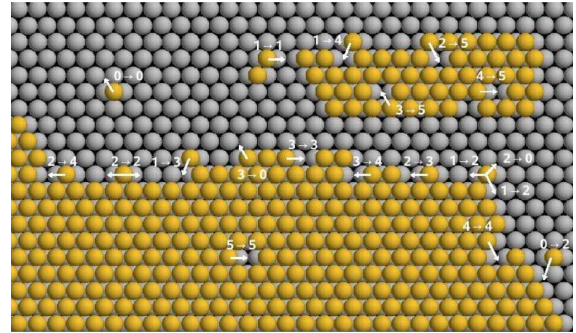
This allows the system to relax into the closest local minimum. Quenching is terminated when the system temperature is lower than 10^{-5} K. The diffusion barrier for the process is then obtained by taking the difference between the system energy in the transition state and in its initial state, with the diffusing adatom resting on a threefold hollow site.

As mentioned above, we have classified all diffusion processes on the basis of the in-plane coordination of the diffusing adatom before and after diffusion. This simplification is allowed by our observation that in gold second-nearest-neighbor interactions and above have insignificant effects with respect to first-nearest-neighbor interactions. In fact, we have compared the height of the barriers obtained in diffusion calculations for different surface configurations but with equal arrangements of first neighbors of the diffusing adatom. We have found that the number of first neighbors is, by far, the most important determinant of the barrier height and that different configurations of second neighbors and above affect the calculations to a negligible extent. In our atomistic calculations, we have considered those processes whose occurrence is more likely during the KMC simulations of finger growth. These processes are shown in Fig. 2. In the figure, all processes are labeled by two positive integers connected by an arrow, which indicate, respectively, the initial and final in-plane coordinations of the diffusing adatom. Given a diffusion process where the adatom hops from a site of in-plane coordination n to a site of coordination m, we define its inverse by that process where the adatom diffuses from an m-fold to an n-fold coordinated lattice site. In the figure, we choose to show only one process for each pair ($n \rightarrow m$, $m \rightarrow n$). Inverse processes can be obtained in a straightforward manner.

B. Diffusion barriers

The results of the diffusion barrier calculations are listed in Table I. This work extends a previous study[31] where adatom diffusion along step edges on the (111) surfaces of Au and Ag was addressed. Our calculations generally agree with the results found by Ferrando and Treglia, with a different

A.0 Nanofinger growth on Au(111) arising from kinetic instability

TOTÓ *et al.*

TABLE I. Barriers for the diffusion processes included in the KMC model, as calculated with the Gupta potential.

Process $i \rightarrow f$	E_b (eV) $A\|B$	Process $i \rightarrow f$	E_b (eV) $A\|B$	Process $i \rightarrow f$	E_b (eV) $A\|B$
$0 \rightarrow 0$	0.10	$2 \rightarrow 0$	0.52|0.54		
$0 \rightarrow 1$	0.08	$2 \rightarrow 1$	0.39|0.25	$4 \rightarrow 1$	0.57|0.67
$0 \rightarrow 2$	0.09|0.11	$2 \rightarrow 2$	0.33|0.24	$4 \rightarrow 2$	0.54|0.63
$0 \rightarrow 3$	0.10	$2 \rightarrow 3$	0.33|0.22	$4 \rightarrow 3$	0.53|0.61
		$2 \rightarrow 4$	0.21|0.30	$4 \rightarrow 4$	0.56|0.55
		$2 \rightarrow 5$	0.02	$4 \rightarrow 5$	0.31|0.31
$1 \rightarrow 0$	0.31	$3 \rightarrow 0$	0.70		
$1 \rightarrow 1$	0.33	$3 \rightarrow 1$	0.55|0.44		
$1 \rightarrow 2$	0.16|0.04	$3 \rightarrow 2$	0.45|0.40	$5 \rightarrow 2$	0.54
$1 \rightarrow 3$	0.15|0.04	$3 \rightarrow 3$	0.48|0.41	$5 \rightarrow 3$	0.52|0.51
$1 \rightarrow 4$	0.04|0.12	$3 \rightarrow 4$	0.45|0.39	$5 \rightarrow 4$	0.52|0.53
		$3 \rightarrow 5$	0.15|0.16	$5 \rightarrow 5$	0.46

parametrization of the potential likely being responsible for the slight differences observed.

By studying the processes of adatom detachment from a corner site, step edge, and kink site, denoted by $1 \rightarrow 0$, $2 \rightarrow 0$, and $3 \rightarrow 0$, respectively, one can notice a roughly linear increase in the height of the activation barrier with increasing initial coordination: the height of the barrier increases by around 0.20 eV for each new first neighbor in the initial position.

In contrast, the inverse processes, i.e., the capture of a free adatom by a defect on the step, display almost the same activation barrier, regardless of the nature of the final position after diffusion. The values are very similar to the case of diffusion on the bare surface. The reason for this is that the perturbation created by the presence of the defect on the surface (corner, step, or kink) is not experienced by the diffusing adatom in the transition state, due to the extremely short-range nature of the interaction. In fact, we have found that the potential of an adatom is influenced dramatically by the presence of a surface defect. However, the effect is noticeable only in close proximity to the defect. For instance, by comparing the system energy at the beginning and at the end of the processes $0 \rightarrow 2$ and $0 \rightarrow 3$, we notice that the difference in bonding energy of the diffusing adatom between the two states is 0.44 and 0.60 eV, respectively. But the bonding energy of the adatom in the initial position is not significantly lower than for the adatom in a fcc threefold hollow site far away from the defect, the difference being only 2−3 meV. In conclusion, we have found that the kinetics of free adatom trapping by a surface defect occur on the same time scale, regardless of the particular type of defect. Furthermore, the probability for a free adatom to be captured by a defect is almost the same as that for diffusion on the bare surface. In other words, when an adatom approaches a defect, it will move away from and toward the defect with almost the same probability. However, once the atom is trapped by the defect, it has a low probability of being released back onto the lower terrace.

FIG. 3. (Color online) Series of images taken during a KMC simulation at 300 K. (a) System configuration after 2×10^8 iterations; system time 4 s. (b) System configuration after 4×10^8 iterations; system time 7 s. (c) System configuration after 10^9 iterations; system time 18 s.

We can calculate the typical times for each diffusion process occurring at a temperature of 300 K by means of Eq. (1). For instance, an atom occupying a corner position (in-plane coordination of 1) can move to the nearest step edge site (in-plane coordination of 4) within a typical time of the order of a few picoseconds for an A-type step and 100 ps for a B-type step. Other options are capture by a neighboring kink site ($1 \rightarrow 3$) and diffusion into the channel opposite the step edge ($1 \rightarrow 2$). Both these processes occur within similar time scales of the order of 100 ps and a few picoseconds for A-type and B-type steps, respectively. However, the expulsion from the corner into the lower terrace ($1 \rightarrow 0$) and the diffusion into an adjacent corner site ($1 \rightarrow 1$) are much slower processes with a characteristic time of around 100 μs. Analogously, an adatom resting in the channel directly opposite a step (in-plane coordination of 2) can either diffuse along the step ($2 \rightarrow 2$) or be captured by a kink ($2 \rightarrow 3$) or step edge site ($2 \rightarrow 4$) with almost the same probability. However, the activation energy required for the adatom to leave the channel and reach the terrace ($2 \rightarrow 0$) is much higher than for the former processes.

IV. RESULTS OF KMC CALCULATIONS

The set of activation barriers listed in Table I has been used as input parameters for the KMC code described in Sec. II. In those cases where the barrier for A-type and B-type steps differ, we have chosen the average of the two values in the KMC calculations. The main difference between the present model and that used in our previous study[12] is that in
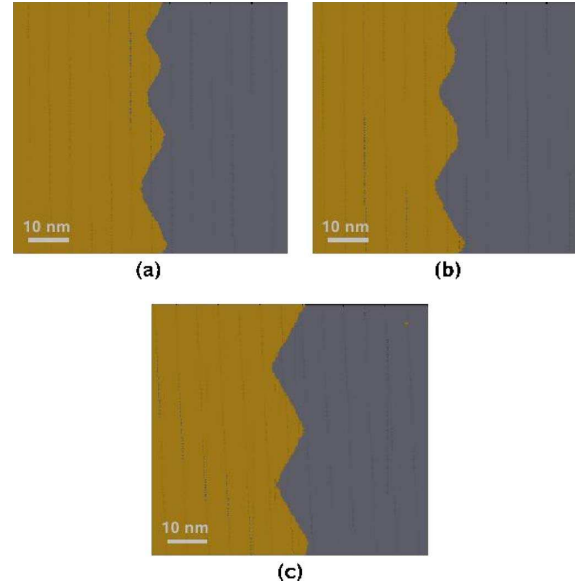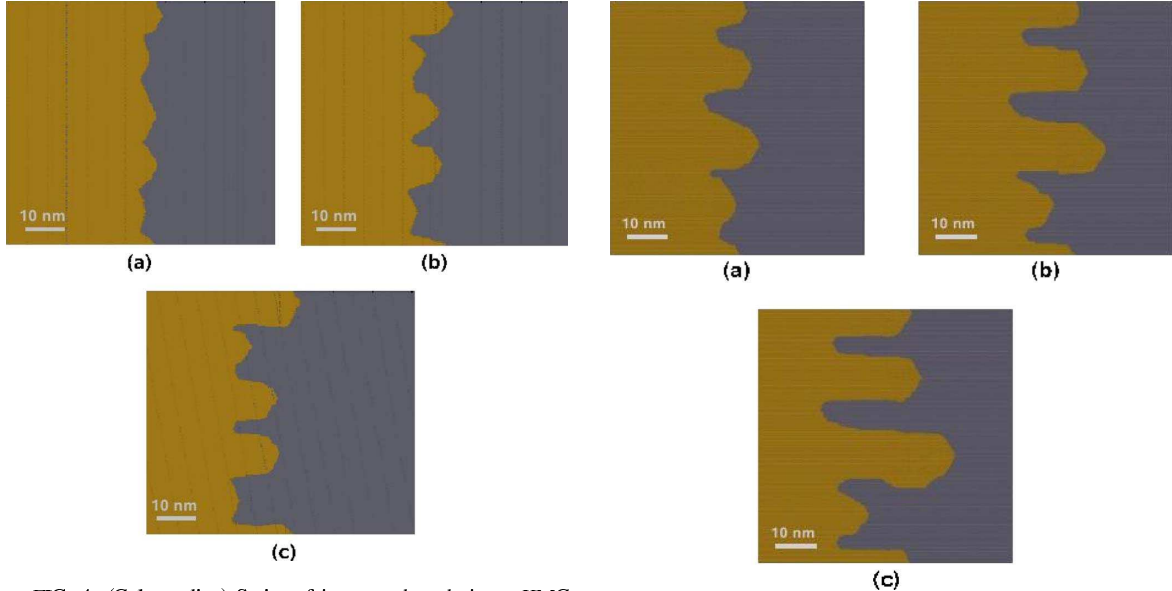
FIG. 4. (Color online) Series of images taken during a KMC simulation at 200 K. (a) System configuration after 10^9 iterations; system time 24.3 s. (b) System configuration after 1.2×10^9 iterations; system time 29.7 s. (c) System configuration after 1.4×10^9 iterations; system time 35.4 s.

the latter all possible diffusion processes occurred at the same rate for each adatom, thus restricting the number of possible diffusion processes to 6. On the contrary, here, many more processes are taken into account, thus allowing a more realistic simulation of the adatom kinetics on the surface.

When the code is run at a system temperature of 300 K, a distinctive zigzag pattern is observed for the step reorganization after the STM scan. The step tends to rearrange along

FIG. 5. (Color online) A typical result obtained at 300 K with the set of barriers quoted in Table I multiplied by the factor 1.5. (a) System cofiguration after 1.2×10^9 iterations; system time 29.8 s. (b) System cofiguration after 1.5×10^9 iterations; system time 38.8 s. (c) System cofiguration after 1.7×10^9 iterations; system time 46.2 s.

two of the three equivalent close-packed directions, giving rise to an alternation of straight segments forming alternatively angles of 120° and 240° with respect to each other. The system eventually relaxes toward a quasiperiodical pattern of periodicity around 30 nm. This *equilibrium configuration* is finally reached, irrespective of the scan rate and the displacement length chosen for the atom detachment from
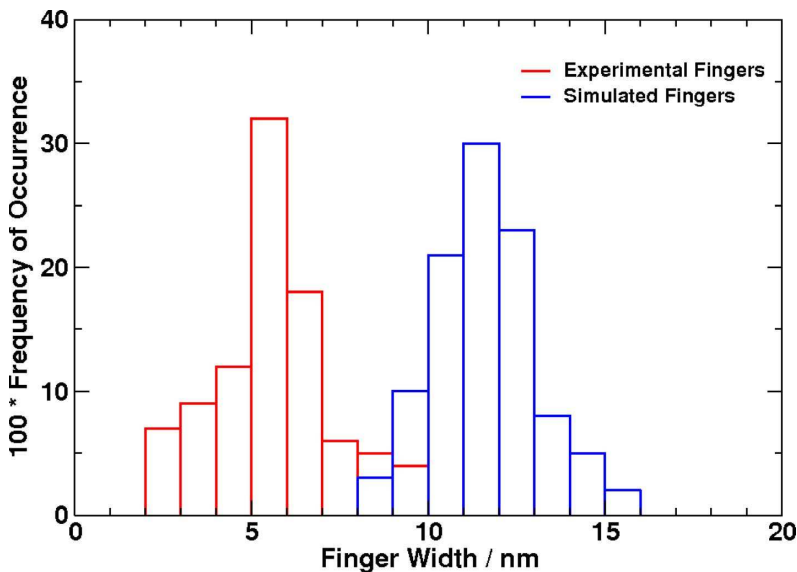
FIG. 6. (Color online) Width distribution of the finger pattern obtained experimentally (red) and in our calculations (blue).
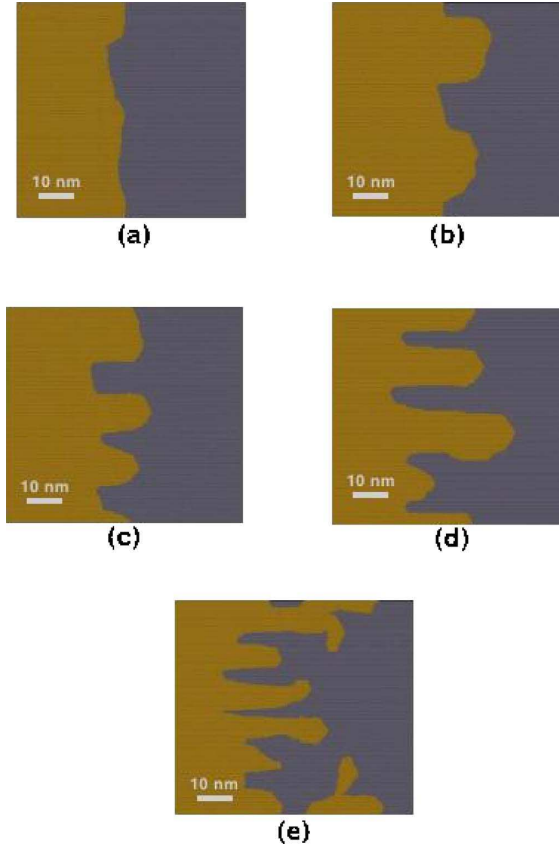
FIG. 7. (Color online) Patterns obtained by altering the value of E_{22}. (a) E_{22}=0.28 eV, configuration after 2×10^9 iterations, and system time 47.3 s. (b) E_{22}=0.36 eV, configuration after 2×10^9 iterations, and system time 49.6 s. (c) E_{22}=0.40 eV, configuration after 1.8×10^9 iterations, and system time 45.3 s. (d) E_{22}=0.43 eV, configuration after 1.7×10^9 iterations, and system time 46.2 s. (e) E_{22}=0.50 eV, configuration after 1.4×10^9 iterations, and system time 45.0 s.

the upper terrace. In Fig. 3, a series of images are shown for a KMC calculation carried out at 300 K, using a scan rate of 500 Hz and a displacement of 100 times the nearest-neighbor distance.

When the system temperature is reduced to 200 K, the pattern formed on the step edge changes completely. For a sufficiently high scan rate, the instability producing the finger pattern starts to appear after a certain number of iterations. The fingers grow perpendicular to the step, along one of the $\langle 1\bar{1}0 \rangle$ close-packed directions, as observed experimentally. As an example of the pattern which could be produced at a temperature of 200 K with the set of barriers quoted in Table I, we show in Fig. 4 a series of images taken during a typical run, where a scan rate of 500 Hz and an atom displacement of 100 times the nearest-neighbor distance were chosen. This pattern looks quite similar to that observed in the experiments at room temperature. There is, therefore, a mismatch between the experiments and the simulations,
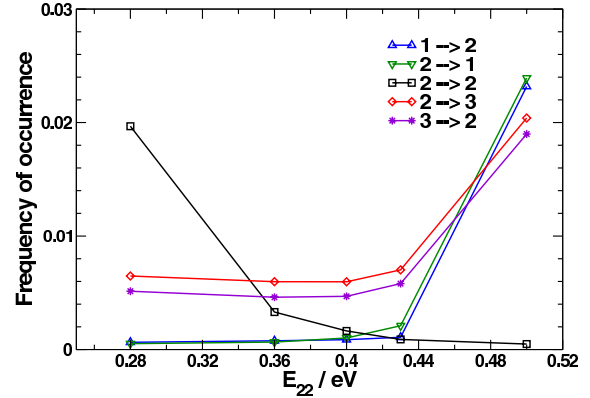
FIG. 8. (Color online) Frequency of occurrence of some particularly significant diffusion processes plotted as a function of E_{22}. For clarity of display, all curves have been rescaled by a factor of 100, except for the $2 \rightarrow 2$ process.

which is a clear indication that the atomistic calculations have underestimated the barrier heights. The reasons for this are twofold. It is known that semiempirical potentials tend to underestimate the surface free energy,[27] thus providing too low values for transition state energies. Furthermore, previous calculations have shown that self-diffusion on the Au(111) surface is hindered when the presence of the $(23 \times \sqrt{3})$ reconstruction is taken into account.[19,20]

Since our atomistic calculations have been carried out on the unreconstructed Au(111) surface, the barrier heights we have found are likely to be too low. We, therefore, have multiplied all the barriers we have calculated by the same factor of 1.5. This value matches well the factor of 1.3 found by Boisvert and Lewis[19] for the ratio of the diffusion activation energy on the reconstructed to that on the bulklike Au(111) surface. A new series of KMC calculations have then been performed using the set of rescaled barriers. With these new values, the simulation produces, at the correct temperature of 300 K, the same finger pattern as that previously obtained using the calculated activation energies at 200 K. Examples of the results that we typically observe at 300 K, using a scan rate of 500 Hz, are displayed in Fig. 5.

A statistical analysis of the finger width, both in the case of the simulated and experimental patterns, has been undertaken. We have found that the distribution is close to normal in both cases, with almost the same amplitude. However, one can notice a clear difference between the two histograms in Fig. 6, in that the whole thickness distribution of the simulated fingers is shifted to higher width by approximately a factor of 2 with respect to the distribution of the experimental fingers. Therefore, the simulated pattern, though qualitatively similar, cannot reproduce faithfully the experimental data.

By analyzing the frequency of occurrence of each diffusion process, we have noticed that the overwhelming majority of events are diffusions of free adatoms on the lower terrace $(0 \rightarrow 0)$, which contribute 99.89% of the total diffusion processes. Step edge diffusion $(2 \rightarrow 2)$ is the second most frequent process, with an occurrence of $8.9 \times 10^{-2}\%$,
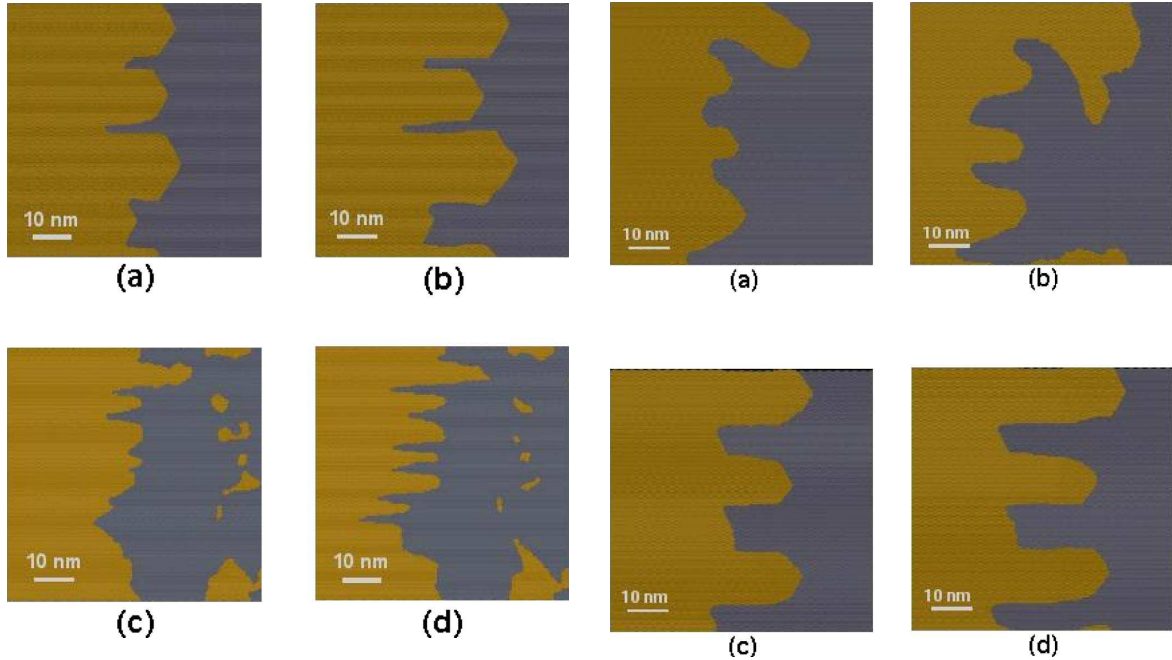
FIG. 9. (Color online) Patterns obtained by altering the value of E_{21}. [(a) and (b)] Configurations obtained for $E_{21}=0.38$ eV after 1.4×10^9 iterations (system time=35.4 s) and 1.8×10^9 iterations (system time=47.2 s), respectively. [(c) and (d)] Configurations obtained for $E_{21}=0.59$ eV after 1.2×10^9 iterations (system time =47.7 s) and 1.3×10^9 iterations (system time=67.5 s), respectively.

FIG. 10. (Color online) Patterns obtained by altering the value of E_{32}. [(a) and (b)] Configurations obtained for $E_{32}=0.60$ eV after 1.5×10^9 iterations (system time=35.4 s) and 1.9×10^9 iterations (system time=58.2 s), respectively. [(c) and (d)] Configurations obtained for $E_{32}=0.67$ eV after 1.6×10^9 iterations (system time =41.8 s) and 1.8×10^9 iterations (system time=49.2 s), respectively.

followed by adatom attachment to a step kink $(2\rightarrow3)$, 7 $\times10^{-3}\%$. We finally observe that the number of atoms that attach to a step edge from the lower terrace (process $0\rightarrow2$) is almost the same as the number of atoms extracted by the tip from the edge. This observations allow one to understand the adatom kinetics on the surface. Once the adatoms are released by the tip onto the terrace, they perform a random walk across the surface until the edge of the upper terrace is approached. When attached to a close-packed step, the adatoms are allowed to migrate along the edge, but as soon as they come across a kink, they are trapped by the step defect.

In order to study the effect of diffusion on the pattern formation, we have selectively modified the values of those barriers which are responsible for the most influential diffusion processes affecting finger shape. The relationship between adatom diffusion and the formation of adatom islands on surfaces is now a well-established field of study. Island formation during homoepitaxial growth has been studied on close-packed surfaces such as Pt(111),[32–35] Al(111),[36] and Ag(111).[37] Both experimental surface characterization techniques and atomistic modeling have been employed to cast light on the atomic processes which are most likely to influence the wide range of patterns observed during epitaxial metal growth. Among these are diffusion across a bare terrace, along a step edge, and around a corner or a kink on a close-packed step.

We have started with a study of the influence of edge diffusion on finger growth. In Fig. 7, the results obtained for different values of E_{22} are compared, while in the graph in Fig. 8 the frequency of occurrence of some particularly significant processes is plotted as a function of E_{22}. If the step edge diffusion is too fast, no instability can set in, since the step has time to rearrange to a lower-energy configuration. As long as E_{22} is increased, the finger pattern will start to appear. The steady decrease in the occurrence of edge diffusions as the barrier height increases is accompanied by an equally steady increase in the occurrence of other processes, such as corner rounding and detachment from and attachment to a kink, which at very low E_{22} occur in much lower proportion. The instability manifests itself as thick bulges along the step for low values of E_{22}. The fingers get thinner and thinner as the edge diffusion gets slower. Finally, when the barrier responsible for step diffusion is too high, bifurcations, giving rise to secondary branches, are observed due to the tendency displayed by the fingers to develop bulges on top. This is reflected in the high frequency of all processes other than edge diffusion.

We subsequently turned our attention to diffusion processes at or around corners. The barrier E_{21} has proven to be particularly influential for the pattern appearance, as can be seen in Fig. 9. Lowering E_{21} leads to an enhancement of corner diffusions $(1\rightarrow2$ and $2\rightarrow1)$, resulting in the forma-

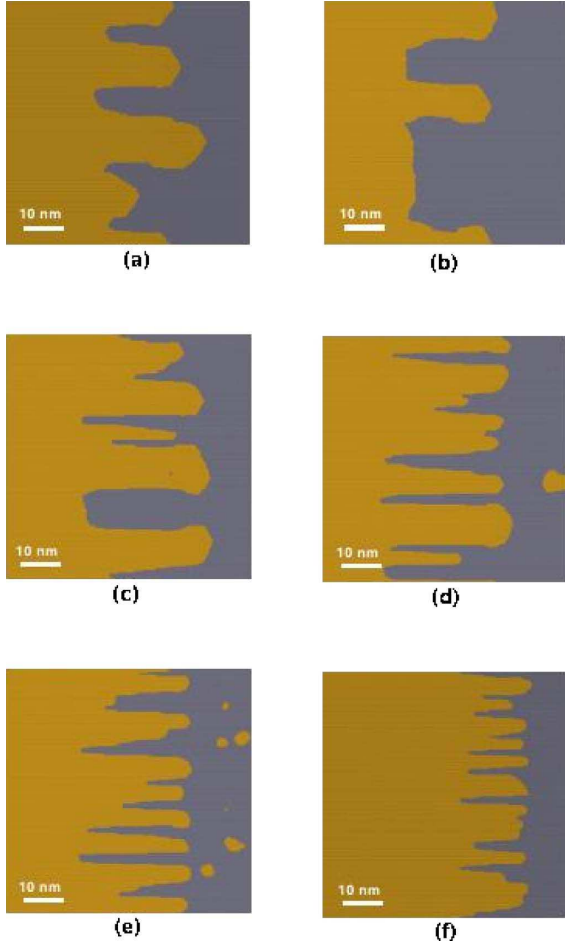# A.0   Nanofinger growth on Au(111) arising from kinetic instability

FIG. 11. (Color online) Patterns obtained by altering the value of E_{00}. (a) E_{00}=0.15 eV, configuration after 1.6×10^9 iterations, and system time 42.2 s. (b) E_{00}=0.25 eV, configuration after 7×10^8 iterations, and system time 27.0 s. (c) E_{00}=0.30 eV, configuration after 4×10^8 iterations, and system time 46.4 s. (d) E_{00}=0.35 eV, configuration after 1.4×10^8 iterations, and system time 56.2 s. (e) E_{00}=0.40 eV, configuration after 10^8 iterations, and system time 55.6 s. (f) E_{00}=0.45 eV, configuration after 10^8 iterations, and system time 41.3 s.

tion of thick, closely spaced fingers. On the other hand, by making the corner diffusion more difficult, a more rugged, irregular pattern is induced. The formation of islands is observed in this case, along with rough profile fingers whose width is much less than in the previous case.

The influence of the kinks on the step rearrangement has also been studied. One process we have identified as particularly important is adatom release by a kink followed by migration of the adatom to an edge site ($3 \rightarrow 2$). We have said before that kinks act as *traps* for adatoms diffusing on step edges. Once trapped in kink sites, the adatoms are released back to the step with low probability and stand almost no chance of reaching the corner site adjacent to the kink or a

FIG. 12. Mean finger thickness as a function of E_{00}.

terrace site. If E_{32} is lowered, a tendency of the fingers to bend laterally and to develop bifurcations is observed [see Figs. 10(a) and 10(b)]. On the other hand, when the step adatom release by kinks is made slower, the fingers tend to grow along the same close-packed direction, thus resulting in a well-aligned, parallel pattern [see Figs. 10(c) and 10(d)]. In other words, the *trapping power* of kinks affects the directionatility of the finger growth. A too high adatom release rate from a kink to an edge site hinders the finger growth by causing the fingers to bend laterally. If, instead, kink sites are traps which the adatoms can barely leave, the growth of straight fingers is favored. We also point out that the fingers in Figs. 10(c) and 10(d) are thinner and more widely spaced than those in Figs. 9(a) and 9(b). The decreased width is most probably due to the dramatically reduced amount of adatom corner crossing (processes $1 \rightarrow 2$ and $2 \rightarrow 1$) with respect to the case in Figs. 9(a) and 9(b), where this type of process occurs an order of magnitude more frequently.

Finally, the effect of terrace diffusion on the finger pattern has been investigated. The effects of the alteration of E_{00} are dramatic, as shown in Fig. 11. Generally speaking, one notices that by increasing the height of the barrier for terrace diffusion, the pattern produced displays thinner and better aligned fingers. This qualitative observation has been confirmed by a quantitative statistical analysis of the width distribution obtained for each value of E_{00}. In Fig. 12, we have plotted the mean value of each distribution as a function of E_{00}; the error bars representing the standard deviation of the mean. The mean width decreases steadily as the barrier increases. For values of E_{00} greater than 0.35 eV, a plateau is reached. This trend is similar to that which we have found when comparing the most relevant diffusion processes. For E_{00} in the range between 0.20 and 0.35 eV, the diffusions on the bare surface undergo a steep decrease in favor of step, corner, and kink diffusions, whose occurrence increase as rapidly. This increase seems to slow down for E_{00} above 0.35 eV.

The hindering of terrace diffusion (by increasing E_{00}) obviously leads to an increase in probability of the other processes (Fig. 13). In particular, corner diffusion ($1 \rightarrow 2$ and $2 \rightarrow 1$) undergo the sharpest rise as the $0 \rightarrow 0$ barrier is in-

A.0 Nanofinger growth on Au(111) arising from kinetic instability

FIG. 13. (Color online) Frequency of occurrence of some particularly significant diffusion processes plotted as a function of E_{00}.

FIG. 14. (Color online) (a) Experimental STM scan taken after manipulation of a step edge on Au(111). Bias voltage=1 V and tunneling current=0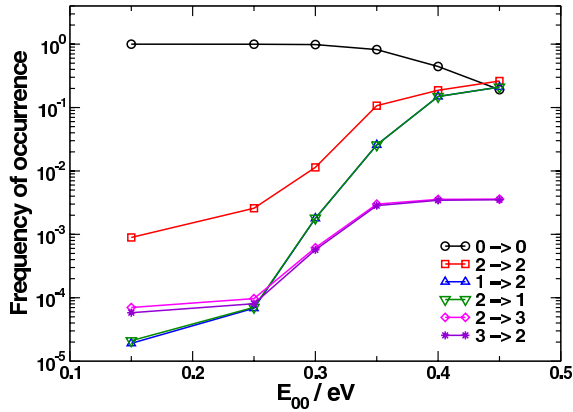.2 nA [courtesy of Yin (Ref. 13)]. (b) Simulated pattern with E_{00}=0.35 eV. System configuration after 10^8 iterations; system time 56.7 s.

creased. But also step and kink diffusions are faster when terrace diffusion slows down, which causes the step edge to rearrange more swiftly. This, together with the increasing density of isolated adatoms on the lower terrace, brings the system out of equilibrium to a greater extent, which, in turn, leads to the formation of thinner fingers. We note that the pattern obtained by fine-tuning E_{00} bears a striking resemblance (same shape and thickness) to the experimental data, as shown in Fig. 14.

V. CONCLUSIONS

We have set up a realistic model of diffusion on the Au(111) surface in the presence of a step edge and a STM-induced electric field. This is an example of a system which is brought out of equilibrium by a perturbation, which in this case is represented by the STM tip. Experimentally, the step proves to be unstable under the effect of such a perturbation. We have managed to reproduce this instability at an excellent degree of accuracy, both from a qualitative and a quantitative point of view.

The phenomenon investigated here is reminiscent of the Bales-Zangwill (BZ) instability for homoepitaxial growth of metals in the step-flow regime.[38–41] In our case, as well as in the case studied by BZ, the instability is prompted by the tendency displayed by those parts of the step edge with higher curvature to attract the free adatom roaming the surface much more efficiently than others. The fundamental difference between the present system and the BZ instability is that the whole phenomenon occurs here on the lower terrace,

which allows us not to assume anything like an Ehrlich-Schwoebel barrier[42] in our model.

Our atomistic calculations of diffusion barriers, together with the KMC algorithm we have set up, have proven that the pattern resulting from the instability is a delicate interplay of all the processes considered in the model. We have managed to relate the appearance of the finger pattern to a number of important atomistic processes, such as diffusion on the bare surface, along step edges, around corners, and in proximity to kinks.

In summary, we have found that the kinetic instability driving gold nanofinger growth is not caused directly by the substrate reconstruction, since the instability also manifests itself when reconstruction is not taken into account. However, our results indicate that reconstruction is important for determining the actual finger shape and thickness. In fact, the reconstruction induces an increase in the diffusion barriers[20] for isolated adatoms. Our simulations have explicitly shown that this increase causes the growth of thinner and better aligned fingers. For a barrier of 0.35 eV [a barrier which is too high for diffusion on unreconstructed Au(111)], simulated fingers match the experimental results perfectly.

Finally, we remark that we would welcome a thorough first-principles calculation of diffusion barriers on the Au(111) surface which, besides casting light on the surface itself, would provide our model with a more accurate set of input parameters.

*Email address: ferrando@fisica.unige.it

†Email address: r.l.johnston@bham.ac.uk

[1] D. M. Eigler and E. K. Schweizer, Nature (London) **344**, 524 (1990).

[2] M. F. Crommie, C. P. Lutz, and D. M. Eigler, Science **262**, 218 (1993).

[3] H. Röder, E. Hahn, H. Brune, J. Bucher, and K. Kern, Nature (London) **366**, 141 (1993).

[4] H. Brune, M. Giovannini, K. Bromann, and K. Kern, Nature (London) **394**, 451 (1998).

[5] J. V. Barth, G. Costantini, and K. Kern, Nature (London) **437**, 671 (2005).

[6] H. Brune, Surf. Sci. Rep. **31**, 121 (1998).

[7] A. C. Levi and M. Kotrla, J. Phys.: Condens. Matter **9**, 299 (1997).

[8] Q. Guo, F. Yin, and R. E. Palmer, Small **1**, 76 (2005).

[9] F. Yin, R. E. Palmer, and Q. Guo, Phys. Rev. B **73**, 073405 (2006).

[10] F. Yin, R. E. Palmer, and Q. Guo, Surf. Sci. **600**, 1504 (2006).

[11] F. Yin, Q. Guo, and R. E. Palmer, Jpn. J. Appl. Phys., Part 1 **45**, 2053 (2006).

[12] N. Totó, R. Ferrando, R. L. Johnston, and Q. Guo, Surf. Sci. (to be published).

[13] F. Yin (private communication).

[14] T. Ala-Nissila, R. Ferrando, and S. C. Ying, Adv. Phys. **51**, 949 (2002).

[15] A. B. Bortz, M. H. Kalos, and J. L. Lebowitz, J. Comput. Phys. **17**, 10 (1975).

[16] M. Kotrla, Comput. Phys. Commun. **97**, 82 (1996).

[17] F. Montalenti and R. Ferrando, Phys. Rev. B **59**, 5881 (1999).

[18] F. Baletto and R. Ferrando, Rev. Mod. Phys. **77**, 371 (2005).

[19] G. Boisvert and L. Lewis, in *Physics Computing 94*, edited by R. Gruber and M. Tomassini (European Physical Society, Geneva, 1994), p. 29.

[20] Y. B. Liu, D. Y. Sun, and X. G. Gong, Surf. Sci. **498**, 337 (2002).

[21] A. F. Voter, F. Montalenti, and T. C. Germann, Annu. Rev. Mater. Res. **32**, 321 (2002).

[22] G. Henkelman and H. Jonsson, J. Chem. Phys. **115**, 9657 (2001).

[23] O. Trushin, A. Karim, A. Kara, and T. S. Rahman, Phys. Rev. B **72**, 115401 (2005).

[24] Z. Zhang and M. G. Lagally, Science **276**, 377 (1997).

[25] R. P. Gupta, Phys. Rev. B **23**, 6265 (1981).

[26] D. Tomanek, A. A. Aligia, and C. A. Balseiro, Phys. Rev. B **32**, 5051 (1985).

[27] V. Rosato, M. Guillopé, and B. Legrand, Philos. Mag. A **59**, 321 (1989).

[28] F. Cleri and V. Rosato, Phys. Rev. B **48**, 22 (1993).

[29] C. Mottet (private communication).

[30] D. Frenkel and B. Smit, *Understanding Molecular Simulation, From Algorithms to Applications* (Academic, San Diego, 1996).

[31] R. Ferrando and G. Treglia, Phys. Rev. B **50**, 12104 (1994).

[32] T. Michely, M. Hohage, M. Bott, and G. Comsa, Phys. Rev. Lett. **70**, 3943 (1993).

[33] S. Liu, Z. Zhang, G. Comsa, and H. Metiu, Phys. Rev. Lett. **71**, 2967 (1993).

[34] J. Jacobsen, K. W. Jacobsen, and J. K. Nøorskov, Surf. Sci. **359**, 37 (1996).

[35] J. Wu, E. G. Wang, K. Varga, B. G. Liu, S. T. Pantelides, and Z. Zhang, Phys. Rev. Lett. **89**, 146103 (2002).

[36] S. Ovesson, A. Bogicevic, and B. I. Lundqvist, Phys. Rev. Lett. **83**, 2608 (1999).

[37] E. Cox, M. Li, P. W. Chung, C. Ghosh, T. S. Rahman, C. J. Jenks, J. W. Evans, and P. A. Thiel, Phys. Rev. B **71**, 115414 (2005).

[38] G. S. Bales and A. Zangwill, Phys. Rev. B **41**, 5500 (1990).

[39] I. Bena, C. Misbah, and A. Valance, Phys. Rev. B **47**, 7408 (1993).

[40] A. Pimpinelli, I. Elkinani, A. Karma, C. Misbah, and J. Villain, J. Phys.: Condens. Matter **6**, 2661 (1994).

[41] O. Pierre-Louis, C. Misbah, Y. Saito, J. Krug, and P. Politi, Phys. Rev. Lett. **80**, 4221 (1998).

[42] G. Ehrlich and F. G. Hudda, J. Chem. Phys. **44**, 1039 (1966).

Appendix B

Theoretical investigations of nanopatterning on the Au(111) surface

Bibliography

[1] Johnston, R. L. *Evolving better nanoparticles: Genetic algorithms for optimising cluster geometries*. Dalton Trans., 2003. page 4193.

[2] Baletto, F. & Ferrando, R. *Structural properties of nanoclusters: Energetic, thermodynamic, and kinetic effects*. Rev. Mod. Phys., 2005. **77**, 371.

[3] Doye, J. P. K. *Physical perspective on the global optimization of atomic clusters*. In Pintér, J. D., editor, *Global Optimization, Scientific and Engineering Case Studies*, volume 85 of *Nonconvex Optimization and Its Applications*. Springer, 2006 .

[4] Martin, T. P. *Shells of Atoms*. Phys. Rep., 1996. **57**, 201.

[5] Sebetci, A. & Güvenç, Z. B. *Global minima of Al_N, Au_N and Pt_N, $N \leq 80$, clusters described by Voter-Chen version of embedded-atom potentials*. Model. Simul. Mat. Sci. Eng., 2005. page 683.

[6] Schwartz, L. W. *Viscous flow down an inclined plane: instability and finger formation*. J. Phys. Fluids A, 1989. **1**, 443.

[7] DiFrancesco, M. W. & Maher, J. V. *Noisy and Regular features in Saffman-Taylor patterns*. Phys. Rev. A, 1989. **39**, 4709.

[8] Carrillo, L., Magdaleno, F. X., Casademunt, J., & Ortin, J. *Experiments in a rotating Hele-Shaw cell*. Phys. Rev. E, 1996. **54**, 6260.

[9] Lopez-Salvans, M. Q., Trigueros, P. P., Vallmitjana, S., & Sagues, F. *Fingerlike Aggregates in Thin-Layer Electrodeposition*. Phys. Rev. Lett., 1996. **76**, 4062.

[10] Ghatak, A., Chaudhury, M. K., Shenoy, V., & Sharma, A. *Meniscus Instability in a Thin Elastic Film*. Phys. Rev. Lett., 2000. **85**, 4329.

[11] Zik, O., Olami, Z., & Moses, E. *Fingering Instability in Combustion*. Phys. Rev. Lett., 1998. **81**, 3868.

[12] Harten, U., Lahee, A. M., Toennies, J. P., & Wöll, C. *Observation of a Soliton Reconstruction of Au(111) by High-Resolution Helium-Atom Diffraction*. Phys. Rev. Lett., 1985. **54**, 2619.

[13] Barth, J. V., Brune, H., Ertl, G., & Behm, R. J. *Scanning tunneling microscopy observations on the reconstructed Au(111) surface: Atomic structure, long-range superstructure, rotational domains, and surface defects*. Phys. Rev. B, 1990. **42**, 9307.

[14] Guo, Q., Yin, F., & Palmer, R. E. *Beyond the Herringbone Reconstruction: Magic Gold Fingers*. Small, 2005. **1**, 76.

[15] Naumovets, A. & Zhang, Z. *Fidgety particles on surfaces: how do they jump, walk, group, and settle in virgin areas?*. Surf. Sci., 2002. **500**, 212.

[16] Ferrando, R. & Treglia, G. *Tight-binding molecular dynamics study of diffusion on Au and Ag(111)*. Surf. Sci., 1995. **331**, 920.

[17] Boisvert, G. & Lewis, L. J. *Diffusion of Au on the reconstructed Au(111) surface*. In Gruber, R. & Tomassini, M., editors, *Physics Computing 94*. European Physical Society, Geneva, 1994 page 29.

[18] Ratsch, C., Seitsonen, P., & Scheffler, M. *Strain dependence of surface diffusion: Ag on Ag(111) and Pt(111)*. Phys. Rev. B, 1997. **55**, 6750.

[19] Brune, H., Bromann, K., Röder, H., & Kern, K. *Effect of strain on surface diffusion and nucleation*. Phys. Rev. B, 1995. **52**, 14,380.

[20] Michely, T., Hohage, M., Bott, M., & Comsa, G. *Inversion of Growth Speed Anisotropy in Two Dimensions*. Phys. Rev. Lett., 1993. **70**, 3943.

[21] Zhong, J., Zhang, T., Zhang, Z., & Lagally, M. G. *Island-corner barrier effect in two-dimensional pattern formation at surfaces*. Phys. Rev. B, 2001. **63**, 113,403.

[22] Dovek, M. M., Lang, C. A., Nogami, J., & Quate, C. F. *Epitaxial growth of Ag on Au(111) studied by scanning tunneling microscopy*. Phys. Rev. B, 1989. **40**, 11,973.

[23] Kürpick, U. & Rahman, T. S. *Tip Induced Motion of Adatoms on Metal Surfaces*. Phys. Rev. Lett., 1999. **83**, 2765.

[24] Haruta, M. *Size- and support-dependency in the catalysis of gold*. Catal. Today, 1997. **36**, 153.

[25] Nam, J.-W., Thaxton, C. S., & Mirkin, C. A. *Nanoparticle-Based Bio-Bar Coded for the Ultrasensitive Detection of Proteins*. Science, 2003. **301**, 1884.

[26] Rosi, N. L., Giljohann, D. A., Thaxton, C. S., Lytton-Jean, A. K. R., Han, M. S., & Mirkin, C. A. *Oligonucleotide-Modified Gold Nanoparticles for Intracellular Gene Regulation*. Science, 2006. **312**, 1027.

[27] Chen, S., Ingram, R. S., Hostetler, M. J., Pietron, J. J., Murray, R. W., Schaaff, T. G., Khoury, J. T., Alvarez, M. M., & Whetten, R. L. *Gold Nanoelectrodes of Varied Size: Transition to Molecule-Like Charging*. Science, 1998. **280**, 2098.

[28] Zheng, X., Shi, X., Dai, Z., & Zeng, Z. *Transport properties of the Au_{32} cluster with fullerene symmetry*. Phys. Rev. B, 2006. **74**, 85,418.

[29] Kondo, Y. & Takayanagi, K. *Synthesis and Characterization of Helical Multi-Shell Gold Nanowires*. Science, 2000. **289**, 5479.

[30] Wang, B., Yin, S., Wang, G., Buldum, A., & Zhao, J. *Novel Structures and Properties of Gold Nanowires*. Phys. Rev. Lett., 2001. **86**, 2046.

[31] Brenner, D. W. *The Art and Science of an Analytic Potential*. Phys. Stat. Sol. B, 2000. **217**, 23.

[32] Jones, J. E. & Ingham, A. E. *On the calculation of certain crystal potential constants, and on the cubic crystal of least potential energy*. Proc. R. Soc. London Ser. A, 1925. **107**, 636.

[33] Morse, P. M. *Diatomic molecules according to the wave mechanics. II. Vibrational levels*. Phys. Rev., 1929. **34**, 57.

[34] Gupta, R. P. *Lattice relaxation at metal surfaces*. Phys. Rev. B, 1981. **23**, 6265.

[35] Daw, M. S. & Baskes, M. I. *Semiempirical, Quantum Mechanical Calculation of Hydrogen Embrittlement in Metals*. Phys. Rev. Lett., 1983. **50**, 1285.

[36] Daw, M. S. & Baskes, M. I. *Embedded-atom method: Derivation and application to impurities, surfaces and other defects in metals*. Phys. Rev. B, 1984. **29**, 6443.

[37] Sutton, A. P. & Chen, J. *Long-range Finnis-Sinclair potentials*. Philos. Mag. Lett., 1990. **61**, 139.

[38] Finnis, M. W. & Sinclair, J. E. *A simple empirical n-body potential for transition-metals*. Phylos. Mag. A, 1984. **50**, 45.

[39] Jacobsen, K. W., Nørskov, J. K., & Puska, M. J. *Interatomic interactions in the effective-medium theory*. Phys. Rev. B, 1987. **35**, 7423.

[40] Tomanek, D., Aligia, A. A., & Balseiro, C. A. *Calculation of elastic strain and electronic effects on surface segregation*. Phys. Rev. B, 1985. **32**, 5051.

[41] Rosato, V., Guillope, M., & Legrand, B. *Thermodynamical and structural properties of f.c.c. transition metals using a simple tight-binding model*. Phil. Mag. A, 1989. **59**, 321.

[42] Cleri, F. & Rosato, V. *Tight-binding potential for transition metals and alloys*. Phys. Rev. B, 1993. **48**, 22.

[43] Wales, D. J. *Energy Landscapes with Application to Clusters, Biomolecules and Glasses*. Cambridge University Press, 2003.

[44] Allen, M. P. & Tildesley, D. J. *Computer Simulations of Liquids*. Oxford Science Publications, 1987.

[45] Wilson, N. T. & Johnston, R. L. *Modelling gold clusters with an empirical many-body potential*. Eur. Phys. J. D, 2000. **12**, 161.

[46] Wales, D. J. & Doye, J. P. K. *Global optimization by basin-hopping and the lowest energy structure of Lennard-Jones clusters containg up to 110 atoms*. J. Phys. Chem. A, 1997. **101**, 5111.

[47] Cartwright, H. M. *Applications of Artificial Intelligence in Chemistry*. Oxford Science Publications, 1993.

[48] Zeiri, Y. *Prediction of the lowest energy structure of clusters using a genetic algorithm*. Phys. Rev. E, 1995. **51**, R2769.

[49] Byrd, R. H., Lu, P., Nocedal, J., & Zhu, C. *A limited memory algorithm for bound constrained optimization*. SIAM J. Sci. Comp., 1995. **5**, 1190.

[50] Deaven, D. M. & Ho, K. M. *Molecular Geometry Optimization with a Genetic Algorithm*. Phys. Rev. Lett., 1995. **75**, 288.

[51] Johnston, R. L. *Atomic and Molecular Clusters*. Taylor & Francis, 2002.

[52] Wales, D. J. *Structure, Dynamics, and Thermodynamics of Clusters: Tales from Topographic Potential Surfaces*. Science, 1996. **271**, 925.

[53] Doye, J. P. K., Wales, D. J., & Berry, R. S. *The effect of the range of the potential on the structures of clusters*. J. Chem. Phys., 1995. **103**, 4234.

[54] Andres, R. P., Bein, T., Dorogi, M., Feng, S., Henderson, J. I., Kubiac, C. P., Mahoney, W., Osifchin, R. G., & Reifenberger, R. *Coulomb Staircase at Room Temperature in a Self-Assembled Molecular Nanostructure*. Science, 1996. **272**, 1323.

[55] Mirkin, C. A., Letsinger, R. L., Mucic, R. C., & Storhoff, J. J. *A DNA-based method for rationally assembling nanoparticles into macroscopic materials*. Nature, 1996. **382**, 607.

[56] Alivisatos, A. P., Johnsson, K. P., Peng, X., Wilson, T. E., Loweth, C. J., Jr, M. P. B., & Schultz, P. G. *Organization of 'nanocrystal molecules' using DNA*. Nature, 1996. **382**, 609.

[57] Cleveland, C. L., Landman, U., Shaaff, T. G., Shafigullin, M. N., Stephens, P. W., & Whetten, R. L. *Structural Evolution of Small Gold Nanoparticles: The Truncated Decahedral Motif*. Phys. Rev. Lett., 1997. **79**, 1873.

[58] Marks, L. D. *Experimental studies of small particle structures*. Rep. Prog. Phys., 1994. **57**, 603.

[59] Garzón, I. L. & Posada-Amarillas, A. *Structural and vibrational analysis of amorphous Au_{55} clusters*. Phys. Rev. B, 1996. **54**, 11,796.

[60] Garzón, I. L., Michaelian, K., Beltrán, M. R., Posada-Amarillas, A., Ordejon, P., & Artacho, E. *Lowest Energy Structures of Gold Nanoclusters*. Phys. Rev. Lett., 1998. **81**, 1600.

[61] Michaelian, K., Rendón, N., & Garzon, I. L. *Structure and energetics of Ni, Ag, and Au nanoclusters*. Phys. Rev. B, 1999. **60**, 2000.

[62] Doye, J. P. K. & Wales, D. J. *The effect of the range of the potential on the structure and stability of simple liquids: from clusters to bulk, from sodium to C_{60}*. J. Phys. B, 1996. **29**, 4859.

[63] Doye, J. P. K. & Wales, J. *Global minima for transition metal clusters described by Sutton-Chen potentials*. New J. Chem., 1998. **22**, 733.

[64] Soler, J. M., Beltrán, M. R., Michaelian, K., Garzón, I. L., Ordejon, P., Sanchez-Portal, D., & Artacho, E. *Metallic bonding and cluster structure*. Phys. Rev. B, 2000. **61**, 5771.

[65] Baletto, F., Ferrando, R., Fortunelli, A., Montalenti, F., & Mottet, C. *Crossover among structural motifs in transition and noble-metal clusters*. J. Chem. Phys., 2002. **116**, 3856.

[66] Darby, S., Mortimer-Jones, T. V., Johnston, R. L., & Roberts, C. *Theoretical study of Cu-Au nanoalloy clusters using a genetic algorithm*. J. Chem. Phys., 2002. **116**, 1536.

[67] Mottet, C. (private communication).

[68] Sebetci, A. (private communication).

[69] Kittel, C. *Introduction to Solid State Physics*. John Wiley & Sons, Inc., sixth edition, 1986.

[70] Miedema, A. R. *Surface energies of solid metals*. Z. Metallkd., 1978. **69**, 287.

[71] Fernández, E. M., Balbás, L. B., Pérez, L. A., Michaelian, K., & Garzón, I. L. *Structural properties of bimetallic clusters from density functional calculations.* Int. J. Mod. Phys. B, 2005. **19**, 2339.

[72] Barcaro, G., Fortunelli, A., Rossi, G., Nita, F., & Ferrando, R. *Electronic and structural shell closure in AgCu and AuCu nanoclusters.* J. Phys. Chem. B, 2006. **110**, 23,197.

[73] Paz-Borbón, L. O., Johnston, R. L., Barcaro, G., & Fortunelli, A. *A mixed structural motif in 34-atom Pd-Pt.* Rev. Mod. Phys., 2005. **77**, 371.

[74] Stroscio, J. & Kaiser, W., editors. *Scanning Tunneling Microscopy*, volume 27 of *Methods of Experimental Physics*. Academic Press, 1993.

[75] Chen, C. J. *Introduction to Scanning Tunneling Microscopy*. Oxford University Press, Oxford, 1993.

[76] Ball, P. *The Self-made Tapestry. Pattern formation in nature*. Oxford University Press, Oxford, 1999.

[77] Uppert, H. E. *Flow and instability of a viscous current down a slope*. Nature, 1982. **300**, 427.

[78] Saffman, P. G. & Taylor, G. I. *The penetration of a fluid into a porous medium or Hele-Shaw cell containing a more viscous liquid*. Proc. R. Soc. London, Ser. A, 1958. **245**, 312.

[79] Moore, M. G., Juel, A., Burgess, J. M., McCormick, W. D., & Swinney, H. L. *Fluctuations in viscous fingerings.* Phys. Rev. B, 2002. **65**, 30,601.

[80] Maher, J. V. *Development of Viscous Fingering Patterns.* Phys. Rev. Lett., 1985. **54**, 1498.

[81] DiFrancesco, M. W. & Maher, J. V. *Hele-Shaw scaling properties of low-constrast Saffman-Taylor flows*. Phys. Rev. A, 1989. **40**, 295.

[82] de Bruyn, J. R. *Fingering Instability of Gravity Currents*. Phys. Rev. Lett., 1995. **74**, 4843.

[83] Shull, K. R., Flanigan, C. M., & Crosby, A. J. *Fingering Instabilities of Confined Elastic Layers in Tension*. Phys. Rev. Lett., 2000. **84**, 3057.

[84] Bales, G. S. & Zangwill, A. *Morphological instability of a terrace edge during step-flow growth*. Phys. Rev. B, 1990. **41**, 5500.

[85] Pimpinelli, A., Elkinani, I., Karma, A., Misbah, C., & Villain, J. *Step motions on high-temperature vicinal surfaces*. J. Phys: Condens. Matter, 1994. **6**, 2661.

[86] Tung, R. T. & Schrey, F. *Topography of the Si(111) Surface during Silicon Molecular-Beam Epitaxy*. Phys. Rev. Lett., 1989. **63**, 1277.

[87] Wu, F., Jaloviar, S. G., Savage, D. E., & Lagally, M. G. *Roughening of Steps during Homoepitaxial Growth on Si(001)*. Phys. Rev. Lett., 1993. **71**, 4190.

[88] Schwenger, L., Folkerts, R. L., & Ernst, H. J. *Bales-Zangwill meandering instability observed in homoepitaxial step-flow growth*. Phys. Rev. B, 1997. **55**, R7406.

[89] Burton, W. K., Cabrera, N., & Frank, F. C. *The growth of crystals and the equilibrium structure of theis surfaces*. Philos. Trans. R. Soc. London, Ser. A, 1951. **243**, 299.

[90] Ehrlich, G. & Hudda, F. G. *Atomic view of surface self-diffusion: tungsten on tungsten*. J. Chem. Phys., 1966. **44**, 1039.

[91] Schwoebel, R. L. & Shipsey, E. J. *Step Motion on Crystal Surfaces*. J. Appl. Phys., 1966. **37**, 3682.

[92] Pimpinelli, A. & Villain, J. *Physics of Crystal Growth*. Cambridge University Press, Cambridge, 1998.

[93] Atkins, P. & de Paula, J. *Physical Chemistry*. Oxford University Press, Oxford, seventh edition, 2002.

[94] Wöll, C., Chiang, S., Wilson, R. J., & Lippel, P. H. *Determination of atom positions at stacking-fault dislocations on Au(111) by scanning tunneling microscopy*. Phys. Rev. B, 1989. **39**, 7988.

[95] Frank, F. C. & van der Merwe, J. H. *One-dimensional dislocations I. Static theory*. Proc. Soc. London Ser. A, 1948. **198**, 205.

[96] Takeuchi, N., Chan, C. T., & Ho, K. M. *Au(111): A theoretical study of the surface reconstruction and the surface electronic states*. Phys. Rev. B, 1991. **43**, 13,899.

[97] Mansfield, M. & Needs, R. J. *Application of the Frenkel-Kontorova model to surface reconstruction*. J. Phys.: Condens Matter, 1990. **2**, 2361.

[98] Crljen, Z., Lazic, P., Sokcevic, D., & Brako, R. *Relaxation and reconstruction on (111) surfaces of Au, Pt and Cu*. Phys. Rev. B, 2003. **68**, 195,411.

[99] Trimble, T. M., Cammarata, R. C., & Sieradzki, K. *The stability of fcc(111) metal surfaces*. Surf. Sci., 2003. **531**, 8.

[100] Johnson, R. A. *Analytic nearest-neighbor model for fcc metals*. Phys. Rev. B, 1988. **37**, 3924.

[101] Yin, F., Guo, Q., & Palmer, R. E. *Nanostructured gold surfaces fabricated with the STM*. Japan. J. Appl. Phys., 2006. **45**, 2053.

[102] Yin, F., Palmer, R. E., & Guo, Q. *Faceting of nanoscale fingers on the (111) surface of gold*. Surf. Sci., 2006. **600**, 1504.

[103] Yin, F. (private communication).

[104] Laidler, K. J. *Chemical Kinetics*. McGraw Hill, 1965.

[105] Gomer, R. *Diffusion of adsorbates on metal surfaces*. Rep. Prog. Phys., 1990. **53**, 917.

[106] Hänggi, P., Talkner, P., & Borkovec, M. *Reaction-rate theory: fifty years after Kramers*. Rev. Mod. Phys., 1990. **62**, 251.

[107] Chudley, C. T. & Elliot, R. J. *Neutron scattering from a liquid on a jump diffusion model*. Proc. Phys. Soc. (London), 1961. **77**, 353.

[108] Revesz, P. *Aspects and Applications of the Random Walk*. North Holland, Amsterdam, 1994.

[109] Weiss, G. H. *Random Walk in Random and Non-Random Environments*. World Scientific Publishing, second edition, 2005.

[110] Ferrando, R., Spadacini, R., & Tommei, G. E. *Kramers problem in periodic potentials: Jump rate and jump lengths*. Phys. Rev. E, 1993. **48**, 2437.

[111] Ala-Nissila, T. & Ying, S. C. *Theory of classical surface diffusion*. Prog. Surf. Sci., 1992. **39**, 227.

[112] Kellogg, G. L. *Field ion microscope studies of single-atom surface diffusion and cluster nucleation on metal surfaces*. Surf. Sci. Rep., 1994. **21**, 1.

[113] Tsong, T. T. *Atomic, molecular and cluster dynamics on flat and stepped surfaces*. Prog. Surf. Sci., 2000. **64**, 199.

[114] Barth, J. V. *Transport of adsorbates at metal surfaces: from thermal migration to hot precursors*. Surf. Sci. Rep., 2000. **40**, 75.

[115] Ala-Nissila, T., Ferrando, R., & Ying, S. C. *Collective and single particle diffusion on surfaces*. Adv. Phys., 2002. **51**, 949.

[116] Wrigley, J. D. & Ehrlich, G. *Surface Diffusion by an Atomic Exchange Mechanism*. Phys. Rev. Lett., 1980. **44**, 661.

[117] Chen, C. L. & Tsong, T. T. *Displacement Distribution and Atomic Jump Direction in Diffusion of Ir Atoms on the Ir(001) Surface*. Phys. Rev. Lett., 1990. **64**, 3147.

[118] Kellogg, G. L. & Feibelman, P. J. *Surface self-diffusion on Pt(100) by an atomic exchange mechanism*. Phys. Rev. Lett., 1990. **64**, 3147.

[119] Mo, Y. W. *Direct Determination of Surface Diffusion by Displacement Distribution Measurement with Scanning Tunneling Microscopy*. Phys. Rev. Lett., 1993. **71**, 2923.

[120] Brune, H. *Microscopic view of epitaxial metal growth: nucleation and aggregation*. Surf. Sci. Rep., 1998. **31**, 121.

[121] Michely, T. & Krug, J. *Islands, Mounds and Atoms. Patterns and Processes in Crystal Growth Far from Equilibrium*. Springer, Berlin, Heidelberg, 2004.

[122] Mo, Y. W. *Activation Energy for Surface Diffusion of Si on Si(001): A Scanning-Tunneling-Microscopy Study*. Phys. Rev. Lett., 1991. **66**, 1998.

[123] Ayrault, G. & Ehrlich, G. *Surface self-diffusion on an fcc crystal: An atomic view*. J. Chem. Phys., 1974. **60**, 271.

[124] Wang, S. C. & Ehrlich, G. *Self-Adsorption Sites on a Close-Packed Surface: Ir on Ir(111)*. Phys. Rev. Lett., 1989. **62**, 2297.

[125] Chen, C. L. & Tsong, T. T. *Behavior of Ir atoms and clusters on Ir surfaces*. Phys. Rev. B, 1990. **41**, 12,403.

[126] Boisvert, G., Lewis, L. J., Puska, M. J., & Nieminen, R. M. *Energetics of diffusion on the (100) and (111) surfaces of Ag, Au, and Ir from first principles*. Phys. Rev. B, 1995. **52**, 9078.

[127] Chen, C. L. & Tsong, T. T. *Self-Diffusion on the Reconstructed and Nonreconstructed Ir(110) Surfaces*. Phys. Rev. Lett., 1991. **66**, 1610.

[128] Feibelman, P. J., Nelson, J. S., & Kellogg, G. L. *Energetics of Pt adsorption on Pt(111)*. Phys. Rev. B, 1994. **49**, 10,548.

[129] Kyuno, K., Gölzhäuser, A., & Ehrlich, G. *Growth and the difffusion of platinum atoms and dimers on Pt(111)*. Surf. Sci., 1998. **397**, 191.

[130] Bott, M., Hohage, M., Morgenstern, M., Michely, T., & Comsa, G. *New Approach for Determination of Diffusion Parameters of Adatoms*. Phys. Rev. Lett., 1996. **76**, 1304.

[131] Li, Y. & DePristo, E. *Predicted growth mode for homoepitaxy on the fcc(111) surface*. Surf. Sci., 1996. **351**, 189.

[132] Stoltze, P. *Simulation of surfaces defects*. J. Phys.: Condens. Matter, 1994. **6**, 9495.

[133] Kellogg, G. L. *Temperature dependence of surface self-diffusion on Pt(001)*. Surf. Sci., 1991. **246**, 31.

[134] Boisvert, G. & Lewis, L. J. *Self-diffusion on low-index metallic surfaces: Ag and Au (100) and (111)*. Phys. Rev. B, 1996. **54**, 2880.

[135] Yu, B. D. & Scheffler, M. *Anisotropy of Growth of the Close-Packed Surfaces of Silver*. Phys. Rev. Lett., 1996. **77**, 1095.

[136] Barth, J. V., Brune, H., Fischer, B., Weckesser, J., & Kern, K. *Dynamics of Surface Migration in the Weak Corrugation Regime*. Phys. Rev. Lett., 2000. **84**, 1732.

[137] Stumpf, R. & Scheffer, M. *Theory of Self-Diffusion at and Growth of Al(111)*. Phys. Rev. Lett., 1994. **72**, 254.

[138] Liu, C. L., Cohen, J. M., Adams, J. B., & Voter, A. F. *EAM study of surface self-diffusion of single adatoms of fcc metals Ni, Cu, Al, Ag, Au, Pd, and Pt*. Surf. Sci., 1991. **253**, 334.

[139] Stumpf, R. & Scheffer, M. Ab initio *calculation of energies and self-diffusion on flat and stepped surfaces of Al and their implications on crystal growth*. Phys. Rev. B, 1996. **53**, 4958.

[140] Boisvert, G., Lewis, L. J., & Yelon, A. *Many-Body Nature of the Meyer-Neldel Compensation Law for Diffusion*. Phys. Rev. Lett., 1995. **75**, 469.

[141] Kürpick, U. *Self-diffusion on (100), (110), and (111) surfaces of Ni and Cu: A detailed study of prefactors and activation energies*. Phys. Rev. B, 2001. **64**, 75,418.

[142] Wang, S. C. & Ehrlich, G. *Adatom diffusion on W(211): Re, W, Mo, Ir, and Rh*. Surf. Sci., 1988. **206**, 451.

[143] Liu, Y. B., Sun, D. Y., & Gong, X. G. *Local strain induced anisotropic diffusion on $\left(23 \times \sqrt{3}\right)$-Au(111) surface*. Surf. Sci., 2002. **498**, 337.

[144] Sandy, A. R., Mochrie, S. G. J., Zehner, D. M., Grübel, G., Huang, K. G., & Gibbs, D. *Reconstruction of the Pt(111) Surface*. Phys. Rev. Lett., 1992. **68**, 2192.

[145] Bott, M., Hohage, M., Michely, T., & Comsa, G. *Pt(111) Reconstruction Induced by Enhanced Pt Gas-Phase Chemical Potential*. Phys. Rev. Lett., 1993. **70**, 1489.

[146] Jacobsen, J., Jacobsen, K. W., & Stoltze, P. *Nucleation of the Pt(111) reconstruction: a simulation study*. Surf. Sci., 1994. **317**, 8.

[147] Zhang, Z. & Lagally, M. G. *Atomistic Processes in the Early Stages of Thin-Film Growth*. Science, 1997. **276**, 377.

[148] Eigler, D. M. & Schweizer, E. K. *Positioning single atoms with a scanning tunneling microscope*. Nature, 1990. **344**, 524.

[149] Crommie, M. F., Lutz, C. P., & Eigler, D. M. *Confinement of Electrons to Quantun Corrals on a Metal Surface*. Science, 1993. **262**, 218.

[150] Zhang, Z. & Lagally, M. G. *Atomic Processes in the Early Stage of Thin-Film Growth*. Science, 1997. **276**, 377.

[151] Barth, J. V., Costantini, G., & Kern, K. *Engineering atomic and molecular nanostructures at surfaces*. Nature, 2005. **437**, 671.

[152] Liu, S., Zhang, Z., Comsa, G., & Metiu, H. *Kinetic Mechanism for Island Shape Variations Caused by Changes in the Growth Temperature*. Phys. Rev. Lett., 1993. **71**, 2967.

[153] Jacobsen, J., Jacobsen, K. W., & Nøorskov, J. K. *Island shapes in homoepitaxial growth of Pt(111)*. Surf. Sci., 1996. **359**, 37.

[154] Kallf, M., Comsa, G., & Michely, T. *How Sensitive is Epitaxial Growth to Adsorbates?*. Phys. Rev. Lett., 1998. **81**, 1255.

[155] Ovesson, S., Bogicevic, A., & Lundqvist, B. I. *Origin of Compact Triangular Islands in Metal-on-Metal Growth*. Phys. Rev. Lett., 1999. **83**, 2608.

[156] Bogicevic, A., Strömquist, J., & Lundqvist, B. I. *Low-Symmetry Diffusion Barriers in Homoepitaxial Growth of Al(111)*. Phys. Rev. Lett., 1998. **81**, 637.

[157] Feibelman, P. J. *Self-diffusion along step bottoms on Pt(111)*. Phys. Rev. B, 1999. **60**, 4972.

[158] Wu, J., Wang, E. G., Varga, K., Liu, B. G., Pantelides, S. T., & Zhang, Z. *Island Shape Selection in Pt(111) Submonolayer Homoepitaxy with or without CO as an Adsorbate*. Phys. Rev. Lett., 2002. **89**, 146,103.

[159] Brune, H., Röder, H., Bromann, K., Kern, K., Jacobsen, J., Stoltze, P., Jacobsen, K., & Nørskov, J. *Anisotropic corner diffusion as origin for dendritic growth on hexagonal substrates*. Surf. Sci., 1996. **349**, L115.

[160] Cox, E., Li, M., Chung, P., Ghosh, C., Rahman, T. S., Jenks, C. J., Evans, J. W., & Thiel, P. A. *Temperature dependence of island growth shapes during submonolayer deposition of Ag on Ag(111)*. Phys. Rev. B, 2005. **71**, 115,414.

[161] Chambliss, D. D., Wilson, R. J., & Chiang, S. *Nucleation of Ordered Ni Island Arrays on Au(111) by Surface-Lattice Dislocation*. Phys. Rev. Lett., 1991. **66**, 1721.

[162] Chambliss, D. D., Wilson, R. J., & Chiang, S. *Ordered nucleation of Ni and Au islands on Au(111) studied by scanning tunneling microscopy*. J. Vac. Sci. Technol. B, 1991. **9**, 933.

[163] Meyer, J. A., Baikie, I. D., Kopatzki, E., & Behm, R. J. *Preferential island nucleation at the elbows of the Au(111) herringbone reconstruction through place exchange*. Surf. Sci., 1996. **365**, L647.

[164] Stroscio, J. A., Pierce, D. T., Dragoset, R. A., & First, P. N. *Miscroscopic aspects of the initial growth of metastable fcc iron on Au(111)*. J. Vac. Sci. Technol. A, 1992. **10**, 1981.

[165] Voigtländer, B., Meyer, G., & Amer, N. M. *Epitaxial growth of thin magnetic cobalt films on Au(111) studied by scanning tunneling microscopy*. Phys. Rev. B, 1991. **44**, 10,354.

[166] Fischer, B., Barth, J. V., Fricke, A., Nedelmann, L., & Kern, K. *Growth and surface alloying of Al on Au(111) at room temperature*. Surf. Sci., 1997. **389**, 366.

[167] Chambliss, D. D. & Wilson, R. J. *Relaxed diffusion limited aggregation of Ag on Au(111) observed by scanning tunneling microscopy*. Surf. Sci., 1991. **9**, 928.

[168] Didiot, C., Pons, S., Kierren, B., Fagot-Revurat, Y., & Malterre, D. *Ag nanostructures on Au(778): A self-assembled superlattice of metallic quantum resonators*. Surf. Sci., 2006. **600**, 3917.

[169] Ferrando, R. & Treglia, G. *Anisotropy of diffusion along steps on the (111) faces of gold and silver*. Phys. Rev. B, 1994. **50**, 12,104.

[170] Frenkel, D. & Smit, B. *Understanding Molecular Simulation, From Algorithms to Applications*. Academic Press, San Diego, 1996.

[171] Bortz, A. B., Kalos, M. H., & Lebowitz, J. L. *A new algorithm for Monte Carlo simulation of Isinig spin systems*. J. Comput. Phys., 1975. **17**, 10.

[172] Kotrla, M. *Numerical simulations in the theory of crystal growth*. Comput. Phys. Commun., 1996. **97**, 82.

[173] Voter, A. F., Montalenti, F., & Germann, T. C. *Extending the time scale in atomistic simulations of materials*. Annu. Rev. Mater. Res., 2002. **32**, 321.

[174] Henkelman, G. & Jonsson, H. *Long time scale Kinetic Monte Carlo simulations without lattice approximation and predefined event table*. J. Chem. Phys., 2001. **115**, 9657.

[175] Trushin, O., Karim, A., Kara, A., & Rahman, T. S. *Self-learning kinetic Monte Carlo method: Application to Cu(111)*. Phys. Rev. B, 2005. **72**, 115,401.

[176] Bena, I., Misbah, C., & Valance, A. *Nonlinear evolution of a terrace edge during step-flow growth*. Phys. Rev. B, 1993. **47**, 7408.

[177] Pierre-Louis, O., Misbah, C., Saito, Y., Krug, J., & Politi, P. *New Nonlinear Evolution Equation for Steps during Molecular Beam Epitaxy on Vicinal Surfaces*. Phys. Rev. Lett., 1998. **80**, 4221.

[178] Eigler, D. M., Lutz, C. P., & Rudge, W. E. *An atomic switch realized with the scanning tunnelling microscope*. Nature, 1991. **352**, 600.

[179] Gimzewski, J. K. & Joachim, C. *Nanoscale Science of Single Molecules Using Local Probes*. Science, 1999. **283**, 1683.

[180] Withman, L. J., Stroscio, J. A., Dragoset, R. A., & Celotta, R. J. *Manipulation of Adorbed Atoms and Creation of New Structures on Room-Temperature Surfaces with a Scanning Tunneling Microscope*. Science, 1991. **251**, 1206.

[181] Avouris, P. *Molecular electronics with carbon nanotubes*. Acc. Chem. Res., 1995. **28**, 95.

[182] Bartels, L. & Rieder, K.-H. *Basic Steps of Lateral Manipulation of Single Atoms and Diatomic Clusters with a Scannig Tunneling Microscope Tip*. Phys. Rev. Lett., 1997. **79**, 697.

[183] Meyer, G., Bartels, L., Zöphel, S., Henze, E., & Rieder, K.-H. *Controlled Atom by Atom Restructuring of a Metal Surface with the Scanning Tunneling Microscope*. Phys. Rev. Lett., 1997. **78**, 1512.

[184] Li, J. L. & Schneider, W.-D. *Tip-Assisted Diffusion on Ag(110) in Scanning Tunneling Micrsocopy*. Phys. Rev. Lett., 1996. **76**, 1888.

[185] Mugele, F., Rattenberger, A., Boneberg, J., & Leiderer, P. *The influence of tip-sample interaction on step fluctuations on Ag(111)*. Surf. Sci., 1998. **400**, 86.

[186] Pascual, J. I., Mendez, J., Gomez-Herrero, J., Baró, A. M., & Garcia, N. *Quantum Contact in Gold Nanostructures by Scanning Tunneling Microscopy*. Phys. Rev. Lett., 1993. **71**, 1852.

[187] Mendez, J., Gomez-Herrero, J., Pascual, J. I., Saenz, J. J., Soler, J. M., & Baró, M. *Diffusion of atoms on Au(111) by the electric field gradient in scanning tunneling microscopy*. J. Vac. Sci. Technol. B, 1996. **14**, 1145.

[188] Clarke, A. R. H., Pethica, J. B., Nieminem, J. A., Besenbacher, F., Lægsgaard, E., & Stensgaard, I. *Quantitative Scanning Tunneling Microscopy at Atomic Resolution: Influence of Forces and Tip Configuration*. Phys. Rev. Lett., 1996. **76**, 1276.

[189] Olesen, L., Brandbyge, M., Sørensen, M. R., Jacobsen, K. W., Lægsgaard, E., Stensgaard, I., & Besenbacher, F. *Apparent Barrier Height in Scanning Tunneling Microscopy*. Phys. Rev. Lett., 1996. **76**, 1485.

[190] Limot, L., Kröger, J., Berndt, R., Garcia-Lekue, A., & Hofer, W. A. *Atom Transfer and Single-Adatom Contacts*. Phys. Rev. Lett., 2005. **94**, 126,102.

[191] Hofer, W. A., Fisher, A. J., Wolkow, R. A., & Grütter, P. *Surface Relaxations, Current Enhancements, and Absolute Distances in High Resolution Scanning Tunneling Micrsocopy*. Phys. Rev. Lett., 2001. **87**, 236,104.

[192] Kürpick, U. & Fricke, B. *Manipulation of Cu adatoms on anisotropic Cu surfaces using scanning tunneling microscopy*. Surf. Sci., 2000. **460**, 1.

[193] Stroscio, J. A. & Eigler, D. M. *Atomic and Molecular Manipulation with the Scanning Tunneling Microscope*. Science, 1991. **254**, 1319.